

# A two-phase model of galaxy formation: III. The formation of globular clusters

Yangyao Chen<sup>1,2</sup>\*, Houjun Mo<sup>3</sup> and Huiyuan Wang<sup>1,2</sup>

<sup>1</sup>*School of Astronomy and Space Science, University of Science and Technology of China, Hefei, Anhui 230026, China*

<sup>2</sup>*Department of Astronomy, University of Science and Technology of China, Hefei, Anhui 230026, China*

<sup>3</sup>*Department of Astronomy, University of Massachusetts, Amherst, MA 01003, USA*

Accepted XXX. Received YYY; in original form ZZZ

## ABSTRACT

We develop a model of globular cluster (GC) formation within the cosmological hierarchy of structure formation. The model is rooted in the ‘two-phase’ scenario of galaxy formation developed in Paper-I, where the fast accretion of dark matter halos at high redshift leads to the formation of self-gravitating, turbulent gas clouds that subsequently fragment into dynamically hot systems of dense sub-clouds with masses  $\sim 10^6$ – $10^7 M_\odot$ . Here we elaborate on the formation, evolution, and fate of these sub-clouds, and show that some of the sub-clouds can be compactified via two distinctive channels into a ‘supernova-free’ regime to form two distinct populations of GCs. The model is simple, characterized by a small number of free parameters underpinned by physical considerations, and can be efficiently implemented into cosmological N-body simulations to generate a coherent sample of halos, galaxies, and GCs. Calibrated with observations, our model can reproduce a range of observational statistics, including those for GC masses, sizes, metallicities, spatial distributions, and the relation of GC systems with host galaxies/halos. Significant discrepancies between model results and existing observations are discussed in connection to processes implemented in the model. Predictions for GCs are made for both the local Universe and for redshift up to  $z \approx 10$ , and can be tested by upcoming observations.

**Key words:** globular clusters: general – ISM: clouds – galaxies: high-redshift – galaxies: haloes – galaxies: formation

## 1 INTRODUCTION

Globular clusters (hereafter GCs) are massive and dense stellar systems observed in nearly every galaxy (Harris & Racine 1979; Krumholz et al. 2019). Many GCs have old age, low metallicity and high density compared to their host galaxies, implying that they are remnants of star formation in the early Universe (Peebles & Dicke 1968; Fall & Rees 1985) and thus provide fossils for cosmological archaeology. At a distinct and important rank in the cosmic structure hierarchy, GCs are crucial to understanding galaxy formation, extending its boundaries to extreme conditions on small scales.

Current observations have already provided critical information about the formation of GCs. They are observed in galaxies of all masses (Blakeslee 1997, 1999; Harris & Racine 1979; Harris 2023) and morphology (Harris et al. 2015) in diverse environments (Forbes et al. 2020; Janssens et al. 2022; Saifollahi et al. 2022; Jones et al. 2023; Forbes & Gannon 2024) in the local Universe. The discovery of young massive star clusters (YMSCs; Whitmore et al. 1999; Figer et al. 1999; Schweizer 1999; Zhang & Fall 1999; Figer 2004; Bastian et al. 2006) suggests that the conditions for GC formation are still present in the local Universe, particularly in starburst and interacting/merging galaxies (see Krumholz et al. 2019, for a review).

The ubiquitous presence of GCs implies that their formation may be driven by some general formation mechanisms rather than rare conditions associated with special galaxies or with rare stochastic

processes. On the other hand, observations also show that the population of GCs within a galaxy, commonly referred to as the globular cluster system (GCS) of the galaxy, shows strong correlations with the properties of the host galaxy and host halo (Harris & Racine 1979), suggesting that the diversity and complexity of the GC population may be related to those of the galaxy population. The most intriguing correlation is the linear relationship between the total mass of GCS and the host halo mass observed in the local Universe (e.g. Blakeslee 1997, 1999; Spitler & Forbes 2009; Harris et al. 2013; Hudson et al. 2014; Harris et al. 2015, 2017; Dornan & Harris 2023; Harris 2023). Exceptions seem to occur in dwarf galaxies with halo masses  $\sim 10^{10} M_\odot$ , where the number of GCs is very small and has large scatter (Saifollahi et al. 2022; Jones et al. 2023), and in the brightest cluster galaxies (BCGs), where contributions from satellite galaxies and the intracluster population can introduce significant ambiguity (Spitler & Forbes 2009; Hudson et al. 2014; Dornan & Harris 2023).

This linear relation was inferred to be a result of the central limit theorem applied to massive galaxies, where the total number of GCs brought in by merger events naturally normalize the GCS mass with the halo mass (Boylan-Kolchin 2017; Valenzuela et al. 2021). However, the establishment of such a relation in dwarf galaxies and whether or not this relation also holds at high redshift (hereafter high  $z$ ) remain poorly understood (e.g. Bastian et al. 2020). Alternative explanations have also been proposed, such as higher gas fractions and enhanced GC formation rates in halos of lower masses (e.g. Choksi et al. 2018; Choksi & Gnedin 2019; El-Badry et al.

\* E-mail: yangyaochen.astro@foxmail.com

2019; Chen & Gnedin 2022, 2023, 2024). Within individual galaxies, GCs are found to have a bimodal distribution in color (Fahrion et al. 2020a; Harris 2023; Hartman et al. 2023). This bimodality is interpreted as a result of the bimodal distribution of metallicity, as metal-poor and metal-rich stars follow different evolutionary paths in the color-magnitude diagram, which is also supported by observations with spectroscopically calibrated color-metallicity conversions (Fahrion et al. 2020b; Hartman & Harris 2024). The observed bimodal distribution signifies mechanisms that correlate non-linearly with metallicity, such as galaxy-galaxy merger (Li & Gnedin 2014; Choksi et al. 2018; Valenzuela et al. 2021) and high-density/pressure condition (Kruijssen 2012; Ma et al. 2020), or a bimodal pair of mechanisms that drives the formation and evolution of GCs. There is thus a strong motivation to investigate how the formation and evolution of GCs are correlated with the metallicity of the interstellar medium (ISM).

Previous theoretical modeling and numerical simulations of GC formation have reached a consensus that GCs in general emerge from turbulent, highly pressurized density peaks in the ISM (see e.g. Kruijssen 2014, for a review). Cosmological zoom-in simulations, such as those conducted by Ma et al. (2020), showed that such conditions are naturally produced at high  $z$ . During the structure formation at high  $z$ , fast mass accretion by a dark matter halo can drive large amounts of gas inflow into the galaxy that has formed at the halo center. Such a collapsing process, coupled with the high ISM density and supernova feedback, can generate supersonic turbulence that leads to the formation of dense gas clumps and GCs. At low  $z$ , when halo accretion becomes slow and the overall ISM density becomes too low to form a large number of dense gas clouds, GC formation can still be triggered by occasional galaxy mergers and interactions (Kruijssen 2014). Simulations of individual giant molecular clouds (GMCs) provide further clues about the conditions needed for GC formation. As shown in Fernandez & Bryan (2018), dense gas clumps can be produced in a metal-poor ISM under the influence of a radiation background, even in the absence of compression by strong initial turbulence. In this case, the GMC is unable to fragment and form stars due to inefficient cooling; instead, it contracts and collapses further to form a dense gas core, providing conditions needed for the formation of a GC. These simulations provide support to observational inferences that GCs have formed predominantly in metal-poor ISM in the early Universe. They also demonstrate that the formation of GCs should and can be investigated in the hierarchy of cosmological structure formation.

The main challenge in modeling GC formation in a cosmological context is the large gap between the properties of GCs and their host galaxies. GCs are relatively small, with a typical size of  $\sim 10$  pc (e.g. Krumholz et al. 2019) that is about two orders of magnitude smaller than a typical dwarf galaxy (e.g. Wang et al. 2023). Consequently, certain approximations are necessary to simulate GC formation as a part of galaxy formation in the cosmic density field. Along this line, two semi-analytic approaches have been developed, each incorporating different physical inputs derived from numerical simulations. The first approach involves post-processing cosmological hydrodynamic simulations, or their zoom-in runs, with subgrid physics specific to GC formation. Depending on the resolution of the simulation used, the input conditions for GC formation can range from global properties of individual GMCs (e.g. Grudić et al. 2023) to the smoothed field of the gas properties (e.g. Kruijssen et al. 2011; Pfeffer et al. 2018; Kruijssen et al. 2019a). The second approach more closely resembles traditional semi-analytic models of galaxies based on dark matter halos and their merger trees. The global properties of individual galaxies are obtained from a semi-analytic model (El-Badry

et al. 2019; De Lucia et al. 2024) or an empirical model of galaxy formation (Li & Gnedin 2014; Choksi et al. 2018; Valenzuela et al. 2021), while the criteria for GC formation are based on some properties of the assembly histories of galaxies/halos, such as mergers of galaxies (El-Badry et al. 2019) and rates of halo mass assembly (Li & Gnedin 2014; Choksi et al. 2018; Valenzuela et al. 2021; Chen & Gnedin 2022). Both approaches have been successful in reproducing some observed properties of GCs. Despite the progress, significant knowledge gaps still exist in our understanding of the GC population. Indeed, our understanding of galaxy formation, in particular of star formation and feedback processes, is still incomplete, and so the large-scale conditions for the formation of GCs are still uncertain. In addition, small-scale processes driving the formation and disruption of GCs are also not well understood.

Recent observations by the James Webb Space Telescope (JWST) have opened a new avenue to study galaxy formation in the early Universe. These observations indicated that early galaxies may differ significantly from their counterparts in the local Universe, suggesting that the processes driving galaxy formation at high  $z$  may be different from those in the low- $z$  Universe. In particular, the efficiency of gas consumption by star formation seems to be enhanced significantly at high  $z$  (Bouwens et al. 2023; Finkelstein et al. 2023; Xiao et al. 2024; Weibel et al. 2024; Wang et al. 2024); supermassive black holes (SMBHs) appear to be over-massive for their host galaxy mass (Pacucci et al. 2023; Maiolino et al. 2024; Matthee et al. 2024; Pacucci & Loeb 2024); there seems to be an inversion of metallicity gradients in both the ISM and circumgalactic medium (CGM; Wang et al. 2022; Lin et al. 2023); and the total mass of bound star clusters in galaxies seems to be excessively large (Vanzella et al. 2022, 2023; Welch et al. 2023; Lin et al. 2023; Claeysens et al. 2023; Adamo et al. 2024; Messa et al. 2024; Fujimoto et al. 2024; Mowla et al. 2024; Whitaker et al. 2025). Given that many GCs are old, these discoveries at high  $z$  have important implications for understanding GC formation.

Motivated partly by these discoveries, Mo et al. (2024, hereafter Paper-I) recently proposed a ‘two-phase’ model of galaxy formation that highlights the transition from an early phase of fast halo accretion to a later phase of slow accretion. A critical part of this model is the formation of self-gravitating and turbulent gas clouds (SGCs) during the fast phase. Such an SGC is expected to fragment subsequently and form a dynamically hot system of dense sub-clouds (SCs), each comparable to a GC in terms of both size and mass. This model is capable of reproducing numerous properties of galaxies observed over a large range of redshift. In particular, its predictions for the sub-cloud formation are directly related to the formation of GCs. As we will show in this paper, the model naturally provides conditions for two channels for the formation of GCs, and the GCs produced in the two channels have distinctive properties. Our model thus provides a unified cosmological framework to understand the formation of both galaxies and their GCs, allowing the model to be tested on spatial scales ranging from star clusters to large-scale structures, and on timescales from  $z \approx 0$  to  $z \approx 10$ .

This paper is organized as follows. In §2, we describe the context of galaxy formation within which GCs emerge. In §3, we elaborate on our model of GC formation. In §4, we describe numerical implementations of our model, present its predictions and compare them with observations and with other models. In §5, we summarize our results and discuss their implications. Throughout this paper, we adopt a flat  $\Lambda$ CDM cosmology with parameters derived from the Planck2015 results (Planck Collaboration et al. 2016): the density parameters  $\Omega_{M,0} = 0.3089$ ,  $\Omega_{B,0} = 0.0486$ , and  $\Omega_{\Lambda,0} = 0.6911$ ; the Hubble constant  $H_0 = 100 h \text{ km s}^{-1} \text{ Mpc}^{-1}$ , with  $h = 0.6774$ ; the

Gaussian initial density field with a power spectrum  $P(k) \propto k^n$  with  $n = 0.9667$ ; and a perturbation amplitude specified by  $\sigma_8 = 0.8159$ . To avoid confusion, we use ‘log’ to denote the base-10 logarithm, and ‘ln’ to denote the natural logarithm. We use the terms 1, 2, and 3- $\sigma$  ranges to denote those centralized at the median value and covering 68%, 95%, and 99.7%, respectively, of the probability mass for any probability distribution.

## 2 THE CONTEXT OF GALAXY FORMATION

Our goal is to develop a paradigm to understand the formation of GCs in the current cosmological framework of galaxy formation. Due to the large dynamic range covered by our model, we structure it in a hierarchical way, from large scales of low density to small scales of high density. The basic idea behind the hierarchy is to introduce different physical and numerical models to describe the ‘jumps’ in characteristic scales, and to join them with recipes describing their interfaces. Thus, we start with modeling the structure formation at large scales, and use the results as boundary conditions, i.e. ‘environments’, for the next step on smaller scales. The first scale, describing the large-scale structures of the cosmic density field and its interface with the second scale, which describes dark matter halos, is modeled using results from cosmological N-body simulations. Models of galaxy formation and the growth of SMBH are built on halos and their merger trees, using the two-phase paradigm described in [Paper-I](#), which bridges the interface between halos and galaxies. Gas fragmentation and star formation are modeled by a new recipe developed in this paper, which bridges the gap to the fourth scale, sub-clouds in galaxies, where globular clusters form. Fig. 1 shows the overall context of our model, where the two-point auto-correlation function of globular clusters, predicted by our model, is shown to represent the scales and densities of the structures in question. The spatial and density scales of relevant gas processes (e.g. mass accretion, gas cooling, fragmentation and compression) and the corresponding structures (large-scale structure, halos, galaxies, and sub-clouds) are marked for reference. This plot demonstrates schematically how the formation of GCs fits in the general cosmological context, and how the related physical processes define the characteristic scales involved in our problem. In what follows, we describe these processes in more detail.

### 2.1 The assembly of dark matter halos

Our modeling of the halo population is based on a sample of halos and merger trees constructed from numerical simulations of the current  $\Lambda$ CDM cosmology, as described in §4. For each subhalo merger tree rooted in a ‘root subhalo’ (i.e. the subhalo without a descendant), we decompose it into a set of disjoint branches using the method described in [Chen et al. \(2023\)](#), see their §3.2.1). This is equivalent to traversing over the tree in a depth-first order starting from the root subhalo, and extracting each subsequent segment of the tree bracketed by a subhalo and its main leaf. For each branch, we find the last snapshot when it is a central subhalo, and define this snapshot as the ‘infall snapshot’. The assembly history at and before this snapshot is defined as the ‘central stage’ of the branch, while that after it is defined as the ‘satellite stage’.

In the central stage, galaxy formation (and SMBH growth) are modeled according to the two-phase model described in [Paper-I](#). In this paper, we extend the previous model to include the recipes for the satellite stage. A model for the formation of globular clusters is then built upon this extended galaxy model, as to be described in §3.

For each branch in the merger tree, we smooth its virial mass

history,  $M_v(z)$ , by a running Gaussian kernel with a width equal to the dynamical timescale,  $t_{\text{dyn}} = R_v(z)/V_v(z) = 1/[10H(z)]$ , where  $R_v(z)$  and  $V_v(z)$  are, respectively, the virial radius and virial velocity of the halo, and  $H(z)$  is the Hubble parameter, all evaluated at the redshift  $z$  in question. Smoothed versions of other virial quantities are defined using the smoothed  $M_v(z)$ , while histories of other relevant halo quantities are smoothed using the same window as that used for  $M_v(z)$ . The smoothing is required to ensure the numerical stability of our model implementation. Note that we do not aim to model the short-time-scale variations in the properties of halos, galaxies and star clusters, but intend to model the long-time-scale averages. The results of our model should thus be understood as an ‘effective’ description over a timescale of  $\gtrsim t_{\text{dyn}}$ .

As discussed in [Paper-I](#), the assembly history of a halo can in general be separated into a fast phase, where  $V_v$  increases rapidly with time, followed by a slow phase where  $V_v$  remains roughly constant (e.g. [Zhao et al. 2003](#)), and galaxy formation in these two phases is expected to have very different characteristics. We thus model the two phases separately using different recipes. To this end, we identify, for the central stage of each branch, a transition redshift,  $z_f$ , at which the halo assembly transits from the ‘fast phase’ to the ‘slow phase’. The details can be found in [Paper-I](#). Briefly, we first fit the halo mass assembly history to the following functional form,

$$\ln M_v(z) = c_0 + c_1 \frac{z}{1+z} + c_2 \ln(1+z) + c_3 z, \quad (1)$$

where  $c_0$ ,  $c_1$ ,  $c_2$  and  $c_3$  are fitting parameters. We then obtain the specific halo growth rate, defined as  $\gamma(z) \equiv \dot{M}_v(z)/[H(z)V_v(z)]$ , from the fitting function. Finally, we determine the redshift at which  $\gamma(z)$  falls below a threshold,  $\gamma_f$ , and define this redshift as  $z_f$ . As our default choice, we set  $\gamma_f = 3/16$ , the central value between the Low- $z_f$  and High- $z_f$  variants used in [Paper-I](#).

The brown curves in the top row of Fig. 2 show the mass assembly histories of three individual halos of different masses. The transition redshift,  $z_f$ , defined above is indicated by the vertical grey line in each panel. For each halo, the mass assembly rate is higher at higher  $z$  and becomes roughly flat at  $z < z_f$ . More examples can be found in [Paper-I](#), where the transition can be seen more clearly in the history of the halo virial velocity,  $V_v(z)$ . To cover the large dynamic range relevant to our model, we use analytical approximations in our description to gain an intuitive understanding of the problem. The actual implementations are performed numerically (see §4.1). In our modeling, many processes are connected to halo properties. We thus list some of the most important halo quantities, their typical values and redshift dependence in the following. Based on the spherical collapse model, the virial velocity of a halo can be approximated as

$$V_v = \left(\frac{\Delta_v}{2}\right)^{1/6} [GM_v H(z)]^{1/3} \quad (2)$$

$$= \begin{cases} \left[80.0 \text{ km s}^{-1}\right] M_{v,10}^{1/3} (1+z)_{10}^{1/2}, \\ \left[138.6 \text{ km s}^{-1}\right] M_{v,11.5}^{1/3} (1+z)_3^{1/2}, \end{cases} \quad (3)$$

where  $1+z = 10(1+z)_{10} = 3(1+z)_3$ ,  $M_v = 10^{10} M_\odot M_{v,10} = 10^{11.5} M_\odot M_{v,11.5}$  and  $\Delta_v = 200$  (e.g. [Mo et al. 2010](#)). The virial radius is

$$R_v = \left(\frac{2GM_v}{\Delta_v}\right)^{1/3} H^{-2/3}(z) \quad (4)$$

$$= \begin{cases} [6.7 \text{ kpc}] M_{v,10}^{1/3} (1+z)_{10}^{-1}, \\ [70.8 \text{ kpc}] M_{v,11.5}^{1/3} (1+z)_3^{-1}. \end{cases} \quad (5)$$

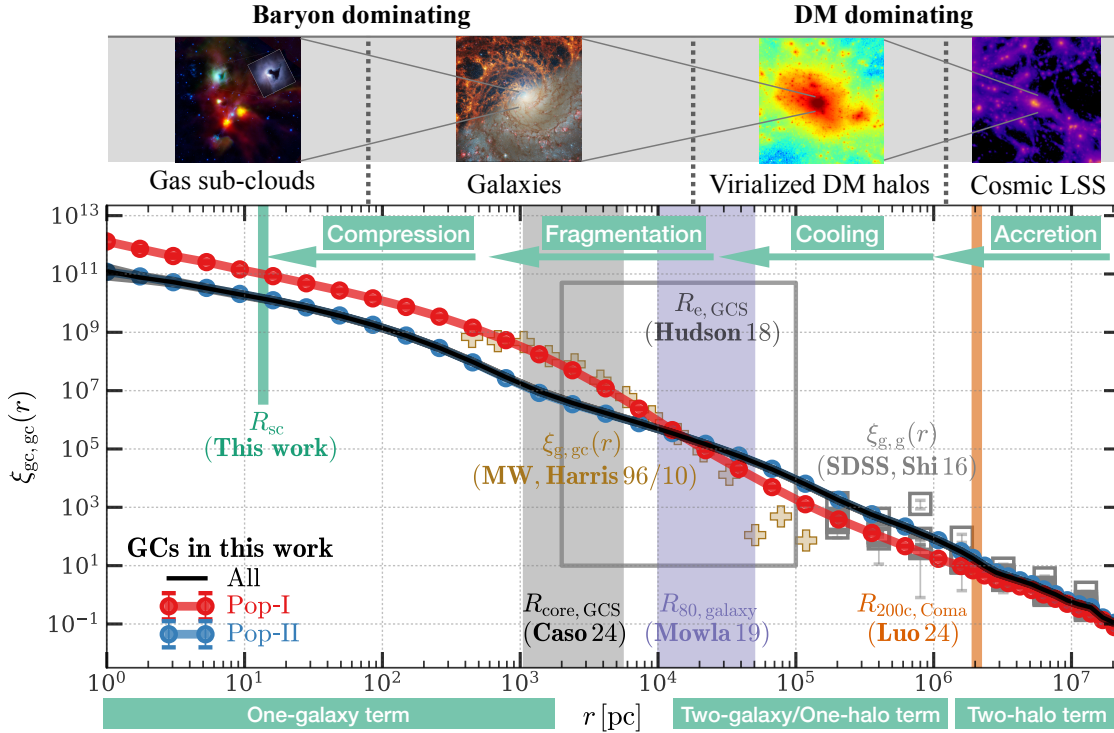


**Figure 1.** Two-point auto-correlation functions of GCs at  $z = 0$  predicted by the model in this paper. **Black, red, and blue** curves show the results for all, Pop-I and Pop-II GCs, respectively, with errorbars or shaded areas showing the standard deviation computed using 20 bootstrap samples. **Vertical lines/shaded areas** mark the typical scales of structures. **Green line** indicates  $R_{sc}$ , the typical size of GC-forming sub-clouds derived in this paper (§§3.4 and 4.3). **Grey shaded area** indicates the core radius,  $R_{core,GCS}$ , below which GC profile presents flattening, obtained by [Caso et al. \(2019\)](#), [De Bortoli et al. \(2022\)](#) and [Caso et al. \(2024\)](#) for a sample of early-type galaxies with  $M_* \gtrsim 10^9 M_\odot$  in the local volume. Here we show the 5<sup>th</sup>-95<sup>th</sup> percentile range of their sample. **Grey rectangle** indicates the effectively radius,  $R_{e,GCS}$ , of GC systems for galaxies with  $M_* > 10^{10.5} M_\odot$ , compiled by [Hudson & Robison \(2018\)](#), see their figure 12). **Purple shaded area** indicates the range of  $R_{80,galaxies}$ , the 80%-light radius in optical band, for galaxies with  $M_* > 10^{10.5} M_\odot$ , obtained by [Mowla et al. \(2019\)](#). **Orange line** indicates the radius of the Coma cluster simulated by [Luo et al. \(2024\)](#) based on the constrained density field. Other markers show the observations at different scales. **Brown markers** show the galaxy-GC cross-correlation function obtained by the Milky Way GCs compiled by [Rodríguez et al. \(2023\)](#) based on the catalog of [Harris \(1996, 2010\)](#). **Grey markers** show the real space galaxy-galaxy auto-correlation functions obtained by [Shi et al. \(2016\)](#), see their figure 10 and table 3) for a sample of flux-limited SDSS galaxies in a number of bins of  $M_r$ , based on their correction method for the redshift-space distortion. This figure demonstrates the overall context of our model for the formation of halos, galaxies and star clusters. See §2 and §3 for the details of the model, and §4.6 for the description of this figure.

The accretion rate of a halo, calibrated by simulations ([Dekel et al. 2013](#)), can be approximated as

$$\dot{M}_v = \begin{cases} [49.8 M_\odot/\text{yr}] M_{v,10}^{1.14} (1+z)_{10}^{2.5}, \\ [125.9 M_\odot/\text{yr}] M_{v,11.5}^{1.14} (1+z)_3^{2.5}. \end{cases} \quad (6)$$

## 2.2 The collapse of the gas component

As gas gets accreted into a halo, it can cool and contract until it becomes self-gravitating or supported by rotation. One important conclusion of the two-phase model developed in [Paper-I](#) is the association of the formation of dynamically hot stellar systems and SMBHs with the self-gravitating, turbulent gas cloud (referred to as the SGC) expected during the fast accretion phase of the dark matter halo, while the formation of a stable, angular-momentum supported disk is associated only with the slow phase. The basic arguments can be summarized as follows.

- During the early, fast-accreting stage of halo assembly ( $z \gtrsim z_f$ ) and if  $\dot{M}_v(z) \lesssim 10^{12} M_\odot$ , the cooling timescale of the halo gas is shorter than the free-fall timescale ( $t_{cool,halo} < t_{ff,halo}$ ), so that cold gas can flow in free-fall to the center of the halo. Thus, before stars and SMBHs can drive a large fraction of the gas from the

halo, the galaxy that forms in the halo center is expected to be gas-rich, and the baryon fraction of the galaxy roughly follows the universal baryon fraction,  $f_B \sim 0.15$ . With such a high fraction, the contraction of the cooled halo gas will become self-gravitating (thus forming an SGC) before it can be supported by angular momentum. Gas motion is expected to be turbulent in such an SGC because of the fast mass assembly and effective cooling. In the presence of effective cooling, the SGC is also expected to fragment into sub-clouds due to gravitational instabilities, and the sub-clouds formed in this way should inherit the turbulent motion generated by the rapid gravitational collapse. Shocks associated with the turbulent motion can compress sub-clouds to higher density, which allows them to move ballistically without being affected significantly by ram pressure and cloud-cloud collision. Stars that form in the dense sub-clouds also inherit the random motion, forming a dynamically hot stellar system such as the bulge of a galaxy. Sub-clouds with sufficiently low angular momentum can reach the halo center to feed the central SMBH, producing feedback effects that can reduce the amount of cold gas.

- In the intermediate stage where feedback from stars and SMBHs can heat/eject large amounts of the gas from the galaxy, a disk may form. However, if the halo is still in the fast accretion regime, frequent



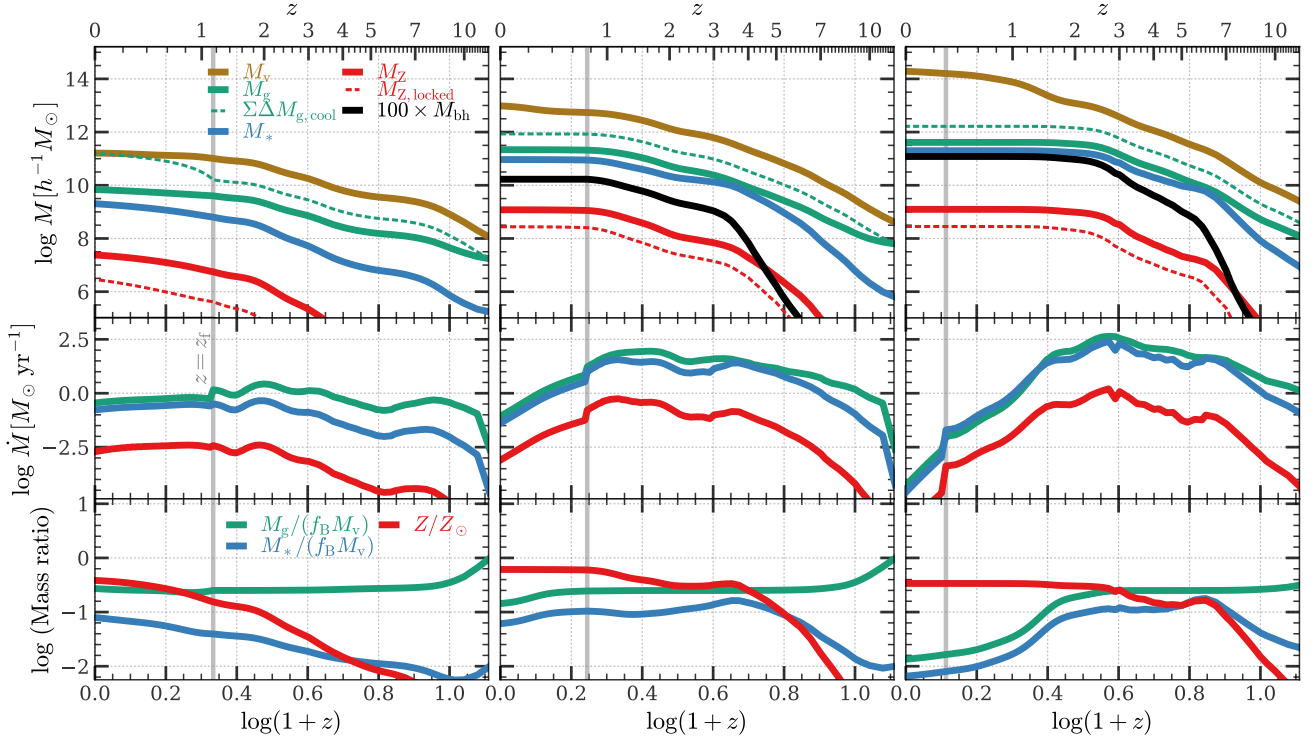


**Figure 2.** History of different mass components predicted by the galaxy model. **Each column** shows the results for an example halo and its central galaxy. Three **rows** show the cumulative mass, the increase rate of mass, and the ratio of two masses, respectively, as indicated in the legends. **Brown, green, blue, red and black** curves show the results for halo, gas, stars, gas-phase metal and central SMBH, respectively. For gas, the **solid** and **dashed** curves show the total gas mass within the galaxy, and the cumulative mass of cooled gas. For metal, the **solid** and **dashed** curves show the total oxygen mass within the galaxy, and the cumulative mass of oxygen locked into stars and SMBHs. In each panel, the **vertical grey** line marks the transition redshift,  $z_f$ , at which halo assembly transits from the ‘fast phase’ to the ‘slow phase’. See §2 for the detailed definition of masses, their evolution equations, and the description of this figure.

interactions and mergers can thicken or even destroy the disk. If the galaxy remains gas-rich (with the gas fraction much higher than the effective spin of the gas) after transiting to the slow accretion phase, the formed disk structure will be too dense to be stable, which may lead to the transformation of the disk into a bar or a pseudo-bulge. Thus, a stable and thin disk is not expected in this stage, while other dynamically hot stellar components, as well as the central SMBH, may continue to grow.

- In the late stage where the halo has transited to the slow accretion phase and feedback has reduced the gas fraction to a value that is comparable to or lower than the effective spin of the gas, a long-lasting, angular momentum supported thin disk forms.

In any of the above stages, the galaxy may temporarily or permanently stop forming stars and become quenched, if the halo has grown massive enough ( $M_v \gg 10^{12} M_\odot$ ) so that cooling becomes inefficient, and/or if feedback effects have ejected most of the gas from the halo. In addition, if the galaxy is accreted into another halo of larger mass and becomes a satellite, environmental processes may also play a role in quenching the galaxy.

The above ‘two-phase’ scenario leads to a prediction that most of the central galaxies have undergone a transition from a dynamically hot phase to a dynamically cold phase driven by the transition in the halo assembly history. Therefore, many of the equations in the following will be presented separately for the two phases: the fast one at  $z \geq z_f$  and the slow one at  $z < z_f$ . The formulations and fiducial parameters are designed and calibrated as in Paper-I. The extensions needed to model the formation of globular clusters (GCs) are described in the next section.

The model starts from the gas accretion associated with the halo assembly. At each time step, the total amount of halo gas available for subsequent processes is determined by the mass assembly history of the halo:

$$\Delta M_{g,avail} = \begin{cases} f_B \Delta M_v, & \text{if } z \geq z_f, \\ \frac{f_B M_v}{\tau(z)} \Delta t, & \text{if } z < z_f. \end{cases} \quad (7)$$

where  $f_B$  is again the cosmic baryon fraction,  $\tau(z) = (1+z)^{-3/2}/(10H_0)$  is an approximation to the dynamical timescale of the halo, and  $\Delta t$  is the time span of the step. Note that the equation in the second line expresses the available gas mass in terms of the halo mass,  $M_v$ , instead of  $\Delta M_v$ . This is motivated by the fact that the halo mass may stop increasing significantly in the slow phase, while the gas already in the halo is still available to feed star formation and SMBH growth.

The initial density of the gas accreted into the halo is below the threshold of star formation. As it cools, the halo gas contracts to a radius of about  $f_{gas} R_v$  where it becomes self-gravitating, forming an SGC (see Paper-I). The typical density of SGC is thus

$$\begin{aligned} n_{sgc} &= \frac{f_{str} f_{gas} M_v}{(4\pi/3)(f_{gas} R_v)^3 \mu m_p} \\ &= f_{str} \frac{n_{B,0} \Delta v}{\mu f_{gas}^2 f_B} (1+z)^3 \\ &= f_{str,4} f_{gas,0.04}^{-2} \times \begin{cases} [663.24 \text{ cm}^{-3}] (1+z)_0^3, \\ [17.91 \text{ cm}^{-3}] (1+z)_3^3, \end{cases} \end{aligned} \quad (8)$$

where the cosmic baryon number density  $n_{B,0} = 3H_0^2 f_B \Omega_m / (8\pi G m_p) \approx 2.48 \times 10^{-7} \text{ cm}^{-3}$ ,  $\Delta_v = 200$ ,  $f_{\text{gas}} = 0.04 f_{\text{gas},0.04}$ ,  $\mu = 1.2$ . The factor  $f_{\text{str}}$  characterizes the ‘streamness’ of the gas inflow. For spherically symmetric contraction,  $f_{\text{str}} = 1$ , and the typical value of  $f_{\text{gas}}$ , 0.04, is regulated by feedback (see [Chen et al. 2024](#), hereafter Paper-II). For cold-mode streams,  $1 < f_{\text{str}} \leq f_B / f_{\text{gas}} \approx 4$ , as gas can penetrate into a galaxy along filaments and a larger fraction of gas can pile up around the halo center. [Mandelker et al. \(2018\)](#) and [Dekel et al. \(2023\)](#) estimated that the effective radius of streams is about  $0.043 R_v$ , similar to the contraction factor based on  $f_{\text{gas}}$ . The SGC density given by Eq. (8) is much lower than the supernova-free threshold  $n_{\text{snf}} \approx 10^{3.5} \text{ cm}^{-3}$  required to form GCs (see §3.5) at  $z = 2$ , and marginally touches the threshold at  $z = 9$ . Thus, additional processes within SGCs are required for the formation of GCs in galaxies.

For halos with  $M_v \gtrsim 10^{12} M_\odot$ , the cooling time of the halo gas exceeds the free-fall time, so that only a fraction of the gas can cool within a free-fall timescale. We use a factor,  $F_{\text{cool}}$ , to account for the reduction of the cold gas due to inefficient cooling,

$$\Delta M_{g,\text{cool}} = F_{\text{cool}} \Delta M_{g,\text{avail}}. \quad (9)$$

We follow [Paper-I](#) to model  $F_{\text{cool}}$ :

$$F_{\text{cool}} = \begin{cases} \left[ 1 + \left( \frac{M_v}{M_{\text{cool}}} \right)^{\beta_{\text{cool},f}} \right]^{-1}, & \text{if } z \geq z_f, \\ \left( 1 + \frac{M_v}{M_c} \right)^{-\beta_{\text{cool},s}(z)}, & \text{if } z < z_f, \end{cases} \quad (10)$$

where we take  $M_{\text{cool}} = 10^{13} h^{-1} M_\odot$ ,  $\beta_{\text{cool},f} = 4$ ,  $\beta_{\text{cool},s} = 3.6(1+z)^{-0.72}$ , and  $M_c = 10^{11.9} h^{-1} M_\odot$  as our fiducial values of the model parameters. The redshift dependence in the fast phase comes implicitly from the redshift dependence of the halo mass, while in the slow phase, it comes explicitly from the redshift dependence of the power index (as in Model-II of [Lu et al. 2014](#), hereafter L14). The remaining fraction,  $1 - F_{\text{cool}}$ , of the halo gas is referred to as the ‘hot’ gas.

In the top row of Fig. 2, the dashed green lines show the time evolution of  $M_{g,\text{cool}}$ , the cumulative mass of the cooled gas, in central galaxies of three example halos of different masses. For halos with mass smaller than the cooling threshold ( $M_{\text{cool}}$ ) and in the fast phase ( $z \geq z_f$ ), the amount of cooled gas tightly follows the total available baryons, with the mass roughly proportional to  $f_B M_v(z)$ , as shown in the left and middle panels. For massive halos, cooling becomes inefficient and the accumulation of cooled gas is stalled once its mass reaches  $M_{\text{cool}}$ , as shown in the right panel. In the slow phase and if the halo mass is sufficiently small, as is the case shown in the left panel, the gas that is heated and ejected from the galaxy may cool down and recycle back to the galaxy to feed further star formation. This is why the accumulative inflow mass of cooled gas can exceed  $f_B M_v(z)$ , as seen at  $z < 1$  in the left panel.

### 2.3 Star formation, SMBH growth and feedback

The amount of cooled gas can be affected by the feedback from supernova (SN) explosions associated with star formation and active galactic nuclei (AGN) associated with the growth of SMBHs. Thus, the amount of star-forming gas,  $\Delta M_{g,\text{sf}}$ , is modulated by two additional factors, one for each source of feedback:

$$\Delta M_{g,\text{sf}} = F_{\text{sn}} F_{\text{agn}} \Delta M_{g,\text{cool}}. \quad (11)$$

Part of the feedback-affected gas is ejected from the galaxy (ejected gas), while the rest remains in the galaxy as a hot medium and is

prevented from forming stars (prevented gas). Following [Paper-I](#), we model the amounts of ejected and prevented gas as

$$\Delta M_{g,\text{ej}} = f_{\text{ej}} (1 - F_{\text{sn}} F_{\text{agn}}) \Delta M_{g,\text{cool}}, \quad (12)$$

and

$$\Delta M_{g,\text{prev}} = (1 - f_{\text{ej}}) (1 - F_{\text{sn}} F_{\text{agn}}) \Delta M_{g,\text{cool}}, \quad (13)$$

respectively. Here,  $F_{\text{sn}}$  is given by

$$F_{\text{sn}} = \begin{cases} \frac{\alpha_{\text{sn},f} + (V_g/V_w)^{\beta_{\text{sn},f}}}{1 + (V_g/V_w)^{\beta_{\text{sn},f}}}, & \text{if } z \geq z_f, \\ \left( \frac{M_v/M_c}{R + M_v/M_c} \right)^{\beta_{\text{sn},s}}, & \text{if } z < z_f, \end{cases} \quad (14)$$

where  $\alpha_{\text{sn},f} = 0$ ,  $\beta_{\text{sn},f} = 2.5$ ,  $V_w = 250 \text{ km s}^{-1}$ ,  $R = 10^{-0.96}$ ,  $\beta_{\text{sn},s} = 1.9$ , and  $V_g = V_{\text{max}}$  is the typical velocity dispersion of the galaxy.  $F_{\text{agn}}$  is given by

$$F_{\text{agn}} = \begin{cases} 1 - \frac{\alpha_{\text{agn},f} M_{\text{bh}} c^2}{M_g V_g^2}, & \text{if } z \geq z_f, \\ \left( \frac{R + M_v/M_c}{1 + M_v/M_c} \right)^{\beta_{\text{agn},s}}, & \text{if } z < z_f, \end{cases} \quad (15)$$

where  $\alpha_{\text{agn},f} = 10^{-3}$ ,  $\beta_{\text{agn},s} = 1.8$ , and  $M_{\text{bh}}$  and  $M_g$  are the masses of central SMBH and the gas within the galaxy (equations describing their evolution are given below), respectively. Modeled in this way, the effects of the SN and AGN feedback are constrained by the gravitational potential of the host halo, which is needed to reproduce the observed  $M_*$ - $M_v$  relation at the low-mass ( $\approx 10^8 M_\odot$ ) end ([Yang et al. 2012a](#)) and the scaling relation of  $M_{\text{bh}}$ - $M_{*,\text{bulge}}$  ([Graham & Sahu 2023](#)). The fraction of ejected gas is set to be  $f_{\text{ej}} = 0.75$  for the fast phase. This choice was made in [Paper-I](#) to ensure that the gas fraction in a feedback-regulated galaxy is comparable to the typical spin,  $\lambda \approx 0.04$ , so that a switch from bulge formation to disk formation can occur after the fast phase. For the slow phase, we set  $f_{\text{ej}} = 1$ . Note that in the slow phase, the hot ISM component represented by  $\Delta M_{g,\text{prev}}$  is degenerate with the remaining part of  $\Delta M_{g,\text{sf}}$  after the consumption of star formation, so that  $f_{\text{ej}}$  is degenerate with  $F_{\text{sn}}$  and  $F_{\text{agn}}$ , and the star formation efficiency of the star-forming gas,  $\Delta M_{g,\text{sf}}$ . Once the star formation efficiency is fixed, the choice of  $f_{\text{ej}}$  does affect the gas fraction in the galaxy. The roughly constant gas fraction shown by the green curve in the bottom left panel of Fig. 2 indicates a gas fraction of  $M_g/M_v \approx \lambda \approx 0.04$ . Such a gas fraction allows a transition from bulge to disk at the end of the fast phase, and the formation of a stable disk in the slow phase (see §3.2 of [Mo et al. 1998](#)), suggesting that the gas fraction predicted by our choice for  $f_{\text{ej}}$  is reasonable.

The star formation rate is assumed to be proportional to the generation rate of star-forming gas:

$$\Delta M_* = \epsilon_* \Delta M_{g,\text{sf}}, \quad (16)$$

where  $\epsilon_* = 0.75$  and  $0.32$  for the fast and slow phases, respectively, as calibrated in [Paper-I](#). Here, we assume instantaneous evolution, as the timescale of stellar evolution is usually much shorter than the dynamical timescale of the halo. Thus, the stellar mass modeled above should be treated as the remaining mass modulated by stellar evolution. The instantaneous star formation rate can be obtained by

$$\text{SFR} = \frac{1}{1 - R} \frac{\Delta M_*}{\Delta t}, \quad (17)$$

where  $R = 0.4$  is the returned fraction of mass assuming a Chabrier IMF ([Bruzual & Charlot 2003](#)). For small-scale processes, such as

the formation of globular clusters, the timescale of stellar evolution is critical in setting the time window for star formation. We will discuss this in detail in §3.

The growth of SMBH is determined by the fraction of low-angular-momentum gas that can reach the halo center to feed the central SMBH. Following the arguments in Paper-I, we model it as

$$\Delta M_{\text{bh}} = \alpha_{\text{cap}} \frac{M_{\text{bh}}}{M_{\text{g}}} F_{\text{en}} \Delta M_{\text{g},\text{sf}}, \quad (18)$$

where  $\alpha_{\text{cap}} = 2.5$  in the fast phase, and  $\alpha_{\text{cap}} = 0$  in the slow phase due to the full mixing of gas. The enhancement factor,  $F_{\text{en}}$ , which describes the enhancement of turbulence by SN feedback, is modeled as

$$F_{\text{en}} = \frac{\alpha_{\text{en}} + (M_{\text{v}}/M_{\text{en}})^{\beta_{\text{en}}}}{1 + (M_{\text{v}}/M_{\text{en}})^{\beta_{\text{en}}}}, \quad (19)$$

where  $\alpha_{\text{en}} = 3$ ,  $\beta_{\text{en}} = 2$ , and  $M_{\text{en}} = 10^{11.5} h^{-1} M_{\odot}$ . The dependence on halo mass comes from the evidence that SN feedback on galactic scales is only effective in low-mass halos. As discussed in Paper-I, this enhancement factor is needed to boost the formation of the seeds for growing SMBHs.

Finally, the change in the amount of gas within a galaxy is determined by the combination of cooling, star formation, SMBH growth, and feedback. Using mass conservation, we can write

$$\Delta M_{\text{g}} = \Delta M_{\text{g},\text{sf}} - \Delta M_{*} - \Delta M_{\text{bh}} + \Delta M_{\text{g},\text{prev}}. \quad (20)$$

For a galaxy that has entered the satellite stage, we model its star formation rate with an exponential form,

$$\dot{M}(t) = \dot{M}(t_{\text{inf}}) \exp\left(-\frac{t - t_{\text{inf}}}{\tau_{\text{sat}}}\right), \quad (21)$$

where  $t_{\text{inf}}$  is the infall time of the galaxy and  $\tau_{\text{sat}} = 4 \text{ Gyr}/\ln 10$  is the decay timescale. This parameterization is motivated by observational results (e.g. Peng et al. 2015). The amount of gas is determined according to the ‘close-box’ model with instantaneous recycling: gas inflow is cut off as a result of environmental effects; the feedback-affected gas is instantaneously recycled into the ISM. Thus, the amount of remaining gas decreases only by the consumption of star formation. The growth of the SMBH is assumed negligible in this stage.

Galaxy mergers are modeled by adding a fraction,  $f_{\text{merge}}$ , of the stellar mass of the satellite galaxy into the central galaxy. The remaining stars are assumed to be tidally stripped or scattered into the halo to become intracluster light (ICL). The fiducial value,  $f_{\text{merge}} = 0.1$  is taken from Model-II of L14. However, we note that this value is highly uncertain because of the complicated details of mergers and the degeneracy with other model parameters. This value also depends on the definition of the galaxy stellar mass in observations, i.e. the boundary used to separate galactic stars from intergalactic stars and the aperture used in deriving the stellar mass. To quantify this uncertainty, we bracket  $M_{*}$  by two extremes: one only includes stars that have formed in the main branch ( $f_{\text{merge}} = 0$ ), and the other includes stars that have formed in both the main branch and all the side branches ( $f_{\text{merge}} = 1$ ). The resulted  $M_{*}-M_{\text{v}}$  relations for these two extremes, shown by the green curves in Fig. 12 (see §4.4 for details), suggest a significant contribution by ex-situ stars at  $M_{\text{v}} \gtrsim 10^{13} M_{\odot}$ . Interpretations of our results involving  $M_{*}$  should thus take into account this uncertainty. When counting the total number and mass of GCs in a galaxy (see §4.1), we instead include all GCs formed in satellites that have merged into the central, based on the fact that observations of GCs usually adopt a large aperture (e.g. Dornan & Harris 2023).

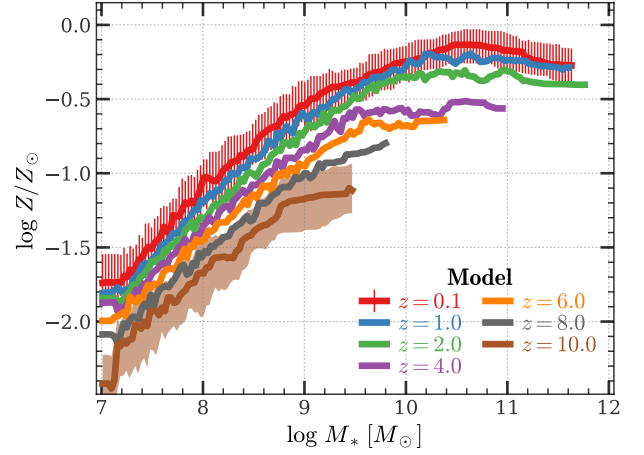


**Figure 3.** Stellar mass-metallicity relation for central galaxies at different redshifts. Each solid curve shows the running median. Error bars and shaded area at two redshifts show the  $1-\sigma$  range. See §2.4 for details.

## 2.4 Metal enrichment

Gas-phase metallicity,  $Z \equiv M_{\text{Z}}/M_{\text{g}}$ , of galaxies is modeled according to the ‘gas-regulator’ scenario (Lilly et al. 2013; Peng et al. 2015; Wang & Lilly 2021), as our modeling of the SFR is based on the amount of available gas and fits in the framework of the gas regulator. However, certain modifications are needed to account for uncertainties in the metal enrichment related to the formation of GCs. One uncertainty arises from the possibility that high- $z$  galaxies may be fed by cold streams, as suggested by numerical simulations (e.g. Keres et al. 2005; Ceverino et al. 2010; Danovich et al. 2015; Mandelker et al. 2018; Lapiner et al. 2023). Cold streams with small cross section can transport pristine gas into the galaxy, leading to the formation of metal-poor stars, as suggested by observations (Lin et al. 2023), analytical estimations (Li et al. 2024) and hydrodynamical simulations (Mandelker et al. 2018). Another uncertainty comes from the expectation that high- $z$  galaxies are much more clumpy and that their star formation is more bursty than in the local Universe, as detailed in Paper-I. Metal yields from stars at high  $z$  may thus be coupled to the ISM and IGM in a way very different from that in a more steady and quieter environment expected at low  $z$ . One way to deal with these uncertainties is to directly use the observed relations of the metallicity with other galaxy properties that can be modeled reliably. This approach, however, is limited by the size and quality of observational data, the selection bias, and uncertainties in, e.g., tracers and calibrations used to infer the metallicity. It is also not guaranteed that the observed relation can be applied to modeling the GCs, as the environment of GCs may differ significantly from the average over an entire galaxy. Indeed, the GC catalog produced by post-processing the FIRE-2 zoom-in simulation, which is claimed to be able to reproduce the observed stellar mass-metallicity relation up to  $z = 12$  (Marszewski et al. 2024), misses the old (born at  $z > 3$ ), metal-poor population observed in the Milky Way (Grudić et al. 2023).

In this paper, we choose to modify some recipes in the gas-regulator model to account for the aforementioned uncertainties, while keeping the overall framework unchanged. The formulation and calibration used here thus only apply to the modeling of GCs, and may not be suitable for other purposes. Following the formulation of Lu et al. (2015), we relate the change of the oxygen mass,  $\Delta M_{\text{Z}}$ , by the combination of inflow, stellar yield, star formation consumption,

and feedback ejection. Thus, the continuity equation for the oxygen mass is

$$\Delta M_Z = Z_{\text{IGM}} \Delta M_{\text{cool}} + y_{\text{eff}} \frac{\Delta M_*}{1 - R} - (\Delta M_* + \Delta M_{\text{bh}}) Z, \quad (22)$$

where the three terms on the right-hand side are referred to as the inflow, yield and locked metal masses, respectively. Thus,  $Z_{\text{IGM}}$  is the metallicity of the inflow gas,  $y_{\text{eff}}$  is the effective oxygen yield that incorporates the intrinsic yield of stars, the escape of decoupled fraction, the ejection by stellar feedback, and the recycling due to cooling; Note that gas ejection and recycling has been absorbed into the effective yield,  $y_{\text{eff}}$ , so that this factor accounts for the net effects of ejection and recycling. Each of the terms in the above equation has uncertainties. To proceed, we make the following assumptions:

- (i) We set  $Z_{\text{IGM}} = 0$  if the metallicity of the inflow gas is much lower than that of the ISM.
- (ii) A constant returning fraction  $R$  (Eq. 17) is adopted. Instantaneous recycling is also assumed here, because the timescale of stellar evolution is much shorter than the dynamical timescale of the halo – roughly 80% of the oxygen is released during the first 10 Myr by the Type-II SNe (Maiolino & Mannucci 2019).
- (iii) The effective yield is defined as

$$y_{\text{eff}} = y(1 - f_{\text{esc}})f_{\text{mix}}. \quad (23)$$

where we adopt the intrinsic oxygen yield  $y = 0.0163$  (Portinari et al. 1998), as it is consistent with a broad range of stellar evolution models in the literature. Other models (e.g. Henry et al. 2000; Kobayashi et al. 2006) give different values, but generally within 0.3 dex. The escaped fraction,  $f_{\text{esc}}$ , depends on the details of wind coupling, gas ejection and recycling, and is hard to model. Therefore, we choose to model it empirically as

$$f_{\text{esc}} = \frac{1 + \alpha_{\text{esc}} x_v}{1 + x_v}, \quad (24)$$

where  $x_v = (V_{\text{max}}/V_{\text{esc}})^{\beta_{\text{esc}}}$  and  $\alpha_{\text{esc}} = z/(z_{\text{esc}} + z)$ . The dependence on  $V_{\text{max}}$  is motivated by the fact that the coupling and ejection of stellar winds in general depend on the depth of the gravitational potential well of the host halo, and the dependence on redshift is motivated by the fact that the overall gas density and clumpiness, and thus the local dynamical timescale and cooling rate, depend on redshift. The mixing factor,  $f_{\text{mix}}$ , which characterizes the efficiency of metal mixing between the inflow gas and the existing ISM, is expected to be lower for faster accretion and thus defined as

$$f_{\text{mix}} = \frac{1}{1 + x_\gamma}, \quad (25)$$

where  $x_\gamma = |\gamma/\gamma_0|^{\beta_{\text{mix}}}$ . We find that  $V_{\text{esc}} = 75 \text{ km s}^{-1}$ ,  $\beta_{\text{esc}} = 2$ ,  $z_{\text{esc}} = 5$ ,  $\gamma_0 = 1$ , and  $\beta_{\text{mix}} = 2$  yield a good fit to the observations (see Appendix B for the calibration).

With the above assumptions, Eq. (22) becomes

$$\Delta M_Z = y_{\text{eff}} \frac{\Delta M_*}{1 - R} - (\Delta M_* + \Delta M_{\text{bh}}) Z. \quad (26)$$

Taking the result of  $\Delta M_*$ ,  $\Delta M_{\text{bh}}$  and  $M_g$  from the equations described in §2.3, we can integrate Eq. (26) over time to obtain  $Z$  for each galaxy.

Fig. 3 shows the stellar mass-metallicity relation (MZR) at various redshifts from  $z = 0$  to 10. Due to the redshift dependence of  $f_{\text{esc}}$  and  $f_{\text{mix}}$ , the modeled MZR shows a steady evolution across the entire redshift range. Low-mass galaxies ( $M_* \lesssim 10^{10} M_\odot$ ) become more enriched as their stellar mass grows, because the star formation efficiency ( $M_*/M_g$ ) increases monotonically with  $M_*$ , as seen from the blue and green curves in the bottom row of Fig. 2. High-mass

galaxies ( $M_* \gtrsim 10^{10} M_\odot$ ) shows saturated metallicity, because gas accumulation, and thus star formation, are stalled due to AGN feedback and inefficient cooling. The assembly of stellar mass for these galaxies is mainly due to gas-poor (dry) mergers, without significant metal yield. The slope in logarithmic scale at the low-mass end shows slow evolution, from 0.6 at high  $z$ , to 0.7 at low  $z$ . This is a consequence of including  $f_{\text{mix}}$ , which suppresses the mixing of low-metallicity inflow gas with existing enriched ISM, for halos at high accretion rates.

In the following, whenever we need an analytical approximation of the MZR to give a rough estimate of the results, we will use the following relation obtained by fitting our modeled galaxies:

$$\log \frac{Z}{Z_\odot} = 0.6 \log \left( \frac{M_*}{10^9 M_\odot} \right) - 0.55 \log(1 + z) - 0.5, \quad (27)$$

For a halo with mass  $M_v$  and star formation efficiency  $\epsilon_v \equiv M_*/(M_v f_B)$ , the average metallicity is thus

$$Z/Z_\odot = \epsilon_{v,0.1}^{0.6} \times \begin{cases} 0.029 M_{v,10}^{0.6} (1+z)^{-0.55}, \\ 0.45 M_{v,11.5}^{0.6} (1+z)^{-0.55}. \end{cases} \quad (28)$$

The model of galaxy formation described in this section focuses on the global properties of galaxies. As described earlier, this provides environmental conditions for small-scale processes related to the formation of GCs. A consequence of this hierarchical strategy is that the spatial distribution of GCs resembles those of the halo and galaxies at large scales, with modifications due to refined processes operating on small scales. In the next section, we will introduce the model of GC formation under the constraints provided by the model of galaxies described above. Note that this top-down approach does not include the details of matter and energy recycling from stars to the gas environment, and thus misses the diversity in the feedback produced by different stellar populations. For example, the IMF in low-metallicity environments is inferred to be top-heavy (Stacy et al. 2016; Latif et al. 2022b; Klessen & Glover 2023), which can alter the evolution paths of individual stars and thus lead to different metal yields (Portinari et al. 1998). More exotic feedback mechanisms can also be present, such as kilonovae (Rosswog et al. 2013; Metzger 2017) and pair-instability supernovae (Woosley et al. 2002; Janka 2012). The inclusion of these populations and related processes may be important in the early Universe, and further exploration is needed in this area.

### 3 THE FORMATION OF GLOBULAR CLUSTERS

A main conclusion of our two-phase model (Paper-I) is the formation of sub-structures, referred to as sub-clouds, once the SGC becomes self-gravitating. In the fast phase, the SGC is expected to be gas-rich and turbulent due to the fast accretion of halo. High-speed winds from SN and AGN can also contribute to the turbulence (Ma et al. 2020; Mercedes-Feliz et al. 2024). Significant compression of the sub-clouds is expected if the turbulence is supersonic, which may produce dense sub-clouds for the formation of GCs we are interested in here. Despite the complexity of the details, it is generally believed that the properties of sub-clouds in a turbulent ISM follow ‘quasi-universal’ laws and distributions, as suggested by both observations (Larson 1981; Lada & Dame 2020) and numerical simulations (Burkhart et al. 2017; Ma et al. 2020; Grudić et al. 2021; Appel et al. 2022; Buck et al. 2022; Kiihne et al. 2025). In this section, we sample the sub-cloud population using these universal distributions under the constraints given by the global properties of SGCs. We then



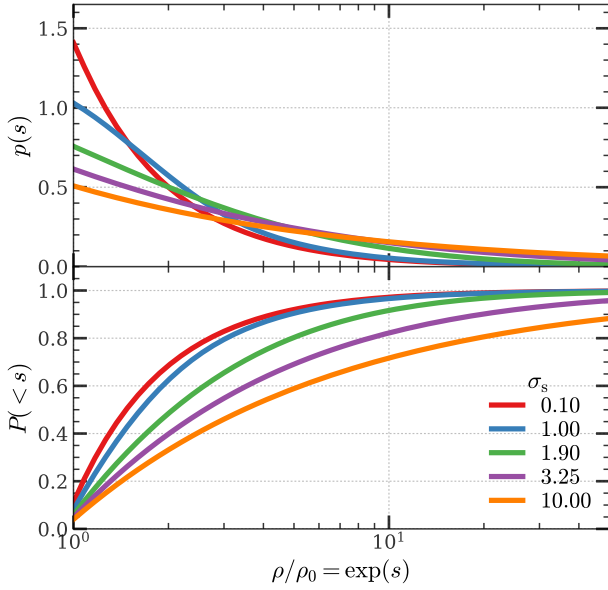


**Figure 4.** The probability distribution of the logarithmic density contrast,  $s \equiv \ln(\rho/\rho_0)$ , of sub-clouds. **Top panel** shows the probability density, while **bottom panel** shows the cumulative distribution. Curves with different colors are obtained by assuming different log-normal dispersion,  $\sigma_s$ . A power-law tail with index  $\alpha_s = 1.5$  is adopted in all cases. See §3.1 for details.

derive the condition for star formation in each sub-clouds, taking into account both external and internal feedback effects on the sub-clouds. We demonstrate that the condition for a sub-cloud to form a GC leads to two distinct channels for GC formation. Finally, we model the disruption and survival of GCs, which is needed to make predictions for comparisons with observations.

### 3.1 The formation of sub-clouds

At formation, an SGC is shock-heated by the release of gravitational potential energy to a temperature determined by the virial temperature of the host halo. Gas cooling in the SGC is efficient, as expected from the high gas density and the high rate of atomic cooling expected at the relevant temperature. The rapid drop of the gas temperature reduces the Jeans mass, and can trigger fragmentation of the SGC into sub-structures. The decline of the temperature is expected to be stalled at  $T_{\text{cool}} \approx 10^4$  K where the cooling rate starts to drop precipitously (e.g. [Smith et al. 2008](#); [Wiersma et al. 2009](#)) and the cooling timescale becomes long. Thermal motion of gas particles in a cloud fragment can thus operate over a sufficient period of time to suppress density fluctuations in the fragment, stabilizing it and preventing it from further fragmentation. The Jeans mass at  $T_{\text{cool}}$  therefore sets a characteristic mass for the fragmentation of SGCs. In this paper, we refer to these self-bound fragments, whose initial temperature is  $T_{\text{cool}}$ , as sub-clouds. Each of these sub-clouds is expected to feature a thermally-supported internal structure and a mass spectrum truncated by the Jeans mass in the high-mass end. The characteristic temperature,  $T_{\text{cool}} \approx 10^4$  K, corresponds to a sound speed of  $c_s \approx 10$  km/s, and the Jeans mass is

$$M_J = v_{\text{eff},10}^3 \times \begin{cases} [5.96 \times 10^7 M_\odot] n_{0,0}^{-1/2}, \\ [1.06 \times 10^6 M_\odot] n_{3,5}^{-1/2}, \end{cases} \quad (29)$$

where  $n_{\text{gas}} = 10^{3.5} \text{ cm}^{-3} n_{3,5} = 1 \text{ cm}^{-3} n_{0,0}$ ,  $v_{\text{eff}} = (c_s^2 + v_{\text{turb}}^2)^{1/2} = 10 \text{ km s}^{-1} v_{\text{eff},10}$ , and  $v_{\text{turb}}$  is the turbulence velocity. By definition,

$v_{\text{turb}} < c_s$ , so that  $v_{\text{eff}} \sim c_s$ . We note that the meaning of the sub-clouds so defined should be distinguished from that of the GMCs in the literature, with the latter usually referring to molecular gas clouds of diverse properties.

The precise mass distribution of sub-clouds depends on the details of how SGCs fragment, and therefore on the temperature, turbulence velocity and density of individual SGCs, as well as on the magnetic and tidal fields they reside in. We do not attempt to trace these details here, but adopt an empirical approach instead. We assume that the mass function of sub-clouds below the truncation mass follows a power-law distribution with an index  $\beta_{\text{sc},m}$ , as expected from scale-free fragmentation of a turbulence-dominated ISM ([Larson 1981](#)). The value of  $\beta_{\text{sc},m}$  is inferred to be  $\approx -2$ , as suggested by the index of the mass function of newly-born massive star clusters in the local Universe ([Zhang & Fall 1999](#); [Fall & Chandar 2012](#); [Adamo et al. 2020](#)) and in the cosmic noon ([Dessauges-Zavadsky & Adamo 2018](#)). The star formation efficiency of massive and dense sub-clouds hosting massive and dense star clusters is expected to be close to unity (see §3.4), and thus the mass spectrum of sub-clouds is expected to be similar to the mass function of star clusters. This value of  $\beta_{\text{sc},m}$  is also reproduced by high-resolution simulations of individual GMCs ([Grudić et al. 2021](#)). With the consideration above, we model the initial mass function for sub-clouds as

$$\frac{dN_{\text{sc}}}{dM_{\text{sc}}} \propto M_{\text{sc}}^{\beta_{\text{sc},m}} \exp\left(-\frac{M_{\text{sc}}}{M_{\text{sc},t}}\right), \quad (30)$$

with  $\beta_{\text{sc},m} = -2$ . The truncation mass  $M_{\text{sc},t} = 10^{6.5} M_\odot$  is set to reflect the Jeans mass given above and the mass limit on the most massive star clusters found in observations (e.g. [Mok et al. 2019](#); [Krumholz et al. 2019](#); see also Fig. 11). The lower and upper bounds of  $M_{\text{sc}}$  are set to be  $M_{\text{sc},\text{min}} = 10^4 M_\odot$  and  $M_{\text{sc},\text{max}} = 10^8 M_\odot$ , respectively. Convergence tests against these choices are made in §4.2.

The presence of supersonic shocks (with Mach number  $\mathcal{M} > 1$ ) can raise the density of sub-clouds and significantly change the density distribution of sub-clouds. As explained in §3.3 of [Paper-I](#), the compressive nature of supersonic turbulence is critical to make the sub-clouds dense enough to survive the drag force by ram pressure and collisions with other sub-clouds. A lack of supersonic turbulence, such as the case where a dynamically-cold disk forms and steady star formation ensues, is expected to terminate the generation of sub-clouds at  $T_{\text{cool}}$  before gas cooling at lower temperature sets a new mass scale,  $M_{\text{sc},t}$ , that is lower than the original truncation mass. Sub-cloud formation in this regime of weak-turbulence may be related to local instabilities, such as those induced by spiral arms and SN feedback, and/or to external perturbations, such as those from interactions with nearby galaxies. On the other hand, sub-clouds in strong turbulence are clustered ([Li et al. 2020](#)). They may thus coalesce to form more massive clouds, raising the value of  $M_{\text{sc},t}$ , or form massive star clusters if rapid star formation can consume the gas before the coalescence (see e.g. Fig. 9 of [Ma et al. 2020](#)). Such a variation of  $M_{\text{sc},t}$  is evident from observations (see §2.2 of [Krumholz et al. 2019](#), for a review), and may be modeled by following the evolution of the turbulence in the SGC. Alternatively, one may start from a parametric model that relates  $M_{\text{sc},t}$  to the galactic environment, such as the gas density, composition and star formation rate density, with necessary calibration from hydrodynamic simulations and observations. Lacking such a model, we adopt a constant value of  $M_{\text{sc},t}$  for simplicity.

The density distribution of sub-clouds in supersonic turbulence, coupled with non-linear star formation and feedback processes, can modify the mass spectrum of sub-clouds and thus that of star clus-

ters formed within them. Major sources of the turbulence may be summarized as follows:

- (i) **Global shocks.** These arise during the formation of an SGC when the inflow gas reaches the core of the host halo, interacts with itself and collides with the existing gas. This is especially important for halos with fast accretion and effective cooling, where cold streams penetrate the halo (corresponding to the Q1 phase described in Paper-I), as suggested by numerical simulations (e.g. Ceverino et al. 2010; Danovich et al. 2015; Mandelker et al. 2018). A global shock can also arise when angular momentum, turbulence and thermal motion of the SGC can no longer support its gravity and it collapses (e.g. Dekel et al. 2009; Dekel & Burkert 2014; Zolotov et al. 2015; Tacchella et al. 2016; Latif et al. 2022a; Ji & Giallisco 2023; Dekel et al. 2023). This is expected to be an important source of turbulence for a gas-rich, slow-rotating SGC (corresponding to the Q2 phase). Gas-rich mergers also produce global shocks and generate gravitational instability due to the pile-up of gas and loss of angular momentum. Such a global shock can propagate outward across the entire SGC, compress the gas, and produce high-density sub-structures.
- (ii) **Local interactions.** These occur when a sub-cloud grows via absorbing surrounding gas, or mergers with nearby sub-clouds. The release of gravitational energy can be effectively dissipated by the effective cooling above  $10^4$  K, so that this process proceeds rapidly and is roughly isothermal. The process continues until sub-clouds become too small and dense enough for them to collide frequently, or until the driving force of the global turbulence disappears. Numerical simulations have shown that such local interactions are critical for the formation of massive and dense sub-clouds (e.g. Latif et al. 2022a; Ma et al. 2020).
- (iii) **Positive feedback.** High-speed winds driven by feedback processes can also drive turbulence and compress sub-clouds to high density. Numerical simulations show that quasar winds (Mercedes-Feliz et al. 2024) and SN winds (Ma et al. 2020) can both lead to the formation of dense stellar clumps reminiscent of YMSCs and GCs. The recent observations by JWST (Pereira-Santaella et al. 2024) and ALMA (Roman-Oliveira et al. 2024) also support the presence of stellar feedback as the driver of turbulence. This channel of turbulence formation exists as long as star formation and/or AGN is active, and thus may cover the entire history of a galaxy.

Turbulence driven by the combination of the above sources creates complex density structure in the SGC. MHD simulations suggest that the volume density of sub-clouds,  $\rho_{sc}$ , follows a piece-wise distribution combining a log-normal piece with a power-law one:

$$p(s) = \begin{cases} \frac{1}{\sqrt{2\pi}\sigma_s} e^{-\frac{(s-s_0)^2}{2\sigma_s^2}}, & \text{if } s \leq s_t, \\ A_s e^{-\alpha_s(s-s_t)}, & \text{if } s > s_t, \end{cases} \quad (31)$$

where  $s = \ln(\rho_{sc}/\rho_0)$  is the logarithmic density contrast,  $\rho_0$  is the mean density of the SGC,  $\sigma_s$  is a free parameter defining the width of the log-normal distribution,  $s_0 = (-1/2)\sigma_s^2$  is the median, and  $\alpha_s$  is the power-law index of the high-density tail. The log-normal piece is found to well represent the isothermal density distribution of a low-density, turbulent ISM (e.g. Burkhart et al. 2009; Myers 2015). The power-law tail at the high density, on the other hand, is expected to originate from compression by self-gravitating collapses and feedback (e.g. Slyz et al. 2005; Collins et al. 2011; Burkhart et al. 2017; Khullar et al. 2021; Appel et al. 2022; Buck et al. 2022; Appel et al. 2022; Kiihne et al. 2025). The continuity of  $p(s)$  and its first

derivative at  $s = s_t$  gives

$$A_s = \frac{1}{\sqrt{2\pi}\sigma_s} e^{-\frac{1}{2}\alpha_s\sigma_s^2}, \quad (32)$$

$$s_t = (\alpha_s - 1/2)\sigma_s^2. \quad (33)$$

So defined, the distribution function has three free parameters,  $\rho_0$ ,  $\sigma_s$  and  $\alpha_s$ , which we obtain as follows:

- (i)  $\rho_0$ , the mean density of the SGC, is predicted by the galaxy model described in §2:

$$\rho_0 = \frac{M_g}{(4\pi/3)(f_{\text{gas}}R_v)^3}. \quad (34)$$

Here,  $f_{\text{gas}} = M_g/M_v$  is the gas fraction of the halo, which also determines the size of the SGC by the condition of self-gravitating.

- (ii)  $\sigma_s$ , the width of the density distribution, is determined by the cascading of turbulence. Numerical simulations (e.g. Appel et al. 2022) suggested that it can be parameterized as

$$\sigma_s^2 = \ln \left[ 1 + f_s \mathcal{M}^2 \right]. \quad (35)$$

Here  $f_s = b^2\beta_m/(1+\beta_m)$ , with  $b$  accounting for different turbulence modes (1/3 for pure solenoidal mode and 1 for pure compressive mode), and  $\beta_m$  denotes the ratio between thermal and magnetic pressure. The Mach number of the turbulence,  $\mathcal{M}$ , is estimated as

$$\mathcal{M} = v_{\text{rms},3D}/c_s = f_{\text{turb}} \frac{\sqrt{V_v^2 + V_w^2}}{c_s}, \quad (36)$$

where  $c_s \approx 10 \text{ km s}^{-1}$  is the sound speed,  $f_{\text{turb}}$  characterizes the fraction of the kinetic energy initially injected to the turbulent ISM, and  $V_w$  is the speed of the SN wind when it is coupled to the ISM. Since  $f_s$  and  $f_{\text{turb}}$  are degenerate, we absorb  $f_{\text{turb}}$  into  $f_s$ , and take  $f_s = 1$  as the fiducial value, based on calibrations using the observed relations of GC systems (see Appendix B). The fiducial value for the wind speed is set to be  $V_w = 250 \text{ km s}^{-1}$ , consistent with the value adopted in §2.3 for the SN feedback.

- (iii)  $\alpha_s$ , the high-density slope, is found to be 1–2 by numerical simulations (e.g. Appel et al. 2022; Kiihne et al. 2025). We take  $\alpha_s = 1.5$ , which is consistent with the analytical expectation for the pressure-free (free-fall) collapse (Girichidis et al. 2014), and for the weak magnetic field and high compression we assumed in setting  $f_s$  (Collins et al. 2011).

With these choices, the initial (post-shock) mass and density of a sub-cloud can be obtained by sampling the distribution function given by Eqs. (30) and (31), respectively, as described in §4.1. As an analytical estimation, the typical density contrast of the post-shock sub-clouds in the high-density tail of the supersonic turbulence is

$$\rho_{sc}/\rho_0 \sim e^{s_t} \sim e^{\sigma_s^2} \sim 1 + f_s \mathcal{M}^2 \sim \mathcal{M}^2. \quad (37)$$

Using Eqs. (36) and (2) for  $\mathcal{M}$  and  $V_v$ , respectively, the Mach number for a halo with  $M_v$ , at redshift  $z$ , and without the presence of SN-induced turbulence ( $V_w = 0$ ) is

$$\mathcal{M}_1 = \begin{cases} 8.00 M_{v,10}^{1/3} (1+z)^{1/2}, \\ 13.86 M_{v,11.5}^{1/3} (1+z)^{1/2}, \end{cases} \quad (38)$$

where  $c_s = 10 \text{ km s}^{-1}$  is used. At  $z = 9$ ,  $\mathcal{M}$  can be high for relatively low-mass halos due to their high densities, while at  $z = 2$  a high value can be achieved in massive halos. Thus, at any redshift, the post-shock density of SCs,  $\rho_0 \mathcal{M}^2$ , can be orders of magnitude higher than the mean density of the SGC, as long as the driving force of

the turbulence is sufficiently strong. Meanwhile, the SN-induced turbulence has a Mach number

$$\mathcal{M}_2 \equiv V_w/c_s = 25, \quad (39)$$

which is higher than  $\mathcal{M}_1$  over the entire redshift range for all halos below the Milky Way (MW) mass. This suggests that supernovae are always important sources to create dense sub-clouds, except for cluster-size halos ( $M_v \gtrsim 10^{13} M_\odot$ ) expected at low redshift, where  $\mathcal{M}_1$  becomes very large. The situation is similar to the growth of SMBH described in §2.3, where supernovae provide small-scale ‘positive feedback’ to enhance the growth of SMBHs, although their large-scale effect is to eject gas and thus represents a source of negative feedback for star formation.

Using Eq. (8) for  $n_{\text{sgc}}$ , the post-shock density without SN is thus

$$n_{\text{sc}} \sim n_{\text{sgc}} \mathcal{M}_1^2 = f_{\text{str},4} f_{\text{gas},0.04}^{-2} \times \begin{cases} [4.24 \times 10^4 \text{ cm}^{-3}] M_{v,10}^{2/3} (1+z)_{10}^4, \\ [3.20 \times 10^3 \text{ cm}^{-3}] M_{v,11.5}^{2/3} (1+z)_3^4, \end{cases} \quad (40)$$

and the post-shock density induced solely by SN is

$$n_{\text{sc}} \sim n_{\text{sgc}} \mathcal{M}_2^2 = f_{\text{str},4} f_{\text{gas},0.04}^{-2} \times \begin{cases} [1.11 \times 10^5 \text{ cm}^{-3}] (1+z)_{10}^3, \\ [4.13 \times 10^4 \text{ cm}^{-3}] (1+z)_3^3. \end{cases} \quad (41)$$

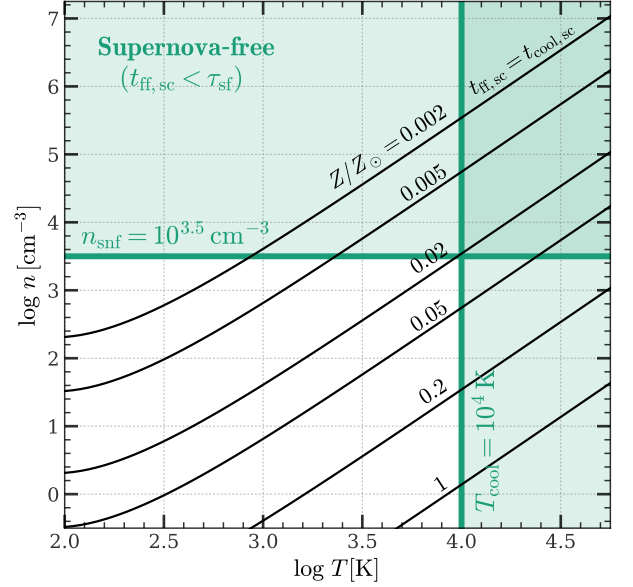
As we will show in §3.5, a sub-cloud with  $n_{\text{sc}} \gtrsim 10^{3.5} \text{ cm}^{-3}$  can remain supernova-free over a free-fall timescale, and may thus be able to form a globular cluster. The estimation in Eqs. (40) and (41) suggests that a gas-rich, dense and turbulent SGC provides the condition to form globular clusters, consistent with the results of FIRE-2 zoom-in simulations (e.g. Ma et al. 2020).

Fig. 4 shows  $p(s)$ , the distribution function of the logarithmic density contrast and its cumulative function for a number of  $\sigma_s$ . In all cases, the low-density, log-normal part ( $s < 2$ ) takes the majority (> 50%) of the probability mass, indicating that stars can form over the entire SGC, albeit with a lower efficiency in a more diffuse medium. This is in contrast to the pure feedback-free model of Dekel et al. (2023), which predicts that star formation in massive halos ( $M_v \approx 10^{10.8} M_\odot$ ) at high- $z$  Universe ( $z \approx 10$ ) is concentrated on dense, supernova-free sub-clouds. The high-density tail of  $p(s)$ , on the other hand, is found to account for about 20% of the probability mass, assuming the typical Mach number at  $z \gtrsim 2$  in Eqs. (38) and (39) (corresponding to  $\sigma \approx 3.5$ –7). As we will show below, sub-clouds in this regime can reach a star formation efficiency of 100%, and thus, contribute a significant fraction of star formation rate and total stellar mass. Recent JWST observations in lensed fields (e.g. Vanzella et al. 2022, 2023; Welch et al. 2023; Lin et al. 2023; Claeysens et al. 2023; Adamo et al. 2024; Messa et al. 2024; Fujimoto et al. 2024; Mowla et al. 2024) appear to support this prediction.

### 3.2 The cooling and fragmentation of sub-clouds

The initial temperature,  $T_{\text{cool}} = 10^4 \text{ K}$ , set by rapid cooling at the formation of sub-clouds, is much higher than that required by star formation. Thus, other cooling channels, such as those given by metal, dust and molecules, determine the subsequent evolution of sub-clouds until the trigger of star formation.

The behavior of how a sub-cloud cools and evolves can be understood by comparing its cooling timescale,  $t_{\text{cool,sc}}$ , and its free-fall timescale,  $t_{\text{ff}}$  (e.g. Fernandez & Bryan 2018; Mandelker et al.



**Figure 5.** The cooling diagram of sub-clouds. **Black** contours show the loci of equaling cooling and free-fall timescales,  $t_{\text{cool,sc}} = t_{\text{ff,sc}}$ , at different metallicity (see §3.2 for details). The **vertical shaded region** indicates the regime above the critical temperature  $T_{\text{cool}} = 10^4 \text{ K}$ , where cooling is effective and fragmentation of SGC is expected to occur to form sub-clouds. The **horizontal shaded region** above the ‘feedback-free’ threshold,  $n_{\text{snf}} = 10^{3.5} \text{ cm}^{-3}$ , indicates the regime where star formation in sub-clouds is free of (internal) supernova feedback. A sub-cloud reaching a density  $n_{\text{sc}} \geq n_{\text{snf}}$  thus hosts a GC (see §3.5 for details).

2018; Dekel et al. 2023). When cooling is effective, i.e. when  $t_{\text{cool,sc}} \lesssim t_{\text{ff,sc}}$ , the heating by gravitational collapse is not able to compensate for the cooling loss, and the growth of small-scale perturbations is no longer limited by gas pressure. Sub-clouds with such initial conditions are thus expected to fragment and form stars. On the other hand, if  $t_{\text{cool,sc}} \gtrsim t_{\text{ff,sc}}$ , a global contraction of the sub-cloud can continue for a longer period without being impeded by fragmentation and star formation. At given  $T$  and  $Z$ , the cooling timescale  $t_{\text{cool,sc}} \propto n_{\text{sc}}^{-1}$  while the free-fall timescale  $t_{\text{ff,sc}} \propto n_{\text{sc}}^{-1/2}$ . Thus, a contracting sub-cloud will eventually enter the regime of effective cooling, and begin to fragment once  $t_{\text{cool,sc}} \sim t_{\text{ff,sc}}$ .

Following Dekel et al. (2023), we use the dominant channel of [CII] 158  $\mu\text{m}$  line cooling to estimate the cooling time scale for gas at  $Z/Z_\odot > 10^{-3}$ . Using results given by Krumholz (2012), we have

$$t_{\text{cool,sc}} \approx 0.87 \text{ Myr } n_{\text{sc},3.5}^{-1} Z_{0.02}^{-1} T_4 \exp\left(\frac{0.009}{T_4}\right) C^{-1}, \quad (42)$$

where  $Z = 0.02 Z_\odot$ ;  $n_{\text{sc}} = 10^{3.5} \text{ cm}^{-3}$ ;  $T = 10^4 \text{ K}$ ;  $T_4$  is a molecular weight  $\mu = 1.2$  is used;  $C = \langle n^2 \rangle / \langle n \rangle^2$  is the clumpiness factor within the sub-cloud. The free-fall timescale depends only on the matter density:

$$t_{\text{ff,sc}} = \left( \frac{3\pi}{32G\rho} \right)^{1/2} = 0.84 \text{ Myr } n_{\text{sc},3.5}^{-1/2}. \quad (43)$$

The threshold density for triggering star formation,  $n_{\text{sf}}$ , can be estimated using  $t_{\text{ff,sc}} \approx t_{\text{cool,sc}}$ , which gives

$$n_{\text{sf}} \approx 3.39 \times 10^3 \text{ cm}^{-3} Z_{0.02}^{-2} T_4^2 C^{-2} = n_{\text{sf},1} C^{-2}. \quad (44)$$

Based on the above arguments, we adopt the following criteria for the fragmentation of sub-clouds. If a sub-cloud has an initial density  $n_{\text{sc}} \geq n_{\text{sf},1}$ , it fragments immediately, followed by star formation in

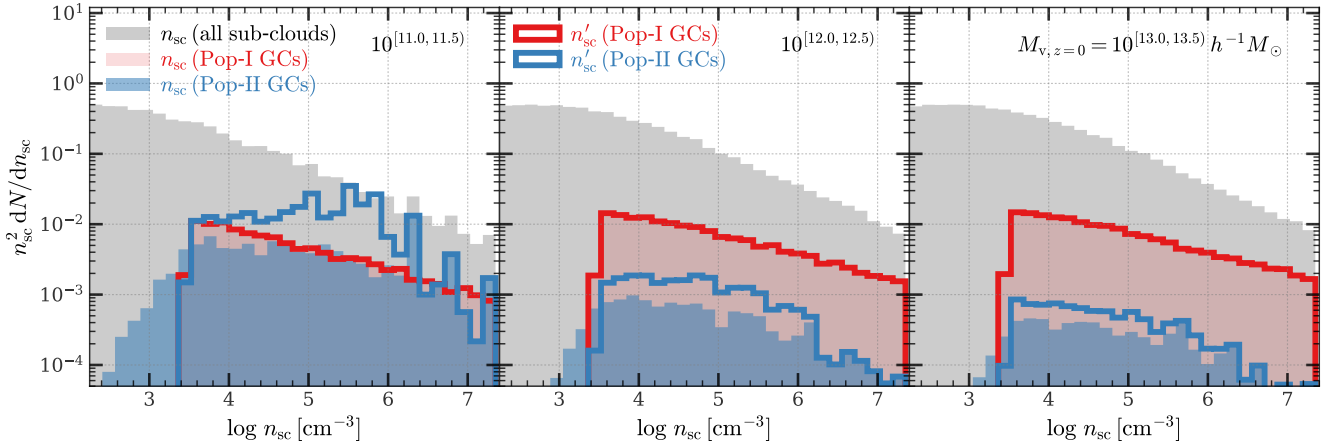


**Figure 6.** Distributions of sub-cloud density. Histograms shown by **shaded areas** and **solid lines** are obtained from  $n_{sc}$ , the density at formation (post-shock), and  $n'_{sc}$ , the density at fragmentation (post-cooling), respectively. In each panel, **grey** histogram shows the result for all sub-clouds, while **red** and **blue** histograms show the results for Pop-I (metal-rich) and Pop-II (metal-poor) GCs, respectively, selected at the birth time (see §4.1 for the selection and classification criteria). Different **panels** show the stacked results for central subhalos with different halo mass at  $z = 0$ . Sub-clouds formed in the main branches of these subhalos are included in the analysis. See §3.2 for a detailed discussion.

individual fragments. On the other hand, if  $n_{sc} < n_{sf,1}$ , the sub-cloud first contracts globally to a density  $n'_{sc}$ , and then fragments to form stars. Due to the uncertainty in the growth of the clumpiness factor  $C$  during the contraction of sub-cloud, we randomly sample  $n'_{sc}$  in the range  $[n_{sc}, n_{sf,1}]$  from a power-law distribution given by

$$\frac{dN_{sc}}{dn'_{sc}} \propto n_{sc}^{\beta_{sc,n}}, \quad (45)$$

where the power-law index is calibrated to be  $\beta_{sc,n} = -2.5$  (see Appendix B).

Fig. 5 shows contours of  $t_{ff,sc} = t_{cool,sc}$ , evaluated using Eqs. (42) and (43) with  $C = 1$ , at different metallicity. The intersection of a contour with the vertical line,  $T = 10^4$  K, gives the star formation threshold density,  $n_{sf,1}$ , as derived in Eq. (44). The strong metallicity dependence of  $n_{sf,1}$  has important implications for the formation of star clusters. At  $z \lesssim 0.02$ ,  $n_{sf,1}$  is above the supernova-free density threshold,  $n_{snf}$ , indicating that a metal-poor sub-cloud, regardless of its initial density, have the possibility to contract to a supernova-free cloud before fragmentation, if it is not destroyed by other sources of feedback (see §3.3 below). Thus, a metal-poor galactic environment provides an additional channel for the formation of GCs, complementary to that via shock compression.

The global collapse of a sub-cloud in the metal-poor condition has been demonstrated by the simulations of [Fernandez & Bryan \(2018\)](#) for individual sub-clouds. They found that, with a moderate UV heating background, a sub-cloud with  $M_{sc} = 10^6 M_\odot$  and  $Z = 0.01 Z_\odot$  can collapse globally to form a dense, fragmented core with a size of  $\approx 5\text{--}10$  pc, while the low-density, smooth envelop does not fragment (see their figure 6). A detailed analysis based on the cooling diagram shows that this delayed fragmentation is due to inefficient cooling of metal-poor gas (see their figures 2 and 7). A similar conclusion can be found in the simulations of [Grudić et al. \(2021\)](#) for individual sub-clouds, who found that the star formation efficiency on sub-cloud scales increases with increasing sub-cloud surface density, and that the fraction of stars formed in bound clusters is higher in their low-metallicity runs.

Grey shades in Fig. 6 show the distributions of sub-cloud density at formation ( $n_{sc}$ ), for all sub-clouds formed in the main branches of central subhalos at  $z = 0$  with different halo masses. Depending on internal properties and environments, sub-clouds can have

different fates: some will be destroyed by external feedback, while others will continue to contract, fragment and form stars at  $n'_{sc}$ . Only the most massive and/or densest sub-clouds can shield themselves from feedback and form sufficient amounts of stars to qualify as (the progenitors of) globular clusters. These will be discussed thoroughly in §§3.3, 3.4 and 3.5, and be synthesized into a coherent model in §4.1. Briefly, the aforementioned conditions, together with supersonic turbulence and metal-poor environment, give rise to two distinct formation channels that lead to two populations of GCs: Pop-I (the metal-rich population) and Pop-II (the metal-poor population).

The red and blue shades in Fig. 6 show the distributions of gas density at formation for sub-clouds that will eventually evolve into Pop-I and Pop-II GCs, respectively, while the solid lines show the distributions of the gas density at fragmentation for the two populations. At  $10^{3.5} \text{ cm}^{-3}$ , the lower limit for a sub-cloud to qualify as (the progenitor of) a globular cluster, only  $< 10\%$  of sub-clouds are massive enough to form globular clusters, mainly due to the bottom-heavy nature of the sub-cloud mass function (Eq. 30). A significant fraction of metal-poor sub-clouds with low initial density can contract to higher density to reach the condition for globular cluster formation, as clearly suggested by comparing the blue histograms for  $n_{sc}$  and  $n'_{sc}$ . The effects of sub-cloud contraction appear to be more significant for low-mass halos, as their metallicity is lower. In contrast, metal-rich sub-clouds hosting globular clusters can fragment immediately after formation. The difference in cooling and fragmentation between the two populations of sub-clouds turns out to be the key to understanding the two channels of GC formation and the observed bimodality in the GC population, as to be discussed in §3.5.

### 3.3 Destruction of sub-clouds by external feedback

Once formed, sub-clouds are subject to various external feedback effects produced by other stars in the galaxy. One of the main feedback sources is the shock wave associated with the energy injection from stellar evolution and SNe, which we collectively refer to as ‘wind feedback’. Depending on the state of the gaseous structure that is affected by the wind feedback, the effect of such feedback can be either negative or positive. For dense sub-clouds where cooling is effective and an isothermal state can be maintained, shocks are to



compress the gas. On the other hand, for the diffuse component or low-density sub-clouds where gas cannot cool effectively, shocks may disperse gas and disrupt sub-clouds (see e.g. §8.3 of Mo et al. 2010; Hopkins et al. 2012; Rosen 2022). The effect of the SN feedback is also scale-dependent. At the galactic scale, its effect is to reduce the amount of star-forming gas and prevent star formation, as modeled by the  $F_{\text{sn}}$  factor in §2.3. Consequently, the total number of sub-clouds survived is also reduced. In terms of individual sub-clouds, the high-density ones are compressed to higher density by shocks, and such positive feedback is already described in §3.1. Here we focus on the negative side of the feedback.

As suggested by Dekel et al. (2023), wind feedback can ablate or destroy sub-clouds. Following their arguments, we use  $t_{\text{crush,sc}}$ , the timescale for the shock to crush a sub-cloud, to estimate the time needed for the shock to destroy the sub-cloud. This timescale is given by Klein et al. (1994):

$$t_{\text{crush,sc}} = 2 \frac{R_{\text{sc}} \rho_{\text{sc}}^{1/2}}{V_w \rho_w^{1/2}}. \quad (46)$$

Here,  $V_w$  and  $\rho_w$  are, respectively, the wind velocity and density when it hits the sub-cloud. These two quantities are related by

$$\rho_w = \frac{\Phi \eta_w}{4\pi R_{\text{sgc}}^2 V_w}, \quad (47)$$

where  $\Phi$  is the star formation rate of the galaxy, and  $\eta_w$  is the mass loss fraction of stars. Using the Starburst99 library (Leitherer et al. 1999), and assuming a wind-lasting time of  $\approx 10$  Myr and a specific loss rate of  $10^{-8} \text{ yr}^{-1}$ , Dekel et al. (2023) estimated that  $\eta_w \approx 0.1$ . The wind velocity is estimated to be  $10^{3.5} \text{ km s}^{-1}$ , which is the typical value of an SN-driven wind before it is coupled with the ISM. The radius of the SGC, as discussed in §2.2, is  $R_{\text{sgc}} = f_{\text{gas}} R_v$ . For the sub-cloud to survive the wind disruption and proceed to the regime of collapse and fragmentation, the cooling timescale in the turbulence mixing layer around the sub-cloud has to be shorter than the crushing timescale:  $t_{\text{cool,sc}} < t_{\text{crush,sc}}$ . Substituting Eq. (42) and (46) into this condition, we obtain the density threshold for a sub-cloud to survive the wind feedback:

$$n_{\text{shield,w}} = 94.71 \text{ cm}^{-3} (\eta_{w,0.1} \Phi_1)^{3/7} \times (Z_{0.02} R_{v,25} f_{\text{gas},0.04})^{-6/7} M_{\text{sc},6}^{-2/7}, \quad (48)$$

where  $\eta_w = 0.1 \eta_{w,0.1}$ ,  $R_v = 25 \text{ kpc } R_{v,25}$  and  $\Phi = 1 \text{ M}_{\odot}/\text{yr } \Phi_1$ . Using the equation of  $\dot{M}_v$  in Eq. (6), assuming a star formation efficiency  $\epsilon_v = M_*/(f_{\text{B}} M_v) = 0.1$ , a mass returning fraction given by Eq. (17), the mean  $Z(M_v, z)$  relation in Eq. (28), and  $R_v$  in Eq. (4), the shielding density can be approximated as

$$n_{\text{shield,w}} = \eta_{w,0.1}^{3/7} (f_{\text{gas},0.04})^{-6/7} M_{\text{sc},6}^{-2/7} \epsilon_{v,0.1}^{-0.086} \times \begin{cases} [233.96 \text{ cm}^{-3}] M_{v,10}^{-0.31} (1+z)_{10}^{2.4}, \\ [4.49 \text{ cm}^{-3}] M_{v,11.5}^{-0.31} (1+z)_3^{2.4}. \end{cases} \quad (49)$$

This depends weakly on halo mass, but as fast as  $n_{\text{sgc}}$  on redshift (see Eq. 8). At  $z = 2$  and  $z = 9$ , it is much smaller than  $n_{\text{sgc}}$  and thus than the post-shock tail of  $n_{\text{sc}}$  (see Eqs. 40 and 41), indicating that only low-density, low-mass sub-clouds are destroyed.

Another source of feedback is the UV radiation of massive stars, which can heat and unbound sub-clouds. The shielding length of an SC is obtained by equaling the HII recombination rate and the photon flux (Dekel et al. 2023), as

$$\Delta R = \frac{f_{\text{OB}} \nu_{\text{ion}} \tau_{\text{OB}} \Phi}{4\pi R_{\text{sgc}}^2 n_{\text{sc}}^2 \alpha_{\text{rec}}}, \quad (50)$$

where  $f_{\text{OB}} = 0.01 \text{ M}_{\odot}^{-1}$  is the number of massive (O/B) stars per solar mass of formed stars,  $\tau_{\text{OB}} = 10 \text{ Myr}$  is their lifetime,  $\nu_{\text{ion}} = 10^{49} \text{ s}^{-1}$  is the UV photon rate per massive star, and  $\alpha_{\text{rec}} = 4 \times 10^{-13} \text{ cm}^3 \text{ s}^{-1}$  is the recombination rate per unit density. For a sub-cloud to survive the UV radiation, its size,  $R_{\text{sc}}$ , has to be larger than the shielding length,  $\Delta R$ , namely  $R_{\text{sc}} > \Delta R$ . This gives the density threshold for a sub-cloud to survive the UV radiation:

$$n_{\text{shield,r}} = 8.27 \text{ cm}^{-3} (\tau_{10} \Phi_1)^{3/5} \times (R_{v,25} f_{\text{gas},0.04})^{-6/5} M_{\text{sc},6}^{-1/5}, \quad (51)$$

where  $\tau_{\text{OB}} = 10 \text{ Myr } \tau_{10}$ . This value of  $n_{\text{shield,r}}$  is usually smaller than  $n_{\text{shield,w}}$ , meaning that UV radiation is not a main source to disperse sub-clouds.

For both the wind feedback and radiation feedback, the  $\Phi/R_{\text{sgc}}^2$ -dependence in the shielding density suggests that the survival of sub-clouds is preferred in low-mass, gas-rich halos, because

$$\frac{\Phi}{R_{\text{sgc}}^2} \sim \Sigma_{\text{SFR}} \sim \Sigma_{\text{gas}}^{\gamma} \sim \left( \frac{M_{\text{sgc}}}{R_{\text{sgc}}^2} \right)^{\gamma} \sim f_{\text{gas}}^{-\gamma} M_v^{\gamma/3}, \quad (52)$$

where  $\gamma \approx 1.5$  is the Kennicutt-Schmidt index. The negative dependence on  $M_{\text{sc}}$  and  $Z$  indicates that sub-clouds with larger mass and higher metallicity have a better chance of surviving against the feedback effects. The effects of the  $Z$ -dependence and the  $\Sigma_{\text{SFR}}$ -dependence cancel each other, weakening the dependence on  $M_v$ , as shown by Eq. (49).

The effect of stellar feedback on star formation has been confirmed by Appel et al. (2022) using MHD simulations, where the inclusion of stellar feedback (outflow and heating) significantly increases the amount of diffuse gas below the mean density, reduces the rate of mass transfer from the log-normal peak to the power-law tail, and thus reduces SFR.

Other sources of feedback external to sub-clouds include the cosmic UV background, which is anticipated to suppress star formation in halos with mass below  $\approx 10^9 \text{ M}_{\odot}$  after the epoch of reionization, and the feedback from accreting SMBHs. As their effects have already been included by the two-phase model in the star formation law of the entire galaxy (§2.3) to set the normalization of the total amount of star formation, we do not include them in the sub-cloud model.

For SNe inside a sub-cloud, the timescale for them to disperse the sub-cloud is too short for cooling to take place. This sets a time window for star formation and a key criterion for the formation of GCs, as we will describe in §3.4 and §3.5, respectively. The combination of these positive and negative effects will become clearer when we join the pieces to construct a complete model in §4.1. The operation of these processes is also demonstrated by high-resolution zoom-in simulations. For example, as shown in figure 3 of Ma et al. (2020) using the FIRE-2 zoom-in simulations, as soon as SNe are triggered by the formation of a massive star cluster, most of the surrounding gas is dispersed, leaving a number of high-density clumps produced by the compression of wind feedback.

### 3.4 Star formation in sub-clouds

Once a sub-cloud survives the external feedback and contracts to a density so that  $t_{\text{cool,sc}} \sim t_{\text{ff,sc}}$ , it is expected to fragment and form stars. The newly formed stars then produce internal feedback, which suppresses star formation within the sub-cloud. As estimated by Paper-1, supernova feedback can affect a self-gravitating, gaseous system with an escaping velocity  $V_{\text{esc}} \lesssim 200 \text{ km s}^{-1}$  (see also e.g. Hopkins et al. 2023). This escaping velocity is much higher than

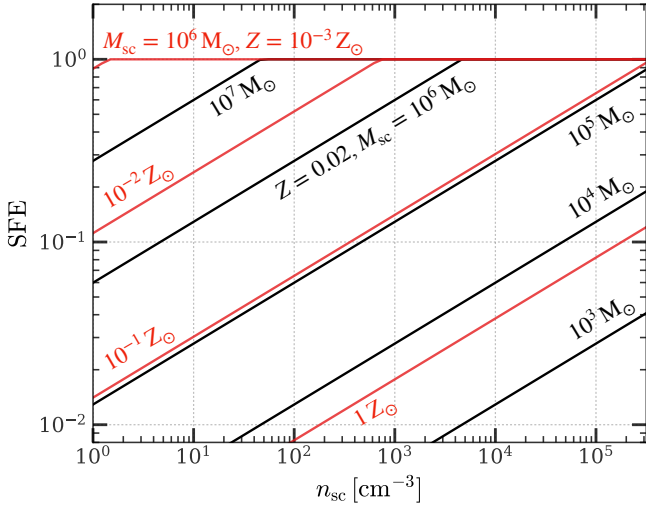


**Figure 7.** Star formation efficiency (SFE) of sub-clouds as a function of their density ( $n_{\text{sc}}$ ), adopting wind feedback and  $\epsilon_{\text{w,max}} = 1$ . **Black** lines show the cases with different sub-cloud mass ( $M_{\text{sc}}$ ) and a fixed metallicity,  $Z = 0.02 Z_{\odot}$ . **Red** lines show the cases with different metallicity and a fixed sub-cloud mass,  $M_{\text{sc}} = 10^6 M_{\odot}$ . See §3.4 for details.

that of a sub-cloud, implying that a sub-cloud will be dispersed as soon as the formation of its first generation of stars. Thus, the delay time of supernova feedback, namely the lifetime of massive stars, sets the time window for star formation in sub-clouds. Based on the Starburst99 library (Leitherer et al. 1999) for individual starbursts, Dekel et al. (2023, see their figure 1) found that this time window is about  $\tau_{\text{sf}} \approx 1$  Myr, quite independent of the metallicity. Within this time window, star formation in sub-clouds is regulated by other channels of stellar feedback, as we discuss below.

Stellar winds generated by massive stars can affect the surrounding gas in the sub-cloud and reduce the subsequent star formation. Here, we adopt a metallicity-dependent wind energy deposition,

$$E_{\text{w}} = e_{\text{w}} \eta_{\text{w}} \tau_{\text{sf}} \left( \frac{Z}{Z_{\odot}} \right)^{0.9} M_{\text{cls}}. \quad (53)$$

Here,  $M_{\text{cls}}$  is the stellar mass of the star cluster formed within the sub-cloud; the normalization  $e_{\text{w}} \approx 10^{40} \text{ erg s}^{-1} (10^6 M_{\odot})^{-1}$  is computed by Dekel et al. (2023) based on the same library in the estimation of  $\tau_{\text{sf}}$ ;  $\eta_{\text{w}} \approx 0.1$  is the wind coupling factor (Gupta et al. 2016). The metallicity dependence comes mainly from the metallicity-dependent threshold for Wolf-Rayet stars that dominate the wind power, while the power-law index 0.9 was suggested by Hirschi (2007). For the wind to be effective in destroying the sub-cloud,  $E_{\text{w}}$  must be comparable to the binding energy of the sub-cloud,  $E_{\text{b}} \approx (1/2) G M_{\text{sc}}^2 / R_{\text{sc}}$ . Equating these two energies leads to a star formation efficiency,  $\epsilon_{\text{w}} \equiv M_{\text{cls}} / M_{\text{sc}}$ , that determines the fraction of the gas in the sub-cloud to be converted into stars under the effect of stellar winds:

$$\begin{aligned} \epsilon_{\text{w}} &= \frac{G M_{\text{sc}}}{2 R_{\text{sc}} (Z / Z_{\odot})^{0.9} \tau_{\text{sf}} \eta_{\text{w}} e_{\text{w}}} \\ &= 3.81 \frac{M_{\text{sc},6}}{R_{\text{sc},12} Z_{0.02}^{0.9} \tau_{\text{sf},1} \eta_{\text{w},0.1}} \\ &= \epsilon_{\text{w,max}} M_{\text{sc},6}^{-1} R_{\text{sc},12}^{-0.9} Z_{0.02}^{-0.9}, \end{aligned} \quad (54)$$

where  $M_{\text{sc}} = 10^6 M_{\odot} M_{\text{sc},6}$ ,  $R_{\text{sc}} = 12 \text{ pc } R_{\text{sc},12}$ ,  $\tau_{\text{sf}} = 1 \text{ Myr } \tau_{\text{sf},1}$ ,  $\eta_{\text{w}} = 0.1 \eta_{\text{w},0.1}$ , and  $\epsilon_{\text{w,max}} \equiv 3.81 / (\tau_{\text{sf},1} \eta_{\text{w},0.1}) \sim 1$  is the maximum star formation efficiency. Fig. 7 shows the star formation efficiency of sub-clouds as a function of their density, regulated by

the wind feedback. At  $Z / Z_{\odot} \approx 0.02$ , the star formation efficiency reaches unity for a sub-cloud with mass of  $10^6 M_{\odot}$  and a size of 12 pc, indicating that a low-metallicity sub-cloud free of internal supernova feedback is also free of internal wind feedback. A reduction of density or mass, or an increase of metallicity, decreases the resistance of sub-cloud to wind feedback and thus lowers the star formation efficiency. Assuming that  $\tau_{\text{sf}}$  and  $\eta_{\text{w}}$  are independent of  $M_{\text{sc}}$ ,  $R_{\text{sc}}$  and  $Z$ , the star formation efficiency scales as

$$\epsilon_{\text{w}} \propto M_{\text{sc}} R_{\text{sc}}^{-1} Z^{-0.9} \propto M_{\text{sc}}^{2/3} Z^{-0.9}. \quad (55)$$

Photo-ionization from stellar radiation also imparts momentum/pressure on the gas within a sub-cloud, which can also disperse the gas and reduce the star formation efficiency (e.g. Li et al. 2020). Following the argument of e.g. Fall et al. (2010), the specific momentum injection rate is

$$\dot{p}_{\text{r}} = \frac{1}{c} \left\langle \frac{L_{*}}{M_{*}} \right\rangle \beta_{\text{boost}}, \quad (56)$$

where  $\langle L_{*} / M_{*} \rangle \approx 10^3 L_{\odot} / M_{\odot}$ , corresponding to the peak emission of a blackbody radiation with  $T \approx 40,000 \text{ K}$  for OB stars. The boosting factor  $\beta_{\text{boost}}$  takes into account the effect of multiple scattering. Following Marinacci et al. (2019), we set  $\beta_{\text{boost}} = 1 + \kappa_{\text{IR}} \Sigma_{\text{sc}}$ , where  $\Sigma_{\text{sc}} = M_{\text{sc}} / (\pi R_{\text{sc}}^2)$  is the surface density of the sub-cloud and  $\kappa_{\text{IR}} = 10 (Z / Z_{\odot}) \text{ cm}^2 \text{ g}^{-1}$  is the infrared opacity. Equating the total momentum injection rate,  $\dot{p}_{\text{r}} M_{\text{cls}}$ , to the gravity,  $G M_{\text{sc}}^2 / R_{\text{sc}}^2$ , we obtain the star formation efficiency  $\epsilon_{\text{r}}$  for a radiation-regulated sub-cloud, as

$$\epsilon_{\text{r}} = \frac{\pi G}{\frac{1}{c} \left\langle \frac{L_{*}}{M_{*}} \right\rangle (\Sigma_{\text{sc}}^{-1} + \kappa_{\text{IR}})} = 2.16 \frac{\Sigma_{\text{sc},3.5}}{1 + 0.13 \Sigma_{\text{sc},3.5} Z_{0.02}}. \quad (57)$$

At  $Z / Z_{\odot} \approx 0.02$ ,  $\epsilon_{\text{r}}$  is proportional to  $\Sigma_{\text{sc},3.5}$  and thus we have

$$\epsilon_{\text{r}} \propto \Sigma_{\text{sc}} \propto M_{\text{sc}}^{1/3}. \quad (58)$$

This efficiency reaches unity at  $\Sigma_{\text{sc}} \approx 10^{3.2} M_{\odot} \text{ pc}^{-2}$ , comparable to the condition for sub-clouds with  $\epsilon_{\text{w}} \approx 1$ . At high metallicity, the momentum injection from multiple scattering can effectively reduce the star formation. A more general form of Eq. (55) was originally proposed by Fall et al. (2010), and subsequently confirmed in hydrodynamical simulations and observations. In particular, Grudić et al. (2018) showed that the formula is accurate for a mixture of feedback processes, both momentum-driven and energy-driven, including radiation pressure, photo-ionization, stellar winds, etc. The formula is also consistent with various observations of proto-clusters/sub-clouds in the MW and the Large Magellanic Cloud (LMC; Mok et al. 2021).

Based on the above discussion, we can parameterize the sub-cloud-scale star formation efficiency as

$$\epsilon_{\text{sf}} \equiv M_{\text{cls}} / M_{\text{sc}} = \epsilon_{\text{sf,max}} M_{\text{sc},6}^{\beta_{\text{sf}}} Z_{0.02}^{\gamma_{\text{sf}}}, \quad (59)$$

where  $\epsilon_{\text{sf,max}} \approx 1$  is the maximum star formation efficiency, which is reached at  $M_{\text{sc}} \approx 10^6 M_{\odot}$  and  $Z \approx 0.02 Z_{\odot}$ . The values of  $\gamma_{\text{sf}}$  and  $\beta_{\text{sf}}$  depend on the dominant channel of stellar feedback. For example,  $(\beta_{\text{sf}}, \gamma_{\text{sf}}) = (2/3, -0.9)$  in the wind-regulated regime, while  $(\beta_{\text{sf}}, \gamma_{\text{sf}}) = (1/3, 0)$  in the radiation-regulated, metal-poor regime. If these two channels operate in multiplication,  $(\beta_{\text{sf}}, \gamma_{\text{sf}}) = (2/3 + 1/3, -0.9)$ .

By definition, the size of a sub-cloud with density  $n_{\text{sc}}$  is

$$R_{\text{sc}} = \left[ \frac{M_{\text{sc}}}{(4\pi/3) \mu m_{\text{p}} n_{\text{sc}}} \right]^{1/3} = 13.65 \text{ pc } M_{\text{sc},6}^{1/3} n_{\text{sc},3.5}^{-1/3}, \quad (60)$$

where the default values of  $M_{\text{sc}}$  and  $n_{\text{sc}}$  are set by the Jeans mass

(Eq. 29) and supernova-free density, respectively. Thus, the typical spatial extent of GC-forming sub-clouds is 10 pc.

The half-stellar-mass radius of a star cluster,  $R_{\text{cls}}$ , is determined by  $R_{\text{sc}}$ , the size of its parent sub-cloud and we model it as

$$R_{\text{cls}} = f_{\text{r,cls}} R_{\text{sc}}, \quad (61)$$

where  $f_{\text{r,cls}} \lesssim 1$  depends on the density profile of the cluster. For an isothermal sub-cloud,  $f_{\text{r,cls}} = 1/2$ , which we find to be able to reproduce observed sizes of young massive star clusters and globular clusters (see §4.3 below). Such a similarity between cluster size and sub-cloud size is expected if star formation in sub-cloud follows a scale-free fragmentation process in which the free-fall timescale is the same throughout the sub-cloud.

Combining the above equations for sub-cloud size-mass relation, star formation efficiency, and the definition of star-cluster size, we obtain the size-mass relation of star clusters at birth:

$$R_{\text{cls}} = 6.83 \text{ pc } n_{\text{sc},3.5}^{-1/3} \left( \frac{M_{\text{cls},6}}{\epsilon_{\text{sf,max}} Z_{0.02}^{\gamma_{\text{sf}}}} \right)^{\frac{1}{3(\beta_{\text{sf}}+1)}}$$

$$= 6.83 \text{ pc } n_{\text{sc},3.5}^{-1/3} \begin{cases} M_{\text{cls},6}^{1/5} Z_{0.02}^{0.18} & (\text{wind}), \\ M_{\text{cls},6}^{1/4} & (\text{radiative}), \\ M_{\text{cls},6}^{1/6} Z_{0.02}^{0.18} & (\text{wind} + \text{radiative}), \end{cases} \quad (62)$$

where we have defined  $M_{\text{cls}} = 10^6 M_{\odot} M_{\text{cls},6}$ . In both cases, star clusters have roughly constant size, as the dependence on stellar mass and metallicity is weak. This is indeed seen in observations, where star clusters spanning orders of magnitude in masses have a narrow size range of 1–10 pc (e.g. Krumholz et al. 2019; Brown & Gnedin 2021).

### 3.5 The fate of sub-clouds and the two channels of globular cluster formation

For a sub-cloud ready to fragment, a combination of the free-fall time scale,  $t_{\text{ff,sc}}$ , and the star formation time window set by supernova feedback,  $\tau_{\text{sf}}$ , leads to an interesting consequence. If the density of the sub-cloud is  $n_{\text{sc}} \gtrsim 10^{3.5} \text{ cm}^{-3}$ , the free-fall timescale (Eq. 43) will be so short that  $t_{\text{ff,sc}} \lesssim \tau_{\text{sf}}$ . Because  $t_{\text{ff,sc}}$  sets the timescale for a sub-cloud to fragment, the sub-cloud with such high density is expected to be free of supernova feedback. Meanwhile, as suggested by Eqs. (54) and (57), feedback from stellar wind and radiation within such a sub-cloud is ineffective, leading to a star formation efficiency of about unity. Thus, according to the size-mass relation of sub-clouds (Eq. 60), a sub-cloud with gas mass  $\sim 10^6 M_{\odot}$  and size  $\sim 10$  pc converts nearly all its gas into stars, producing a massive star cluster with stellar mass  $\sim 10^6 M_{\odot}$  and size  $\sim 10$  pc. Such a star cluster falls into the mass and size range of globular clusters, and can thus be viewed as the progenitor of a globular cluster. In the remainder of this paper, we will refer to the density,  $n_{\text{snf}} = 10^{3.5} \text{ cm}^{-3}$  as the ‘supernova-free’ density threshold, and use it as a condition for the formation of globular clusters.

The star formation threshold density  $n_{\text{sf},1}$  obtained in Eq. (44) is sensitive to metallicity. In the high-redshift Universe where pristine inflow dominates the gas accretion, the metallicity of sub-clouds can be as low as  $Z \approx 0.02 Z_{\odot}$  so that the density at the triggering of fragmentation can reach  $n_{\text{snf}}$ . Thus, the low-metallicity environment naturally gives rise to the formation of globular clusters, regardless of the initial density produced by shocks. On the other hand, for galactic environments where gas is already enriched, sub-clouds with low initial densities can fragment before they reach  $n_{\text{snf}}$ . This will lead to the formation of star clusters under the influence of supernova

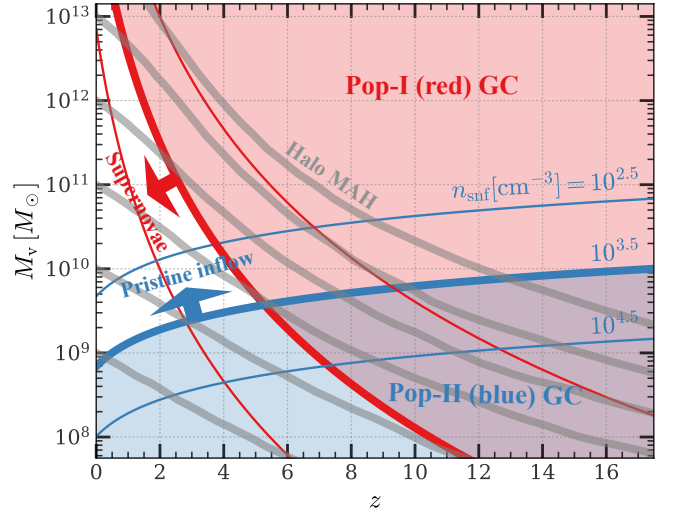


**Figure 8.** The criteria for the formation of Pop-I and Pop-II GCs. **Red and blue shaded areas** indicate the halo mass and redshift where Pop-I and Pop-II GCs can actively form, according to Eqs. (63) and (65), respectively, assuming a supernova-free density threshold  $n_{\text{snf}} = 10^{3.5} \text{ cm}^{-3}$ . Other red and blue curves are the criteria boundaries with alternative choices of  $n_{\text{snf}}$ . In the presence of supernovae and/or metal-poor inflow, the criteria for GC formation can be further relaxed, as indicated by the red and blue arrows. **Gray curves** are median mass assembly histories of halos with different masses at  $z = 0$ , generated using DIFFMAH (Hearin et al. 2021). Note that this figure only shows the environment expected for active GC formation. The random sampling of halo assembly history, sub-cloud density and metallicity can lead to the formation of GCs in unusual environments. See §3.5 for the details of this figure.

feedback, making them less dense, less massive, and more fragile to the tidal field of the host galaxy. Such a star cluster is expected to become an open cluster or to disperse and join the diffuse stellar component. In metal-enriched galaxies, therefore, a globular cluster can form only if the initial density of the parent sub-cloud is  $\gtrsim n_{\text{snf}}$ .

The above discussion leads to two channels of globular cluster formation, depending on the order of three densities: the star formation threshold ( $n_{\text{sf},1}$ ); the supernova-free density ( $n_{\text{snf}}$ ); and the initial density of the sub-cloud ( $n_{\text{sc}}$ ). We thus define two types of globular clusters as follows:

- **Pop-I GC** which forms in a sub-cloud with  $n_{\text{sc}} \gtrsim n_{\text{snf}} > n_{\text{sf},1}$ . A globular cluster of this type relies on compression by supersonic shocks for its progenitor sub-cloud to reach the supernova-free threshold and to fragment.
- **Pop-II GC** which forms in a sub-cloud with  $n_{\text{sf},1} \gtrsim n_{\text{snf}}$ . A globular cluster of this type forms by contracting towards the star formation threshold that is above the feedback-free threshold. Shock compression can help to set a high initial density, but is not necessary. Due to the uncertainty in the growth of the clumpiness factor as described around Eq. (45), a sub-cloud with  $n_{\text{sf},1} \gtrsim n_{\text{snf}}$  may fragment at a density  $n'_{\text{sc}}$  below  $n_{\text{snf}}$ , and thus fail to form a Pop-II GC.

Using Eq. (44) for  $n_{\text{sf},1}$ , the critical density  $n_{\text{sf},1} = n_{\text{snf}}$  that separates the two types of GCs immediately yields a critical gas-phase metallicity,  $Z_{\text{crit}} = 10^{-1.68} Z_{\odot}$ . Our definition of GCs resembles the definition of Pop-I and Pop-II stars, in the sense that Pop-I GCs are metal-rich and Pop-II GCs are metal-poor. Observationally, Pop-I GCs appear red in color, while Pop-II GCs appear blue. Other phenomenological classifications of GCs, such as those based on in- and ex-situ origins, can be derived by integrating the star formation history and merger history of a given system (galaxy/halo). Our

classification of GCs is based on the properties of sub-clouds prior to the star formation. This should not be confused with the Type-I/II GCs classified by the observed stellar populations (e.g. [Milone et al. 2017](#); [Simioni et al. 2020](#)) that reflect the star formation and enrichment history of a GC (see §4 of [Milone & Marino 2022](#), for a review).

To gain some intuition on the condition of globular cluster formation, here we provide a simple analytical estimation. In the absence of ‘positive feedback’ from supernovae, the post-shock density of sub-clouds at the high-density tail is given by Eq. (40), and the Pop-I GC formation criterion,  $n_{\text{sc}} \geq n_{\text{snf}}$ , becomes

$$M_{v,11.5}^{2/3} (1+z)^4 f_{\text{gas},0.04}^{-2} f_{\text{str},4} \geq 0.99 n_{\text{snf},3.5}, \quad (63)$$

where  $n_{\text{snf}} = 10^{3.5} \text{ cm}^{-3} n_{\text{snf},3.5}$ . If supernovae dominate the generation of turbulence, the condition can be obtained by using Eq. (41) as

$$(1+z)^3 f_{\text{str},4} f_{\text{gas},0.04}^{-2} \geq 2.07 n_{\text{snf},3.5}. \quad (64)$$

Thus, supernovae can effectively enhance the formation of Pop-I GCs in halos of any mass over a wide range of redshift. At  $z \lesssim 1$ , the cold stream disappears ( $f_{\text{str}} \approx 1$ ) in most halos and supernova-driven globular cluster formation ceases. On the other hand, using the mean  $Z(M_v, z)$  relation in Eq. (28) and the metallicity-dependent star formation threshold in Eq. (44), the Pop-II GC formation criterion  $n_{\text{sf},1} \geq n_{\text{snf}}$  becomes

$$M_{v,10}^{-1.2} (1+z)^{1.1} \epsilon_{v,0.1}^{-1.2} T_4^2 \geq 1.96 n_{\text{snf},3.5}. \quad (65)$$

In the presence of metal-poor inflows, such as that from cold streams and mergers with low-mass galaxies, the above criterion can be further relaxed (see §4.5).

Fig. 8 shows the conditions for the formation of Pop-I and Pop-II GCs in the  $(z, M_v)$  plane, where fiducial values,  $n_{\text{snf}} = 10^{3.5} \text{ cm}^{-3}$ ,  $\epsilon_v = 0.1$ ,  $f_{\text{gas}} = 0.04$ ,  $f_{\text{str}} = 4$  and  $T = 10^4 \text{ K}$  are used. Both conditions have a positive dependence on redshift and thus favor globular cluster formation in high-redshift halos. However, at a given redshift, they have opposite dependence on halo mass: the Pop-I GCs preferentially form in high-mass halos owing to the high Mach number (strong turbulence), while Pop-II GCs preferentially form in low-mass halos owing to the low metallicity (slow cooling and delayed fragmentation). At  $z \approx 5$ , roughly the peak redshift for the formation of dynamically hot systems (see e.g. figure 12 of [Paper-I](#)), the boundaries of two criteria start to diverge, leaving halos of intermediate mass less efficient in forming GCs. This divergence has direct implications for the GC frequency expected in halos of different masses, as we will discuss in §4.4 and Fig. 12. At  $z \approx 0$ , the low density of the Universe, the enrichment of the environment (galaxy), and the disappearance of cold stream prevent the formation of GCs in most galaxies. This leaves supernova compression and/or galaxy-galaxy merger as the open channel for GC formation.

### 3.6 Dynamical evolution

After formation, dynamical evolution of a star cluster changes its structure, causes continuous mass loss and may eventually disrupt it. Sources that drive the dynamical evolution include two-body relaxation, tidal stripping, and tidal shocks, all of which may depend on the tidal environment and the internal composition and structure of the star cluster. As most GCs are born early, the long time available for dynamical effects to operate can significantly change the number of GCs survived today. For example, [Harris et al. \(2015\)](#) used the observed constancy of GCS mass-halo mass ratio to speculate that

only 1/3-1/5 proto-GCs can survive to the present day. [Choksi & Gnedin \(2019\)](#) modeled the evolution of GCs within external, Milky Way-like tidal field by adopting a disruption timescale of 5 Gyr for clusters with  $M_{\text{cls}} = 2 \times 10^5 M_\odot$ . Consequently, most of such GCs born at  $z \gtrsim 2$  are disrupted. [Chen & Gnedin \(2022\)](#) reported a more detailed modeling of the disruption timescale by tracing tidal fields in a hydrodynamical simulation around individual GCs sampled using a semi-analytical method. Their results suggested that  $\approx 90\%$  of the GCs are disrupted, with significant dependence on their ages and distances to the galactic center (see their figure 13). [Rodríguez et al. \(2023\)](#) performed a more detailed modeling, based on the bulk properties of GMCs resolved by the FIRE-2 simulation of a Milky Way-mass galaxy, a semi-analytical cluster sampler calibrated by simulations of individual GMCs ([Grudić et al. 2021, 2023](#)), and a star-by-star cluster evolution code with assumptions on the cluster structure and tidal field. Their results highlight the complex interplay between the internal stellar population, metallicity and structure of the star cluster, and the varying tidal environment of the host galaxy.

Due to the large sample and dynamic range that we aim to cover, the spatially resolved tidal environment is not available for individual star clusters. Following [Chen & Gnedin \(2023\)](#) and [Chen & Gnedin \(2024\)](#), we adopt a semi-analytical approach, which was originally introduced by [Fall & Zhang \(2001\)](#), extended by [McLaughlin & Fall \(2008\)](#), and calibrated by the high-resolution N-body simulations of [Gieles & Gnedin \(2023\)](#), with modifications according to the SGC properties from our model. For a star cluster with mass  $M_{\text{cls}}(t)$  moving in an orbit with radius  $R_{\text{orb}}(t)$  and  $V_{\text{orb}}(t)$  around the host galaxy, the total mass loss rate can be modeled as

$$\frac{dm(t)}{dt} = -\frac{\nu_0 \Omega_{\text{tid}}(t)}{250} \left[ \frac{M_{\text{cls}}(t_0)}{2 \times 10^5 M_\odot} \right]^{\alpha_{\text{tid}}} m^{\beta_{\text{tid}}}(t). \quad (66)$$

where  $m(t) \equiv M_{\text{cls}}(t)/M_{\text{cls}}(t_0)$  is the scaled mass and  $t_0$  is the birth time of the cluster,  $\nu_0 \sim 1$  is a free parameter that needs to be calibrated by observations due to the unresolved tidal environments in the simulation, such as those producing tidal shocks. We choose  $\nu_0 = 0.6$  as the fiducial value (see Appendix B for the calibration). We set  $\alpha_{\text{tid}} = -2/3$  and  $\beta_{\text{tid}} = -1/3$  using calibrations by the N-body simulation of [Gieles & Gnedin \(2023\)](#), which also takes into account the effects of stellar black holes. Since their calibrations assume a static potential and may thus miss potential non-linear correlations between the two-body relaxation and tidal disruption, we modify their formulation of tidal frequency,  $\Omega_{\text{tid}}$ , to be time-dependent, as

$$\Omega_{\text{tid}}(t) = \frac{V_{\text{orb}}(t)}{R_{\text{orb}}(t)} = \frac{V_v(t)}{u_r f_{\text{gas}} R_v(t)}, \quad (67)$$

where all the normalization constants have been absorbed into  $\nu_0$ , and  $u_r \sim U[0.0, 1]$  is a uniformly distributed random number describing the distribution of the effective orbital radius of the star clusters within the host galaxy. The above formulation relies on the following facts. Firstly, the SGC is self-gravitating, so that  $V_v$  and  $f_{\text{gas}} R_v$  give its typical circular velocity and radius, respectively, as discussed in [Paper-I](#) and [Paper-II](#). Secondly, the initial distribution of star clusters within the host galaxy is nearly isothermal, so that the approximations that  $V_{\text{orb}} = V_v$  and  $R_{\text{orb}} = u_r f_{\text{gas}} R_v$  may be valid. This is consistent with the GC evolution model of [Rodríguez et al. \(2023\)](#), see their figure 10) based on the post-processing of the FIRE-2 simulation and a cluster Monte Carlo code, where the effective tidal strength is found to be well described by the expectation of an isothermal sphere. Finally, the upper bound of  $u_r$  comes from observations that GCs can extend to large radius, such as  $0.1 R_{\text{vir}}$  or even beyond (e.g. [Kantha et al. 2014](#); [Alabi et al. 2016](#); [Forbes & Remus 2018](#); [Dornan & Harris 2023](#)).



Combining Eqs. (2) and (4) for halo virial velocity and radius, respectively, and substituting the time variable with  $H = \dot{a}/a$  and  $a = 1/(1+z)$ , Eq. (66) can be analytically integrated from the initial redshift  $z_0$  to arbitrary redshift  $z < z_0$ :

$$M_{\text{cls}}(z) = M_{\text{cls}}(z_0)(1-R) \times \left[ 1 - \frac{(1-\beta_{\text{tid}})\nu_0}{u_{\text{r}}f_{\text{gas},0.04}} M_{\text{cls},5.3}^{\alpha_{\text{tid}}}(z_0) \ln \left( \frac{1+z_0}{1+z} \right) \right]^{\frac{1}{1-\beta_{\text{tid}}}}, \quad (68)$$

where  $M_{\text{cls}}(z_0) = 2 \times 10^5 M_{\odot} M_{\text{cls},5.3}(z_0)$ ,  $f_{\text{gas}} = 0.04 f_{\text{gas},0.04}$ , and  $R$  is the returned fraction of mass (Eq. 17). Note that the change of tidal environment in mergers is difficult to model. We ignore such effects in our modeling and apply Eq. (68) to all star clusters, regardless of whether or not they have merged into other galaxies. This is a rough approximation, but may be reasonable given that tidal disruption is more significant at higher  $z$ , so that most of the mass loss is expected to occur in the galaxy where star clusters were born (e.g. Kruijssen 2014).

To gain some intuition of the disruption, we define the disruption timescale for a star cluster as  $\tau_{\text{tid}} = |m/\dot{m}|_{z=z_0}$ , and by using Eq. (66), we obtain

$$\begin{aligned} \tau_{\text{tid}} &= u_{\text{r}} f_{\text{gas},0.04} M_{\text{cls},5.3}^{-\alpha_{\text{tid}}}(z_0) \nu_0^{-1} H^{-1}(z_0) \\ &= u_{\text{r}} f_{\text{gas},0.04} M_{\text{cls},5.3}^{-\alpha_{\text{tid}}}(z_0) \nu_0^{-1} \times \begin{cases} [0.82 \text{ Gyr}] (1+z)_{10}^{-3/2} \\ [5.00 \text{ Gyr}] (1+z)^{-3/2} \end{cases}. \end{aligned} \quad (69)$$

The dependence of  $\tau_{\text{tid}}$  on  $M_{\text{cls}}$  has a power-law index of  $2/3$  in our fiducial choice, close to the analytically-estimated and observed values, 0.62 and 0.60, respectively, reported by Lamers et al. (2005). The dependence of  $\tau_{\text{tid}}$  on the tidal frequency (Eq. 66) implies a dependence of  $\tau_{\text{tid}}$  on the ambient gas density,  $\tau_{\text{tid}} \sim \rho_{\text{gas}}^{-1/2}$ , consistent with N-body simulations and observations shown by Lamers et al. (2005). The disruption timescale is proportional to the Hubble timescale, and does not explicitly depend on halo mass, indicating that the GCS mass-halo mass relation is not distorted by the dynamical evolution while the normalization decreases as the formation of GCs stops. The short disruption timescale at  $z = 9$  indicates that nearly all GCs formed at such high redshift are eventually disrupted. The relatively long disruption timescale at  $z = 2$  suggests that massive GCs born with  $M_{\text{cls},5.3} \gtrsim 1$  at  $z = 2$  can survive until  $z = 0$ . At  $z = 0$ , the disruption timescale is about 3 Gyr for a cluster with  $u_{\text{r}} = 0.5$ ,  $f_{\text{gas}} = 0.04$  and  $M_{\text{cls}} = 10^4 M_{\odot}$ , falling into the range found by Lamers et al. (2005) using observational data. Variations of GC disruption among halos due to their differences in GC formation history are allowed in Eqs. (67) and (68) through the gas fraction  $f_{\text{gas}}$  and time variables  $t$  and  $z_0$ . Note that we have ignored substructures of galaxies, such as clumps, spiral arms and bars. These should be included in the future with detailed modeling of the galactic structure.

#### 4 MODEL PREDICTIONS AND COMPARISON WITH OBSERVATIONAL DATA

In this section, we combine the physical recipes described in §2 and §3, and implement them into (sub)halo merger trees taken from a dark-matter-only simulation. The product of the implementation is the galaxy, including its gaseous, stellar and SMBH components, and globular clusters, for each subhalo in the simulation. A variety of summary statistics are provided for comparisons with currently available observations and other GC models. Other predictions are provided to be tested by future observations.

The simulation used here is the TNG100-1-Dark run, conducted as a part of the IllustrisTNG project (Pillepich et al. 2018; Nelson et al. 2019). The cosmology adopted by the simulation is consistent with that used in this paper (see §1). The run has a periodic box with a side length of  $75 h^{-1} \text{Mpc}$ ,  $1820^3$  dark matter particles, each with a mass of  $6.0 \times 10^6 h^{-1} M_{\odot}$ , a Plummer equivalent gravitational softening length varying from  $1 h^{-1} \text{kpc}$  at high  $z$  to  $0.5 h^{-1} \text{kpc}$  at low  $z$ . A total of 100 snapshots spanning from redshift  $z = 20.0$  to 0 have been saved. Halos are identified using the friends-of-friends (FoF) algorithm with a scaled linking length of 0.2 (Davis et al. 1985). Subhalos are identified using the SUBFIND algorithm (Springel et al. 2001; Dolag et al. 2009), and subhalo merger trees are constructed using the SUBLINK algorithm (Springel 2005; Boylan-Kolchin et al. 2009; Rodriguez-Gomez et al. 2015). The lower limit for FoF halo mass is about  $2 \times 10^8 h^{-1} M_{\odot}$ , and the most massive halo at  $z = 0$  in the simulation volume has  $M_{\text{v}} = 2.47 \times 10^{14} h^{-1} M_{\odot}$ . The main progenitor of a subhalo is defined as the one with the most massive history among all progenitors (De Lucia & Blaizot 2007; Rodriguez-Gomez et al. 2015). The central subhalo of a FoF halo is defined as the one with the most massive history among all subhalos within the halo. The main branch of an FoF halo corresponds to the main branch of its central subhalo. The specific run we choose ensures a balance between statistical robustness and resolution in halo assembly histories.

#### 4.1 Numerical implementation of the model

The numerical algorithm takes each subhalo merger tree as the input unit, and processes it by the steps summarized below.

- (i) **Decomposition of halo assembly history:** The subhalo merger tree is decomposed into a set of disjoint branches. Physical quantities in each branch are smoothed by a running kernel, with the kernel size given by the dynamical timescale,  $t_{\text{dyn}}$ . Each branch is decomposed into two stages, a central stage and a satellite stage. The mass assembly history,  $M_{\text{v}}(z)$ , during the central stage is fitted to a parametric function. The specific halo growth rate,  $\gamma(z)$ , derived from the parametric fitting, and a threshold,  $\gamma_{\text{f}}$ , are used to separate the central stage into two phases: a fast phase with  $\gamma(z) \geq \gamma_{\text{f}}$ , and a slow phase with  $\gamma(z) < \gamma_{\text{f}}$ . The details of this step are described in §2.1.
- (ii) **The amount of cooled gas:** At each time step in a branch, the total amount of available gas,  $\Delta M_{\text{g,avail}}$ , is given by Eq. (7). The amount of gas cooled down to the SGC,  $\Delta M_{\text{g,cool}}$ , is modified by the cooling factor,  $F_{\text{cool}}$ , given by Eq. (9).
- (iii) **Star formation and SMBH growth:** Taking into account the feedback from AGN and supernova, the amount of star-forming gas,  $\Delta M_{\text{g,sf}}$ , is a fraction  $F_{\text{sn}} F_{\text{agn}}$  (Eqs. 14 and 15) of the cooled gas. The amount of formed stars,  $\Delta M_{\text{*}}$ , is given by Eq. (16), from which SFR is also obtained. The growth of SMBH,  $\Delta M_{\text{bh}}$ , is given by Eq. (18). The amount of gas remaining in the SGC,  $\Delta M_{\text{g}}$ , is obtained by the conservation of mass (Eq. 20). Star formation in the satellite stage is assumed to follow an exponential decay (Eq. 21), and the gas is modeled assuming a ‘close-box’. Galaxy mergers are modeled by assuming that a fraction,  $f_{\text{merge}}$ , of the stellar mass of the infall galaxy is added to the main branch.
- (iv) **Metal enrichment:** Metal yield and recycling are modeled by following the idea of the gas regulator, with mixing and escaping fractions modified for the gaseous component that hosts star clusters. The details are described in §2.4. To account for the missed fluctuations,

**Table 1.** List of the model components, their fiducial parameters and the sources of the values. See §4.1 for a list of the steps of the numerical implementation. The parameters calibrated in this paper are detailed in Appendix B.

Model Component	Fiducial Parameters	Sources
Halo assembly and galaxy formation (§§2.1, 2.2, 2.3)	-	Calibration in Paper-I and L14
Metal enrichment (§2.4)	$V_{\text{esc}} = 75 \text{ km s}^{-1}$ , $\beta_{\text{esc}} = 2$ , $z_{\text{esc}} = 5$ , $\gamma_0 = 1$ , $\beta_{\text{mix}} = 2$	This paper
Sub-cloud formation (§3.1)	$\beta_{\text{sc},\text{m}} = -2$ , $M_{\text{sc},\text{t}} = 10^{6.5} M_{\odot}$ ; $f_s = 1$ ; $V_w = 250 \text{ km s}^{-1}$ ; $\alpha_s = 1.5$	Star cluster mass function by e.g. Krumholz et al. (2019); This paper; The same value as §2.3 for the galactic-scale model; Girichidis et al. (2014) and Kiihne et al. (2025)
Sub-cloud fragmentation (§3.2)	$\beta_{\text{sc},\text{n}} = -2.5$	This paper
Star formation within sub-cloud (§3.4)	$\epsilon_{\text{w},\text{max}} = 1$ ; $f_{\text{r},\text{cls}} = 1/2$	Dekel et al. (2023); Isothermal assumption
GC formation (§3.5)	$n_{\text{snf}} = 10^{3.5} \text{ cm}^{-3}$	Dekel et al. (2023)
Star cluster dynamical evolution (§3.6)	$\alpha_{\text{tid}} = -2/3$ , $\beta_{\text{tid}} = -1/3$ ; $\nu_0 = 0.6$	Gieles & Gnedin (2023); This paper

a Gaussian random number with  $\sigma_{\log Z} = 0.1$  dex is added to the metallicity  $Z$ .

- (v) **Sampling of sub-clouds:** A set of sub-clouds is randomly sampled, with initial mass  $M_{\text{sc}}$  following the distribution given by Eq. (30), and with the initial density  $n_{\text{sc}}$  following the distribution given by Eq. (31).  $M_{\text{sc}}$  and  $n_{\text{sc}}$  are assumed to be independent of each other at formation, but subsequent processes, e.g. external feedback and star formation, can lead to correlations. The size of a sub-cloud,  $R_{\text{sc}}$ , is obtained from  $M_{\text{sc}}$  and  $n_{\text{sc}}$ . The metallicity of a sub-cloud is assumed to follow the galactic average given by the previous step, with an additional 0.3 dex random fluctuation added to account for variations among sub-clouds. Because the timescale involved in sub-cloud generation and dispersal can be much shorter than the time interval between two adjacent snapshots saved by the simulation, we use the amount of stars to constrain  $N_{\text{sc}}$ , the number of sub-clouds to be sampled at each snapshot. This is achieved by requiring that the total amount of stars formed in all sub-clouds to be equal to that of the entire galaxy:  $\sum_{i \leq N_{\text{sc}}} M_{\text{cls},i} = \Delta M_*$ , where  $M_{\text{cls}}$  is given by Step (viii) and  $\Delta M_*$  is modeled in Step (iii).
- (vi) **Cooling and fragmentation:** The threshold density,  $n_{\text{sf},1}$ , at which a sub-cloud is able to fragment and form stars, is obtained according to Eq. (44). If the initial density is so low that  $n_{\text{sc}} < n_{\text{sf},1}$ , the fragmentation and star formation are delayed to a later time when the sub-cloud cools and contracts to a density  $n'_{\text{sc}}$  sampled from the distribution function given by Eq. (45). On the other hand, if  $n_{\text{sc}} \geq n_{\text{sf},1}$ , the sub-cloud fragments immediately. For convenience, we set  $n'_{\text{sc}} = n_{\text{sc}}$ .
- (vii) **External feedback:** A sub-cloud can survive the feedback from previous generations of stars within the galaxy if the initial density of the sub-cloud is high enough to shield against the feedback. In this paper, we only include the wind feedback (Eq. 48), as its effect is estimated to be more significant than the radiative feedback (Eq. 51) on sub-cloud scales. If a sub-cloud is not shielded, we remove it from the set of sub-clouds.
- (viii) **Star formation in sub-clouds:** The fraction of gas converted into stars in each sub-cloud, and thus the mass of the resulted star cluster,  $M_{\text{cls}}$ , is determined by the stellar feedback within the sub-cloud (Eqs. 54 and 57). We adopt the wind feedback in the fiducial model, while leaving other choices optional. With alternative choices of feedback, the power-law index of the size-mass relation of star clusters differs within a narrow range of 1/6–1/4, and the dominant

channel of feedback is still unconstrained by the current observations. The fiducial parameters are chosen so that the star formation efficiency in a sub-cloud is  $\epsilon_w = 1$  at  $M_{\text{sc}} = 10^6 M_{\odot}$ ,  $R_{\text{sc}} = 12$  pc and  $Z = 0.02$ , consistent with both our theoretical expectations in §3.4 and the observed truncation mass and size of young massive clusters and globular clusters (e.g. Krumholz et al. 2019).

- (ix) **Selection of globular cluster:** At formation, a star cluster is classified as a (progenitor of) GC if (i) the star formation in the sub-cloud is supernova-free, i.e.  $n'_{\text{sc}} \geq n_{\text{snf}}$ , and (ii) the stellar mass  $M_{\text{cls}} \geq M_{\text{gc},\text{min}} = 10^4 M_{\odot}$ . The mass limit set by the second criterion is roughly the threshold adopted to classify an observed star cluster as a GC (e.g. Kruijssen et al. 2019b), and is also adopted by other models (e.g. Chen & Gnedin 2023). We have checked that this lower bound of mass is sufficient to robustly obtain all the statistics of GCs, because the peak of the cumulative GC mass function is much larger than this lower bound (see §4.2). As discussed in §3.5, a GC is classified as Pop-I if  $n_{\text{sf},1} < n_{\text{snf}}$ , and otherwise classified as Pop-II. These two populations directly match the metal-rich (red) and metal-poor (blue) populations, respectively, found in observations. Once a side-branch galaxy is merged into the main branch, all of the side-branch GCs are added to the merger remnant. The strong tidal field in the merger process can strip GCs from the infalling galaxy and spread them over a large range of galactocentric distance, as to be discussed in §4.6. GCs formed in the main and side branches are referred to as the in-situ and ex-situ populations, respectively.
- (x) **Dynamical evolution:** The change of stellar mass of a star cluster in the galactic tidal field is modeled according to the time integration, from the birth redshift  $z_0$  to the observed redshift  $z$ , given by Eq. (68), with a randomly sampled effective orbital radius within the SGC. Consequently, a star cluster born as a GC, i.e.  $M_{\text{cls}}(z_0) \geq M_{\text{gc},\text{min}}$ , can gradually lose its mass, and begin to be classified as a non-GC (e.g. open) star cluster or a diffuse stellar component, once  $M_{\text{cls}}(z) < M_{\text{gc},\text{min}}$ .

The above pipeline involves a number of random sampling procedures (e.g. those for  $M_{\text{sc}}$ ,  $n_{\text{sc}}$ ,  $n'_{\text{sc}}$ ), which are all difficult to carry out directly. This is due to several reasons. Firstly, the ranges of quantities to be sampled are wide, and the probability densities vary significantly over these ranges. For example, the distribution of  $M_{\text{sc}}$  has a power-law index  $\approx -2$  (Eq. 30), implying that the number of sub-clouds per unit logarithmic mass differs by four orders of magnitude between  $10^4$  and  $10^8 M_{\odot}$ . The consequence of this is that sub-populations are highly imbalanced, potentially leading to large

statistical fluctuations for the rare population (e.g. GC) when the sample size of dark matter halos is limited. Secondly, the number of sub-clouds to sample is rather large even for a single halo. For example, the total number of sub-clouds to sample is about  $1.5 \times 10^7$  for a subhalo merger tree rooted in a present-day Milky Way-size subhalo with  $M_{v,z=0} \approx 10^{12} h^{-1} M_\odot$ , and more than  $2 \times 10^8$  for a cluster halo of  $10^{14} h^{-1} M_\odot$  (see Fig. A1). This presents a great challenge for computation, especially when we want to generate samples of GCs on cosmological scales.

For the sake of statistical robustness and computational efficiency, we design a ‘balanced’ sampling algorithm (referred to as BSAMPLING hereafter) to generate sub-clouds. Briefly, the algorithm defines a set of proposal distributions  $q^{(j)}(x^{(j)})$ , one for each property  $x^{(j)}$  to be sampled, as replacements of the original distributions  $p^{(j)}(x^{(j)})$ . Once a sub-cloud, represented by a set of its properties  $\mathbf{x}_i = (x_i^{(1)}, x_i^{(2)}, \dots)$ , is drawn from the proposal distributions, a weight

$$w_i \equiv \prod_j \frac{p^{(j)}(x_i^{(j)})}{q^{(j)}(x_i^{(j)})} \quad (70)$$

is assigned to it to compensate for the bias between the proposal and original distributions. The weights of sub-clouds are normalized by  $N_{sc}$ , the total number of sub-clouds to be sampled, as  $\sum_i w_i = N_{sc}$ , so that a weight  $w_i > 1$  represents multiple sub-clouds, therefore reducing the computational cost. Summary statistics derived from the sampled sub-clouds need to incorporate these weights. If  $q^{(j)}$  is carefully chosen so that it is more uniform than  $p^{(j)}$ , the statistical fluctuation can be reduced. If a real, un-weighted sample of sub-clouds is needed for, e.g. mock observations, it can be generated by resampling  $N_{sc}$  times from the discrete values  $\{\mathbf{x}_i\}$ , according to probabilities given by  $\{w_i / \sum_i w_i\}$ . The idea here is motivated by the importance sampling technique in Monte Carlo integrations, and by the sampling-importance-resampling (SIR) technique in the discrete approximation of continuous distributions (see e.g. chapter 11 of Bishop 2006). A formal description of this sampling technique and the specific choice for this paper are detailed in Appendix A.

Table 1 lists the parameters adopted in this paper for each component of the model. The free parameters that cannot be fixed via theoretical arguments, hydrodynamical simulations or direct observations need to be calibrated by summary statistics of observations, which are detailed in Appendix B. In the remainder of this paper, we present the results of the model and discuss their physical implications.

## 4.2 Mass and age distributions

Fig. 9 shows the mass functions of GCs in central galaxies at  $z = 0$  in three different ranges of halo mass. Here, the mass function is defined as  $dN/d \log M_{cls}$ , the number of GCs per unit logarithmic mass, and the result is averaged over all central galaxies in the given range of halo mass. Both the in-situ and ex-situ components are included. The birth-time mass function, obtained by selecting GCs and using statistics based on their masses at formation (see §4.1 for the selection criteria), is shown by the grey curve. The slope of the mass function in the logarithmic scale is a constant of  $\approx 0.7$  at  $M_{cls} \lesssim 10^6 M_\odot$ , due to the power-law form, with an index of  $\beta_{sc,m} = -2$ , of the sub-cloud mass function (Eq. 30), and the decreasing star formation efficiency with decreasing sub-cloud mass (Eq. 55). The steepening of the mass function at the high-cluster-mass end is due to the exponential truncation of the sub-cloud mass function. The present-day mass function, obtained by taking into account the effects of dynamical

evolution (§3.6), is shown by the black curve. The difference between the present-day mass function and that at the birth time highlights the effect of mass loss. As GCs with lower mass have shorter tidal disruption timescales (Eq. 69), the mass loss is quicker for lower-mass GCs, leading to greater suppression of the mass function towards lower cluster mass. The dynamical evolution also changes the shape of the mass function, from a monotonical form at birth to a unimodal form at the present day.

The peak of the unimodal distribution is around  $10^5 - 10^{5.5} M_\odot$ , with moderate dependence on the host halo mass. Such a unimodal distribution also ensures that the lower limit of sub-cloud mass,  $M_{sc,min} = 10^4 M_\odot$  (Eq. 30), and the lower limit of GC mass,  $M_{gc,min} = 10^4 M_\odot$  (§4.1), are sufficient to obtain the summary statistics for the observed population of GCs.

The red and blue curves in each panel of Fig. 9 show the mass functions of Pop-I and Pop-II GCs, formed via the two channels defined in §3.5, respectively. The mass functions of the two populations are quite similar in shape, both being unimodal. The mass function of Pop-II GCs appears more top-heavy, which is because this population on average is born earlier, and thus has a longer time for mass loss and a higher probability for the low-mass ones to be disrupted. The amplitudes of the mass function of both populations increase with increasing halo mass, as we will discuss in more detail in §4.4. Pop-I is sub-dominant in central galaxies with  $M_{v,z=0} < 10^{11.5} h^{-1} M_\odot$ , but becomes comparable to Pop-II in more massive halos. This is a direct outcome of the more enriched ISM in galaxies that reside in more massive halos, as shown in Fig. 3 and §2.4.

In the center panel of Fig. 9, we also include the observed mass functions of GCs in the Milky Way (green curve) and M31 (purple curve), compiled by Rodriguez et al. (2023, see their figure 3) using catalogs from Harris (1996, 2010) and Caldwell et al. (2011), respectively. The observed GC mass function of M31 has an amplitude about 0.5 dex higher than that of the MW, and appears more top-heavy. This may be explained partly by the more massive halo of M31, and partly by the fact that it has more recent mergers that can bring in ex-situ GCs as well as increase the in-situ formation of GCs (see the age distribution below; see also, e.g. §4.3 of Chen & Gnedin 2024). The mass function of GCs predicted by our model (black curve) falls between those of MW and M31 over the entire range of  $M_{cls}$ , indicating that the model is capable of reproducing the average GC mass function for MW-size galaxies. The observed mass functions of MW and M31 are well within the range of the model prediction (light shade), indicating that they are not outliers in the ensemble of MW-sized galaxies predicted by our model.

Fig. 10 shows the age distributions of GCs in the same sets of central galaxies as in Fig. 9. In each panel, histograms of the birth redshift are shown for star clusters born as GCs (grey curve) and for the ones that can survive to the present. For comparison, in the middle panel, we also show the results of the empirical model of Chen & Gnedin (2024) for MW (green curves) and M31 (purple curves), obtained by calibrating the model with observations and by populating GCs in appropriate halos in simulations. The results shown here are the averages over their three best-match realizations for both MW and M31. Their adopted halo masses for MW and M31 are about  $10^{12.1} M_\odot$  and  $10^{12.25}$ , respectively, which gives a slightly larger number of GCs in M31 than in MW. Their selections of MW-like and M31-like halos are observationally motivated, so that there is no major merger in the past 10 Gyr for the MW case and there is at least one major merger in the past 6 Gyr for the M31 case. This, combined with their merger-triggered GC formation scenario, predicts a larger and younger population of GCs in M31 than in MW, as seen from the excess of young GCs in M31 at  $z \lesssim 1$ . The fraction

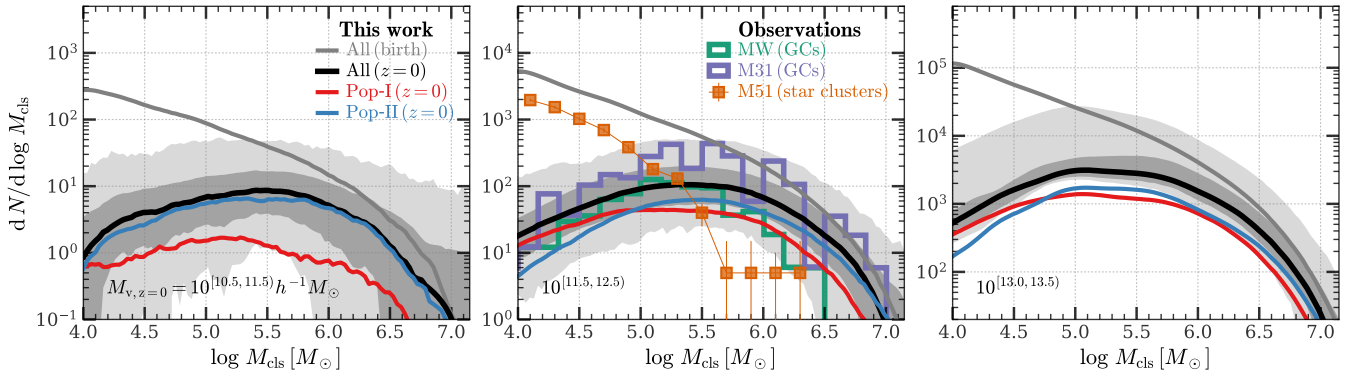


**Figure 9.** Mass functions of GCs. Different panels show the mass functions of GCs in central galaxies with different halo masses at  $z = 0$ . Both in-situ and ex-situ GCs are included. In each panel, **grey** curve shows the birth-time mass function of all GCs formed in the history. **Black** curve shows the  $z = 0$  mass function of GCs survived after the mass loss due to dynamical evolution is incorporated, with dark shade showing the  $1-\sigma$  range among individual galaxies and light shade showing the minimum to maximum. **Red** and **blue** curves show the Pop-I and Pop-II sub-components, respectively, of the black curve. See §4.1 for the details of modeling and sample selection. In the center panel, the histograms show the observed GC mass functions for MW (**green**) and M31 (**purple**), compiled by Rodriguez et al. (2023). **Orange** markers show the mass function of star clusters in M51, obtained from the star-cluster catalog of LEGUS (Messa et al. 2018). See §4.2 for a detailed discussion of this figure.

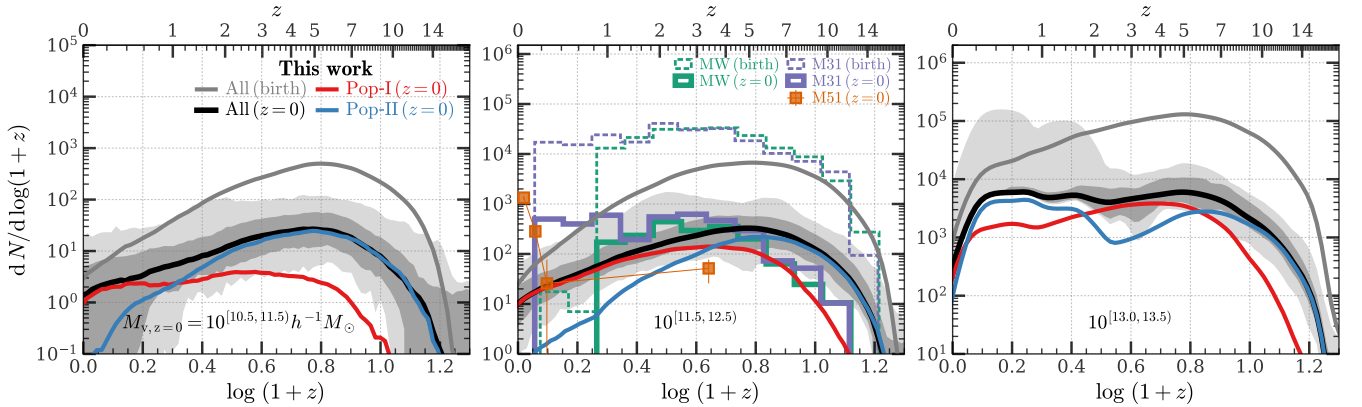


**Figure 10.** Age distributions of GCs. Different panels show the age distributions of GCs in central galaxies with different halo masses at  $z = 0$ . Both in-situ and ex-situ GCs are included. In each panel, **grey** curve shows the distribution of the birth time of all GCs formed in the history. **Black** curve shows that of GCs survived until  $z = 0$  after the mass loss due to dynamical evolution is incorporated, with dark shade showing the  $1-\sigma$  range among individual galaxies and light shade showing the minimum to maximum. **Red** and **blue** curves show the Pop-I and Pop-II sub-components, respectively, of the black curve. See §4.1 for the details of modeling and sample selection. In the center panel, the histograms show the results of the empirical model of Chen & Gnedin (2024) for MW (**green**) and M31 (**purple**). Their results for all and survived GCs are shown by **dashed** and **solid** histograms, respectively. **Orange** markers show the age distribution of star clusters more massive than  $10^5 M_\odot$  in M51, obtained from the star-cluster catalog of LEGUS (Messa et al. 2018). See §4.2 for a detailed discussion of this figure.

of disrupted GCs predicted by their model is significantly larger than ours, although the predicted number of GCs at  $z = 0$  is similar in both models. This highlights the degeneracy between GC formation and disruption in the modeling, which are respectively controlled by the parameters ( $p_2, p_3$ ) and  $\kappa$  in Chen & Gnedin (2024, see their §2.2), and by  $n_{\text{snf}}$  (§3.5) and  $v_0$  (§3.6) in our model.

A key difference between our model and theirs is that we include the Pop-II (metal-poor) channel which elevates GC formation in metal-poor galaxies, mainly low-mass galaxies at high  $z$ . The consequence is the enhanced GC formation at high redshift, which produces an age distribution peaked at  $z \approx 5$ , roughly the peak redshift for cosmic bulge formation (Paper-I), instead of at  $z \approx 2$ , the peak redshift of the cosmic star formation history (e.g. Madau & Dickinson 2014). Thus, a stronger connection between GCs and bulges is predicted by our model in comparison to other models and early observations. The new GC candidates in the galactic bulge discov-

ered recently by Gaia (Palma et al. 2019; Camargo & Minniti 2019; Minniti et al. 2021) appears to support the prediction of our model. The empirical model of GC formation by Valenzuela et al. (2021, see also Valenzuela et al. 2024) also supports the presence of a distinct channel in the early Universe. Metal-poor GCs in present-day central galaxies hosted by halos below the MW-halo mass are dominated by the in-situ component, and thus have systematically older age than the metal-rich counterparts, as seen in the left and center panels. On the other hand, for cluster-size halos, the age distribution of metal-poor GCs in their central galaxies is bimodal, as seen from the right panel of Fig. 10. The additional metal-poor, low- $z$  mode in our model is due to the ex-situ GCs brought in by satellite galaxies merged into the central, and it is consistent with the inference by, e.g., Harris (2023) from observations of bright elliptical galaxies.

The difference between MW and M31 in the mass and age distributions of GCs indicates the diversity of GC formation in galaxies



with different states and assembly histories. To clearly see this, we consider another galaxy, M51 (NGC 5194), a spiral galaxy interacting with a massive companion, NGC 5195. The stellar mass of M51 is inferred to be  $\approx 10^{10.6} M_{\odot}$  (Leroy et al. 2008; Wei et al. 2021), slightly smaller than that of MW. We take the star-cluster candidates of the LEGUS survey for M51 (Messa et al. 2018), remove the contamination by selecting only those with machine-learning class 1 or 2, and exclude those with age less than 10 Myr to avoid unbound systems. The mass distribution of the star clusters so obtained is shown in the center panel of Fig. 9. We further restrict the sample to massive clusters with  $M_{\text{cls}} \geq 10^5 M_{\odot}$  so that they are age-complete (see Fig. 5 of Messa et al. 2018), and show the age distribution of these clusters in the center panel of Fig. 10. At  $M_{\text{cls}} \geq 10^5 M_{\odot}$ , the cluster mass function of M51 is much lower than those of MW, M31 and the model prediction. The age distribution shows that these massive clusters are mostly born at  $z < 0.5$  by recent star formation, and none of them are as old as those produced at  $z \approx 5$ , the peak of the GC-formation activity predicted by our model. Such a situation can be created if M51 forms very late, and is hosted by a halo with very stable dynamical environment in the early stage. The lack of galactic-scale turbulence thus suppresses the formation of old and massive GCs, and large amounts of GCs are produced only later by gas compression through, e.g. disk instabilities and/or external interactions (see the discussion in §3.1). Even considering the extreme ranges of the mass and age distributions predicted by our model (light shades in Figs. 9 and 10), the observed distributions of M51 are still outliers. This highlights the importance of explicitly modeling effects of galaxy interactions on the formation of GCs. Such interactions can complement and even dominate the source of turbulence in the ISM, and may produce a density distribution different from that based on the assumption of the single Mach number given by Eq. (36).

### 4.3 The size-mass relation

In addition to marginal distributions of individual GC properties, a number of joint distributions have also been shown in the literature to characterize the interconnection among different physical processes. One of such relations is the GC size-mass relation, or more formally the size distribution conditioned on the mass,  $p(R_{\text{cls}}|M_{\text{cls}})$ . The importance of this relation can be understood by applying the virial theorem to individual bound star clusters. At a given GC mass, the binding-energy distribution of GCs at the birth-time depends on their stellar density profiles which are related to the histories of gas dissipation (cooling). The subsequent dynamical processes of a GC, such as mass segregation, binary hardening, black-hole heating, core collapse, evaporation and tidal heating, can cause changes in the distribution of stars and exchanges between the cluster and its environment (see Portegies Zwart et al. 2010, for a review). The histories of these processes can thus leave imprints on the size of a GC, and shape the final size-mass relation of GCs.

Fig. 11 shows the birth-time size-mass relation of GCs, both in-situ and ex-situ, in central galaxies with  $M_{\text{v},z=0} \in 10^{[11.5, 12.5]} h^{-1} M_{\odot}$ . Results for other halo masses are similar and not shown here. As discussed in §3.4, the amount of gas converted into stars before the dispersal of a sub-cloud by internal stellar feedback is determined by the balance between feedback energy and binding energy. Thus, the size-mass relation of GCs is a direct reflection of the gravity-feedback relation. As our fiducial model adopts the wind feedback, the resulted GC size-mass relation is expected to have a power-law index of  $\approx 1/5$  (Eq. 62), smaller than the  $1/3$  power-law index expected from the assumption of a constant density for all GCs. This is seen from the median relation shown by the black solid curve in

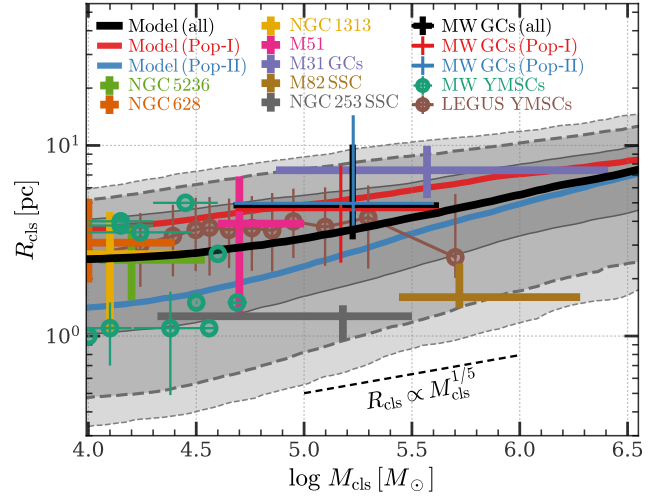


**Figure 11.** Size-mass relation of GCs. **Thick black** curve shows the model prediction of the birth-time median size at a given mass by stacking all GCs formed in the histories of central galaxies with  $10^{11.5} \leq M_{\text{v},z=0} / (h^{-1} M_{\odot}) < 10^{12.5}$ . Both in-situ and ex-situ GCs are included in the analysis. Here  $R_{\text{cls}}$  is defined as the half-mass radius of GC. Shaded areas, from inner to outer, encompass 1, 2 and 3- $\sigma$  ranges, respectively. **Red** and **blue** curves show relations of Pop-I and Pop-II GCs, respectively. Star clusters compiled by Krumholz et al. (2019) from observations for individual galaxies also shown: Each **cross marker** represents the median and 1- $\sigma$  range of all observed massive ( $M_{\star} \geq 10^4 M_{\odot}$ ) star clusters in a given galaxy; each **green circle** represents a single YMSC in MW, with the error bar indicating the uncertainty for this star cluster. For MW GCs, we compile the catalog of Harris (1996, 2010 edition) and Baumgardt & Hilker (2018), and show the results for all, Pop-I and Pop-II of them by **black**, **red** and **blue cross markers**, respectively. **Brown circles** with error bars are running median and 1- $\sigma$  uncertainty for a large sample of YMSCs in the LEGUS survey obtained by Brown & Gnedin (2021). The observed size-mass trend of GC is very weak and the scatter of GC size is large even in a single galaxy. The power-law index of our prediction, due to the adoption of wind feedback, is about  $1/5$ , as indicated by the **black dashed line** (see Eq. 62), consistent with the observation of Brown & Gnedin (2021) for YMSCs. The present-day size-mass relation of GCs is expected to be similar if GCs evolve along their birth-time relation. See §4.3 for a detailed discussion of this figure.

Fig. 11 at  $M_{\text{cls}} \geq 10^{5.5} M_{\odot}$ . At lower  $M_{\text{cls}}$ , the effect of metallicity becomes important, as seen from the divergence of the red (Pop-I) and blue (Pop-II) curves, and the median relation for all GCs becomes flatter and has a larger scatter. This is expected, as massive stars formed in metal-rich ISM evolve faster, strengthening the feedback and lowering the mass of Pop-I GCs relative to that of Pop-II GCs formed in sub-clouds with comparable mass and density.

Symbols in Fig. 11 show the sizes and masses of massive star clusters compiled by Krumholz et al. (2019) and obtained by Brown & Gnedin (2021) from the HST/LEGUS survey. For MW GCs, we take the catalog of Harris (1996, 2010 edition) for metallicity, and incorporate the size and mass measurements from Baumgardt & Hilker (2018). We use a two-component Gaussian mixture model to fit the metallicity distribution of MW GCs, classify them into Pop-I and Pop-II, and show the sizes and masses separately for all, Pop-I and Pop-II GCs using three markers with different colors. Note that classifications of star clusters are not clean-cut and may not carry particular physical significance (see discussion in, e.g. §1 of Krumholz et al. 2019). YMSCs traditionally refer to massive bound star clusters with young age ( $M_{\text{cls}} \geq 10^4 M_{\odot}$ , age  $< 100$  Myr); GCs in the MW are considered old (age  $\geq 6$  Gyr; see Fig. 10) but

those in M31 are not; star clusters in some other galaxies do not even have a clear classification. Despite of the wide range of age, nearly all the observed sizes and masses of massive clusters fall well within the  $2\text{-}\sigma$  range of our model prediction. The amplitude and slope (in logarithmic scale) of the size-mass relation obtained by [Brown & Gnedin \(2021\)](#) for LEGUS YMSCs are very close to our model prediction, thus providing support to our model. Given the large scatter in the observed cluster size at given cluster mass and the significant galaxy-galaxy variation, it is still difficult to use the observed relation to constrain different feedback channels.

Another uncertainty arises from the dynamical evolution of GCs, which can not only change their masses, as modeled in §3.6, but also modifies their sizes. As our model does not track the change of the GC size during the dynamical evolution, it is unclear whether or not the present-day size-mass relation is different from that at the birth time. Some studies have suggested a ‘two-phase’ scenario for the size evolution in the tidal field (e.g. [Gieles & Portegies Zwart 2011](#)): an early ‘expansion-dominated’ phase before the cluster becomes Roche lobe filling, and a later ‘evaporation-dominated’ phase. The starting point and the duration of the two phases thus depend on the initial conditions for cluster formation. Using N-body simulations, [Kruijssen et al. \(2011, see their figure 2\)](#) found that, during the second phase, the evolution paths of individual star clusters in the size-mass plane follows the observed size-mass relation at  $z = 0$ . Thus, if a population of GCs are born on the local size-mass relation, as suggested by our analysis, they are expected to follow the observed relation after the dynamical evolution. We note that the birth-time size-mass relation of star clusters, as well as other initial conditions for their subsequent dynamical evolution, is set up by a complex interplay of stellar physics, gas magnetohydrodynamics, and radiative transfer, which is not well understood and constrained theoretically and observationally (see §3 of [Portegies Zwart et al. 2010](#), for a review). Our model that star-clusters are born in the observed size-mass relation and evolve along it thus only represents a possible solution. Whether this is a coincidence due to model simplification or a more general result remains to be determined. Taking MW GCs as an example, the sizes and masses of Pop-I and Pop-II GCs have no obvious difference in median, but the sizes of Pop-II GCs appear to be skewed towards larger values, as seen from the error bar. This is potentially due to the older age, and thus the longer time for dynamical evolution, of Pop-II GCs. Alternatively, it may originate from the different tidal environments of the two populations. In such cases, dynamical evolution is required to drive them off the birth-time size-mass relation which lies below the observed one. [Arca Sedda et al. \(2024, see their figure 2 and §3\)](#) used N-body simulations and reported such a possible path for the size-mass evolution: star clusters are initially small and under-filling the Roche lobes, but expand to the observed range of sizes within a timescale of  $\lesssim 1$  Gyr due to internal dynamical effects.

#### 4.4 Connection to host galaxies and halos

The systematic change in the distribution function of GCs with different host halo mass, as discussed in §4.2, indicates a strong connection between the GC population and the host galaxy and halo. An intriguing observational fact is the linear relation between the total mass of the GC population,  $M_*^{(\text{GCs})}$ , and the host halo mass,  $M_v$ , discovered by [Blakeslee \(1997, 1999\)](#). Follow-up studies have extended this relation to galaxies with wide ranges of masses (e.g. [McLaughlin 1999](#); [Spitler & Forbes 2009](#); [Harris et al. 2013](#); [Hudson et al. 2014](#); [Harris et al. 2015, 2017](#); [Burkert & Forbes 2020](#); [Forbes et al. 2020](#);

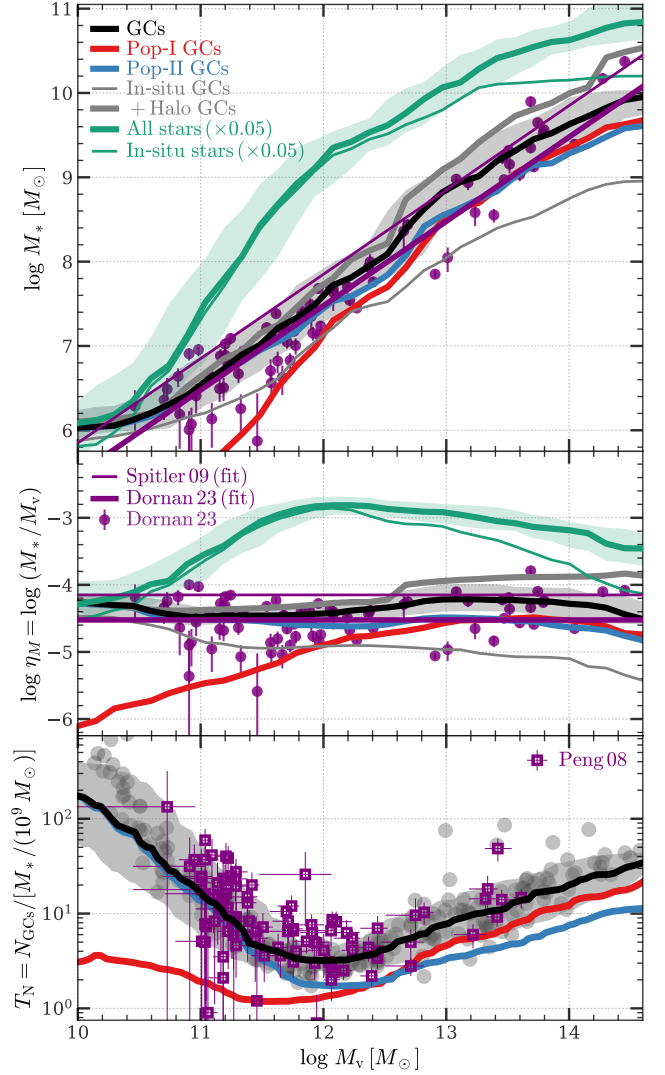


**Figure 12.** Total mass and number of GCs in galaxies at  $z = 0$ . All results are shown as a function of host halo mass,  $M_v$ . **Top panel** shows  $M_*^{(\text{GCs})}$ , the total mass of GCs within individual galaxies. **Middle panel** shows  $\eta_M$ , the ratio of  $M_*^{(\text{GCs})}$  and  $M_v$ . **Bottom panel** shows GC frequency,  $T_N$ , defined as the number of GCs,  $N_{\text{GCs}}$ , per  $10^9 M_\odot$  stellar mass of the host galaxy. **Thick black curve** is obtained by including all (in-situ + ex-situ) GCs within the central galaxy. **Red and blue curves** are obtained by only including Pop-I and Pop-II galactic GCs, respectively. **Thin grey curve** is obtained by only including in-situ galactic GCs. **Grey dots** show the results for galactic GCs of individual galaxies. **Thick grey curve** is obtained by including both galactic GCs and halo GCs (in satellite galaxies). For reference, **green curves** show  $M_*$ , the stellar mass of all stars (GC and non-GC), **thin** for in-situ only ( $f_{\text{merge}} = 0$ ) and **thick** for in-situ plus ex-situ ( $f_{\text{merge}} = 1$ ), both scaled by 5% for clarity. **Shaded areas** represent the  $1\text{-}\sigma$  ranges of the results. For comparison, **purple dots** show the observational results by [Dornan & Harris \(2023\)](#) for individual galaxies, and **thick purple line** shows their linear fit,  $M_*^{(\text{GCs})} = 3.0 \times 10^{-5} M_v$ . **Thin purple line** shows the linear fit,  $\log M_v = 4.15 + \log M_*^{(\text{GCs})}$ , obtained by [Spitler & Forbes \(2009\)](#). **Purple squares** show the results obtained by [Peng et al. \(2008\)](#) for individual galaxies from HST/ACS Virgo Cluster Survey, where we have converted their stellar mass to halo mass by the fitted relation obtained from our modeled galaxies. See §4.4 for a detailed discussion of this figure.

Dornan & Harris 2023), and found that it is obeyed by galaxies of different masses, from dwarfs to massive ellipticals. A key question for modeling the GC population is how such a relation is established by physical processes.

The top panel of Fig. 12 shows  $M_*^{(\text{GCs})}$ , the mass of the GC population obtained by summing up the masses of individual GCs within the galaxy, as a function of halo mass,  $M_v$ . Here, the analysis includes central galaxies at  $z = 0$  and the GCs survive in them. For convenience, the middle panel shows  $\eta_M$ , the GC mass fraction defined as the ratio between  $M_*^{(\text{GCs})}$  and  $M_v$ . For galactic GCs (in-situ + ex-situ; shown by the black curve), a linear relation,  $M_*^{(\text{GCs})} \propto M_v$ , is seen over the entire range of halo mass considered here. The  $1-\sigma$  residual, as shown by the grey shaded area, is about 0.3 dex, comparable to the root mean square error of 0.35 dex reported by Dornan & Harris (2023, see their §5). Including only the in-situ component decreases  $M_*^{(\text{GCs})}$  by a halo-mass-dependent factor, from negligibly small at  $M_v \approx 10^{10} M_\odot$ , to about 0.5 dex at  $10^{12} M_\odot$  and about 1 dex at  $\geq 10^{14} M_\odot$ . Including additionally halo GCs (formed in satellite galaxies) increases  $M_*^{(\text{GCs})}$  by a halo-mass-dependent factor, from negligibly small at  $M_v \leq 10^{12.5} M_\odot$ , to about 0.5 dex at  $\geq 10^{14} M_\odot$ , consistent with the results for the intracluster GCs obtained by Spitler & Forbes (2009) and Hudson et al. (2014). Separating galactic GCs into Pop-I and Pop-II components reveals the effects of metal enrichment on the two channels of GC formation, as already discussed in §4.2 using the mass function: below  $M_v \approx 10^{12.5} M_\odot$ , Pop-II GCs are dominating, while Pop-I GCs become comparable in abundance to and then slightly more abundant than Pop-II GCs above this halo mass. The difference between the two populations in the  $M_*^{(\text{GCs})}$ - $M_v$  relation found here is very similar to the result obtained by Harris et al. (2015, see their figure 7), and we will quantify this in more detail in §4.5.

The measurement of the  $M_*^{(\text{GCs})}$ - $M_v$  relation in observations has to deal with a number of systematic uncertainties in, e.g., the selection of GCs, sample incompleteness, etc. Collecting data published in the literature, we found that observational results generally agree with each other within about 0.3 dex, and the internal uncertainties originated from errors of individual data points are at a similar level (see e.g. figure 8 of Dornan & Harris 2023). We therefore take two representative results from Spitler & Forbes (2009) and Dornan & Harris (2023), and show them in the first two panels of Fig. 12 by the thin and thick purple lines, respectively. For comparison, we also show results for individual galaxies obtained by Dornan & Harris (2023) using purple dots. The result produced by the model, shown by the black curve, matches the observational data well over the full range of the halo mass. This is partly because of our calibration with observations (see Appendix B), and partly because of the two underlying mechanisms in the model that shape the linearity between  $M_*^{(\text{GCs})}$  and  $M_v$ , as detailed below.

The origin of the linear relation between  $M_*^{(\text{GCs})}$  and  $M_v$  can be understood by comparing different curves in Fig. 12 produced by our model. Firstly, we note that, as shown by the green curves in the first two panels, the total stellar mass,  $M_*$ , is a non-linear function of  $M_v$  (see also observations of, e.g. Yang et al. 2012b; Behroozi et al. 2013), with  $M_*/M_v$  varying by more than 1 dex over the range of halo mass considered here. Thus, the relation between  $M_*^{(\text{GCs})}$  and  $M_*$  must be non-linear, as clearly shown by the GC frequency, defined as the number of GCs per  $10^9 M_\odot$  of the host galaxy, versus  $M_v$  in the bottom panel for galactic GCs produced by our model and obtained by Peng et al. (2008) from observational data. The frequency of Pop-II (metal-poor) GCs closely follows that of the total population, with

only small deviations above the MW mass. Pop-I is very different in that it follows the frequency of the total population only at the high end of the halo mass. The proximity of the Pop-II GCs to the total population suggests that the key to understanding the linear relation is to understand such a relation for Pop-II GCs. At  $M_v \lesssim 10^{12} M_\odot$  where the in-situ Pop-II component dominates, the condition for a halo to host a significant number of Pop-II GCs is given by Eq. (65) and shown by the blue shaded area in Fig. 8. The negative correlation between  $M_v$  and  $z$ , which defines the boundary of this condition, leads to a narrower time window for a more massive halo to host GCs. It turns out that the metal enrichment of the ISM, which is positively correlated with galaxy mass and halo mass (Fig. 3), plays an important role in blocking the Pop-II channel of GC formation in massive halos and in shaping the linear relation between  $M_*^{(\text{GCs})}$  and  $M_v$ . At  $M_v \gtrsim 10^{12} M_\odot$  where mergers become more frequent, this proportionality is preserved by the central limit theorem, as Pop-II GCs in satellite galaxies follow this linear relation and so does their summation. Thus, the origin of the observed  $M_*^{(\text{GCs})}$ - $M_v$  relation is a combination of the initial linear relation set up by the metal enrichment process and the central limit theorem that preserves it.

A similar conclusion for the importance of the central limit theorem in shaping the  $M_*^{(\text{GCs})}$ - $M_v$  relation was reached by Boylan-Kolchin (2017, see also Valenzuela et al. 2021) using a simple additive model for the formation of Pop-II GCs. In their model, an initial linear relation is assumed to populate tiny progenitor halos with GCs at  $z \approx 6$ , and the growth of a GC is followed by mass acquisition along its merger tree. Alternative explanations have also been proposed, e.g. by assuming a larger gas fraction and an enhanced GC formation rate, for halos with lower mass (e.g. Choksi et al. 2018; Choksi & Gnedin 2019; El-Badry et al. 2019; Chen & Gnedin 2022, 2023, 2024). Future observations to measure the gas fraction, density and metallicity, the reconstruction of the formation histories of GCs in low- $z$  galaxies (see e.g. Fig. 10), and to directly identify GC-forming galaxies at high  $z$  (e.g. Vanzella et al. 2022, 2023; Welch et al. 2023; Lin et al. 2023; Claeysens et al. 2023; Adamo et al. 2024; Messa et al. 2024; Fujimoto et al. 2024; Mowla et al. 2024), will be critical to distinguish different scenarios.

#### 4.5 The metallicity dichotomy

To demonstrate the relative contribution to the GC formation of the two channels, in Fig. 13 we show the metallicity distribution of galactic GCs in central galaxies with different halo masses at  $z = 0$ . The distribution for all survived GCs (black solid curve) is clearly bimodal, which is a consequence of the two channels of GC formation. For low-mass halos ( $M_v \sim 10^{11} M_\odot$ ), Pop-II GCs (blue curve) dominates the total number, while Pop-I GCs (red curve) are just starting to appear in the metal-rich end of the distribution. For MW-size halos ( $M_v \sim 10^{12} M_\odot$ ), the Pop-I channel becomes important, and the two populations are nearly equal in number. For more massive halos ( $M_v \gtrsim 10^{13} M_\odot$ ), the relative contribution from the two channels appears to be stabilized, which is an outcome of the slightly increased Pop-I GC fraction at birth (black dashed curve) due to more enriched ISM, as compared to MW-size halos, and the stronger effect of tidal disruption due to the longer time for mass loss. For all halos and for both Pop-I and Pop-II, the metallicity of GCs is significantly lower than that of the total stellar component (grey curve), which reflects the preference of GC formation in a high-density environment in the early Universe (see Eqs. 63 and 65). Such a bimodal distribution of GCs has been found by observations in nearly all galaxies, using either direct metallicity measurements



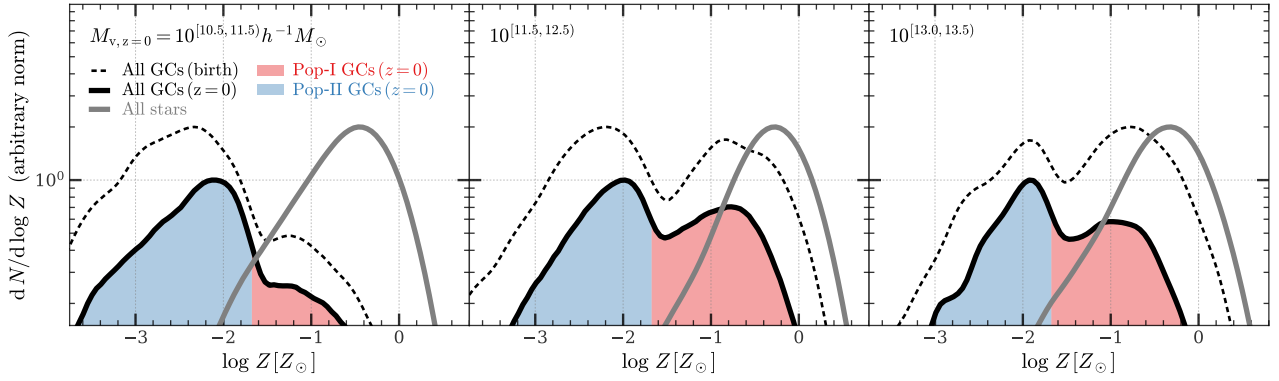


**Figure 13.** Metallicity distribution of GCs. **Three panels** show the results for GCs in central galaxies with different halo masses at  $z = 0$ . All galactic GCs (in-situ and ex-situ) are included in the analysis. **Black solid curve**, **red shade** and **blue shade** show the distributions of all, Pop-I and Pop-II GCs, respectively, survived until  $z = 0$ . **Black dashed curve** is obtained by including all GCs formed in the history. For comparison, **grey curve** shows the metallicity distribution of all stars (GC and non-GC), obtained by using all sub-clouds formed in the history, weighted by their stellar masses. Distributions are arbitrarily normalized for clarity. See §4.5 for the detailed description of this figure.

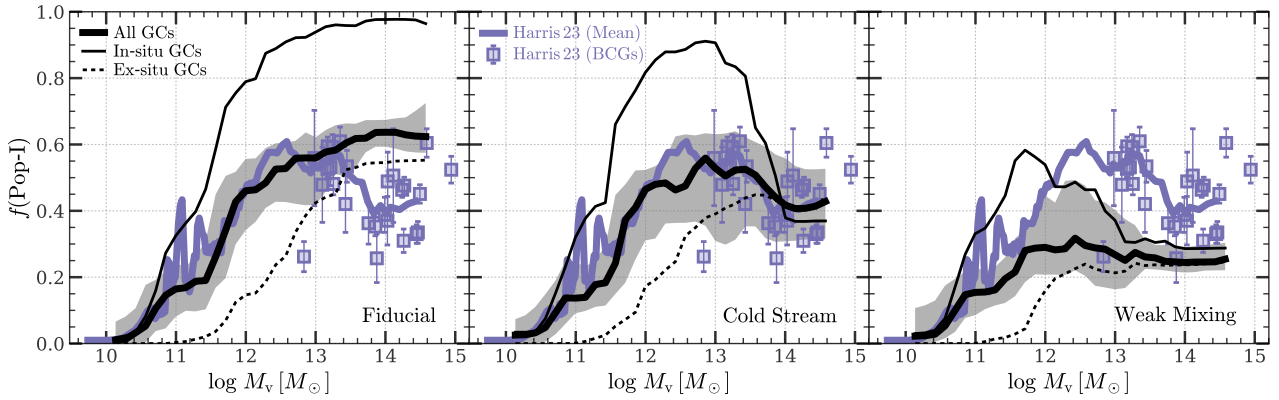


**Figure 14.** Pop-I GC fraction,  $f(\text{Pop-I})$ , as a function of halo mass at  $z \approx 0$ . **Three panels** show the results for three model variants, respectively: **left** for the fiducial, **center** for a variant that mimics the pristine inflow for stream-fed galaxies in massive halos at high redshift, and **right** for a variant with more relaxed criteria for a galaxy to be stream-fed. In all panels, **black curves** show the median results of our model: **thick** for all galactic GCs, with a shaded area indicating the  $1-\sigma$  range, and **thin** and **dotted** for the in-situ and ex-situ components, respectively. **Purple curve** is the running mean compiled by [Harris \(2023\)](#) from observations, while **purple squares** represent the results for individual brightest cluster galaxies. The observed drop of  $f(\text{Pop-I})$  at high halo mass, as our inference, is the fossils of the cold streams at high redshift. See §4.5 for details.

from spectra (e.g. [Fahrion et al. 2020a](#)), or conversion from color indices (e.g. [Harris 2023](#)).

To quantify the systematic change in the contribution of the two channels for halos with different masses, in Fig. 14, we show the fraction of Pop-I (metal-rich) GCs, defined as the number ratio between Pop-I GCs and the total galactic GCs:

$$f(\text{Pop-I}) = \frac{N_{\text{GCs}}(\text{Pop-I})}{N_{\text{GCs}}}, \quad (71)$$

as a function of halo mass. Both in-situ and ex-situ components are included in the analysis, and the results are shown for central galaxies at  $z = 0$ . Our model predicts a monotonically increasing Pop-I fraction with increasing halo mass, regardless of the parameter choices. The fiducial model (left panel, black thick curve) is calibrated by the observation of [Harris \(2023\)](#), purple curve) at  $M_v \lesssim 10^{12.5} M_\odot$  (see Appendix B), and thus matches the observation in this mass range. The Pop-I fraction is near zero at  $10^{10} M_\odot$ ; increases rapidly to about 0.5 at  $10^{12} M_\odot$ ; becomes saturated and slowly increases towards higher halo mass. This is consistent with the inferences from the effects of metal enrichment on the mass functions (§4.2), on the masses of GC systems (§4.4), and on the metallicity distributions (Fig. 13).

The reason for the dominance of Pop-II GCs at  $M_v < 10^{11} M_\odot$  can also be inferred from the GC formation criteria shown in Fig. 8, where the mass assembly histories of halos with  $M_{v,z=0} \lesssim 10^{11} M_\odot$  do not intersect with the Pop-I channel (the region covered only by red). Similar results have been obtained by, e.g. [Choksi & Gnedin \(2019\)](#), see their figure 7) and [El-Badry et al. \(2019\)](#), see their figure 9). In more detail, we separate galactic GCs into in-situ and ex-situ components, and show their Pop-I fractions separately by the thin and dotted black curves, respectively. These two components show similar monotonic behavior to the total population in the Pop-I fraction, but with different amplitude and different halo mass for saturation. This difference can be explained by the fact that progenitors of satellites in general have lower halo mass than those of centrals at a given redshift, and their metal enrichment is systematically delayed, as seen by comparing the three panels of Fig. 2.

The observational results from [Harris \(2023\)](#) cover a wide range of halo mass, with the BCGs highlighted by individual purple squares. At  $M_v \approx 10^{12.5} M_\odot$ , the observed Pop-I fraction begins to decline and drops to about 0.4 at  $10^{14} M_\odot$ , while the result of fiducial model continues to increase. This significant discrepancy can arise from



a number of sources. The first possibility is the systematic error in the observation. As many of the BCGs are quite distant, individual GCs within them are point sources even viewed by HST, and have to be distinguished from individual stars by, e.g., the color-magnitude diagram with trade-offs between completeness and contamination. The crowded environment in the inner regions of BCGs can also hide their GCs, and thus statistical inferences have to rely on the identification of the turnover point of the GC luminosity function and assumptions on the completeness curve. These systematics combined may lead to an underestimate of the Pop-I fraction in BCGs. The second possibility is the difference in the definition of Pop-I GCs between our model and the observation. The two populations in each BCG are obtained by Harris (2023) using a bi-Gaussian fitting to the distribution of the stellar [Fe/H] converted from a color index. In our model, on the other hand, the populations are classified using a physical criterion on the gas-phase oxygen abundance of the sub-clouds that host GCs (see §3.5). This difference in definition is not likely to be the main reason for the discrepancy, however, as the Pop-I fraction is related to the normalization of the two components of a bimodal distribution, rather than the metallicity of individual GCs. A linear conversion between oxygen and iron abundances for the alpha enhancement, such as that adopted by, e.g. Chen & Gnedin (2024, see their appendix), does not change the Pop-I fraction. We have also tried to use a bimodal fitting, instead of our physical criterion, to classify the two populations, and found no significant difference in the result. The final possibility is that the observed drop of the Pop-I fraction is physical and reflects a deficiency of our model, as we discuss in the following.

One simplification of our model, as discussed in §3.4 of Paper-I, is the assumption of spherically symmetric accretion of gas into the SGC. Galaxies in the real Universe, however, can be fed by filamentary inflows of cold streams. The thin, cold streams of pristine gas are expected to penetrate the IGM, with only little mixing with the enriched outflow (see e.g. an analytical estimation by Li et al. 2024). High resolution numerical simulations (e.g. Mandelker et al. 2018) suggest that dense clumps can form within such streams, leading to even less mixing with the enriched gas. Thus, stream-fed galaxies may have a higher fraction of Pop-II GCs originated from cold-stream inflows. To test the effects of such accretion on GC formation, we design a suite of variants to the fiducial model by lowering the metallicity of sub-clouds in stream-fed galaxies. Formally, we define a galaxy to be stream-fed when it is in the fast phase of halo accretion, and if

$$\eta_s(M_v, z) \equiv \frac{M_v}{10^{10.8} M_\odot} \left( \frac{1+z}{10} \right)^{6.2} \geq \eta_{s,0}, \quad (72)$$

where  $\eta_{s,0}$  is a free-parameter. The requirement for fast accretion is motivated by hydrodynamic simulations, which found that cold gas streams are seeded by dark matter filaments outside the virial radius of fast-accreting halos (e.g. Danovich et al. 2015). The parameterization of  $\eta_s$  is derived by Dekel et al. (2023) to identify galaxies that are ‘feedback-free’, and is used by Li et al. (2024) to model ‘feedback-free’ galaxies. From their arguments, a galaxy with  $\eta_s \geq 1$  is purely fed by cold streams, and a lower value of  $\eta_s$  leads to a galaxy with more spherical accretion. For a stream-fed galaxy, we lower the metallicity of each sub-cloud by randomly assigning it a metallicity,  $Z_{sc}$ , drawn from the distribution

$$\frac{dN_{sc}}{dZ_{sc}} \propto Z_{sc}^{\beta_{sc,Z}}, \quad (73)$$

in the range of  $Z_{sc} \leq Z$ , where  $Z$  is the metallicity of the SGC predicted by the fiducial model (§2.4), and  $\beta_{sc,Z}$  is a free-parameter.

With this modification, we define two variants as follows. The first one, referred to as the ‘Cold Stream’ variant, has  $\eta_{s,0} = 0.2$  and  $\beta_{sc,Z} = -0.35$ . This variant is obtained on the basis of the fiducial model whose calibration is presented in Appendix B, with additional tuning of  $\eta_{s,0}$  and  $\beta_{sc,Z}$  so that the Pop-I fraction matches those of the BCGs at  $M_v \geq 10^{12.5} M_\odot$  obtained by Harris (2023). The second variant, referred to as the ‘Weak Mixing’ variant, has  $\eta_{s,0} = 0.02$ , a more relaxed criterion for a galaxy to be stream-fed, and the same value of  $\beta_{sc,Z}$  as the first variant. The results of these two variants for the Pop-I GC fraction are shown in the central and right panels of Fig. 14, respectively. The ‘Cold Stream’ variant appears to match the observations well owing to parameter tuning. An inspection of  $f(\text{Pop-I})$  for the in-situ and ex-situ components suggests that cold streams mainly affect the in-situ formation in massive halos, which is a consequence of the mass and redshift dependence of  $\eta_s$ . The ‘Weak Mixing’ variant, on the other hand, produces too many metal-poor sub-clouds in low-mass halos, and thus under-predicts the Pop-I fraction in most halos.

Given the small sample size and the large uncertainty in identifying  $f(\text{Pop-I})$  GCs from individual BCGs, it is still premature to make definite conclusions on the origin of the observed drop of the Pop-I fraction at high halo mass. Observations of GCs at higher redshift, such as those made by JWST at  $z \approx 0.3$  (Harris 2023; Harris & Reina-Campos 2024), or at even higher redshift via strong lensing (Vanzella et al. 2022, 2023; Welch et al. 2023; Lin et al. 2023; Claeysens et al. 2023; Adamo et al. 2024; Messa et al. 2024; Fujimoto et al. 2024; Mowla et al. 2024), will provide more clues. Gas dynamics and metallicity measured via multiple tracers (e.g. Wang et al. 2019, 2022; Zhang et al. 2023; Lin et al. 2023; Venturi et al. 2024) have unveiled from a small number of systems that pristine gas inflows can invert the radial gradient of the metallicity profile. A larger sample of such measurements is needed to quantify the importance of the stream-fed population of galaxies.

## 4.6 Spatial distribution

Complementary to the age distribution (§4.2) that describes when GCs formed, the spatial distribution of GCs in their host galaxies and halos contains information about their birthplaces and provides additional insights into the conditions and mechanisms of GC formation. In observations, this information can be obtained as long as resolved images are available. To predict the spatial distribution from the first principle is more challenging, as it requires precise modeling of the host environment, including small-scale perturbations from close encounters of density clumps, and precisely tracking the orbits of individual GCs. One approach is to attach each newly formed star cluster to a neighbor young stellar particle that serves as an environment tracer (e.g. Pfeffer et al. 2018; Chen & Gnedin 2022; Rodriguez et al. 2023). This approach, however, can only be applied to the ‘post-processing’ models based on high-resolution hydrodynamical simulations, because it needs stellar particles to trace the orbits. Such details are not available in the large-volume, dark-matter-only simulations used here. Meanwhile, the tracer-based method cannot deal with dynamical friction and orbital decay of star clusters in a self-consistent way, and analytical approximations are still necessary.

Here we adopt a semi-empirical approach to assign a spatial location to each modeled star cluster, with the formulation and parameters motivated physically and calibrated by observations. We note that the purpose here is to statistically reproduce the profile of GCs in their host galaxies at a given redshift, instead of tracking the evolution of individual orbits. For each galaxy at the given redshift  $z$ , we partition

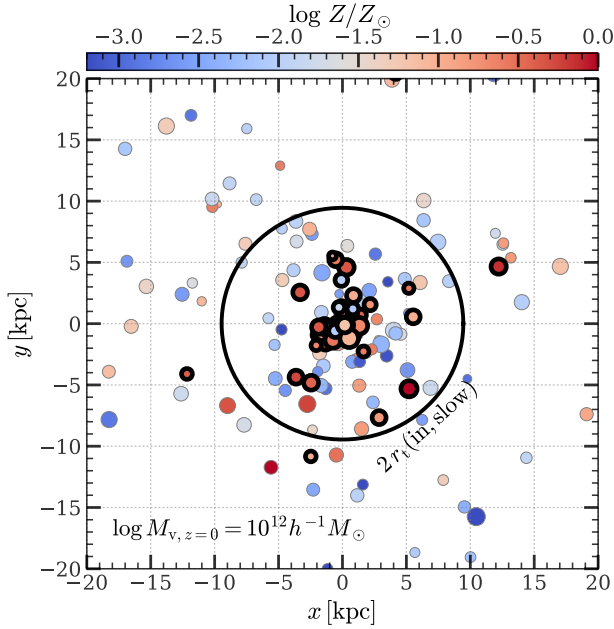


**Figure 15.** Projected spatial distribution of GCs within a MW-size galaxy with  $M_v = 10^{12} h^{-1} M_\odot$  at  $z = 0$ . All galactic GCs predicted by our model and resampled with the BSAMPLING method (see §4.1) are shown. Each **dot** represents a survived GC, with **bold** and **thin** edges indicating their in-situ and ex-situ origins, respectively. The **size** of each circle is proportional to  $R_{\text{cls}}$ , the half-mass radius of the GC (see §3.4). Metallicity of each GC is **color-coded** according to the color bar on the top. The **big circle** indicates two times the exponential truncation radius of the in-situ, slow-phase GC system of this galaxy. See §4.6 for a detailed discussion of this figure.

its survived GCs into three components: (A) the in-situ component formed during the fast phase; (B) the in-situ component formed during the slow phase; (C) the ex-situ component accreted from merged companion galaxies. A GC is assigned a galactocentric distance,  $r$ , according to the number density profile

$$n(r) \propto \frac{1}{r^2} \exp\left(-\frac{r}{r_t}\right), \quad (74)$$

where GCs belonging to the same component share a common parameter  $r_t$  that describes the characteristic size of the distribution of the GC component. The isothermal form,  $1/r^2$ , is motivated by the expectation that the fragmentation of an SGC is associated with effective cooling that keeps the temperature to be  $10^4$  K at the formation of dense sub-clouds (§3.1). The exponential truncation ensures that the distribution of galactic GCs has a finite extent. Once  $r$  is sampled for a GC, the angular location is randomly drawn from a uniform distribution on a unit sphere.

The typical value of  $r_t$  for each of the three components can be obtained by assuming that GCs follow the profile of diffuse stellar components. For the in-situ GC system formed during the fast-phase, its characteristic size is expected to be the size of the stellar bulge, which is discussed in Paper-II and can be modeled to be about  $0.01 R_f$ , where  $R_f$  is the halo virial radius at the end of the fast phase. We thus set  $r_t^{(\text{in,fast})} = 0.01 R_f$  as our fiducial choice. For the in-situ GC system formed during the slow phase, its size is expected to be the size of the stellar disk, which is derived theoretically by, e.g. Fall & Efstathiou (1980), Fall (1983) and Mo et al. (1998), and observed to be about  $0.02 R_v$  with a moderate uncertainty (e.g. Kravtsov 2013; Huang et al. 2017; Somerville et al. 2018). We thus set  $r_t^{(\text{in,slow})} = 0.02 R_v$  as our

fiducial choice. The size of the ex-situ GC system is theoretically uncertain due to the complexity of tidal stripping and galaxy mergers. The typical value found by observations is about  $0.1\text{--}0.2 R_v$  (e.g. Kartha et al. 2014; Alabi et al. 2016; Forbes & Remus 2018; Dornan & Harris 2023), from which we choose a conservative value of  $r_t^{(\text{ex})} = 0.1 R_v$ , as suggested by Dornan & Harris (2023).

Another difference between the three components is their dynamical hotness (see Paper-I). GCs formed during the fast phase or assembled via mergers are expected to follow random orbits, as dissipation is not sufficient to settle them down into a dynamically cold disk. Thus, we randomly sample the galactocentric distance from the distribution of Eq. (74). In-situ GCs formed during the slow phase live in the dynamically cold disk, and are expected to preserve their orbits over a long time. We thus assume that their orbits are the same as those used in modeling the tidal disruption, which is achieved by taking the  $u_r$  value sampled for Eq. (67) as the percentile value, and inverse the CDF of Eq. (74) to get the quantile value.

Fig. 15 shows the spatial distribution of GCs in an example of Milky Way-size galaxies at  $z = 0$ . Here, we take the survived GCs together with their BSAMPLING weights from the model output, and resample them to get a set of un-weighted GCs for display (see §4.1). Each of the un-weighted GCs is shown by a circle, with the color representing the metallicity and the size proportional to the half-mass radius of the GC (see §3.4). The in-situ population (highlighted by bold edges) has a smaller spatial extent than the ex-situ one, owing to the difference in their  $r_t$ . Ex-situ GCs are on average bluer, reflecting the less enriched ISM of their hosts at formation (see also §4.5 and Fig. 14). The sizes of in-situ GCs are also bigger, which is a consequence of the higher amplitude of the size-mass relation for Pop-I GCs (Fig. 11) and the similar mass function of both Pop-I and Pop-II GCs (Fig. 9).

Upper panels of Fig. 16 shows the number density profiles of GCs in central galaxies with different halo masses at  $z = 0$ . For the profile of all survived GCs (black solid curve), the amplitude increases rapidly with halo mass, as a result of the tight, linear relation between  $M_*^{(\text{GCs})}$  and  $M_v$  described in §4.4. In contrast, the shape of the profile is independent of halo mass, which is a consequence of our model to assign positions to GCs (see Eq. 74). Such a universal profile has been found in observations, and has been modeled using the Sérsic profile (Usher et al. 2013; Kartha et al. 2014; Hudson & Robison 2018), the modified Hubble profile (Caso et al. 2019; De Bortoli et al. 2022; Caso et al. 2024), and the power-law profile (Hudson & Robison 2018). The profile shows some flattening in the inner region, which is due to the tidal disruption of the in-situ component in the slow halo assembly phase (see §3.6). The disruption changes the profile of the GC distribution, reduces its amplitude and makes its shape less concentrated, in comparison with the profile of all GCs selected at their formation (black dashed curve). As disrupted GCs can contribute to the diffuse stellar component, a part of the metal-poor and alpha-enhanced stellar population observed in the Milky Way may have originated from the disrupted GCs (Wallerstein 1962; Weinberg et al. 2019; Rojas-Arriagada et al. 2019; Lian et al. 2020). Separated into Pop-I and Pop-II populations, the profile of Pop-I (red curve) is more centrally concentrated than that of the Pop-II (blue curve), which owes to the extension of the profile caused by metal-poor GCs brought in by mergers. This prediction is consistent with the observed negative metallicity gradient of GCs in most galaxies (e.g. Usher et al. 2013; Fahrion et al. 2020b; Harikane et al. 2023). The outer profiles ( $r \sim 100$  kpc) for both Pop-I and Pop-II GCs in massive galaxies (right panel) are very similar, indicating a flat

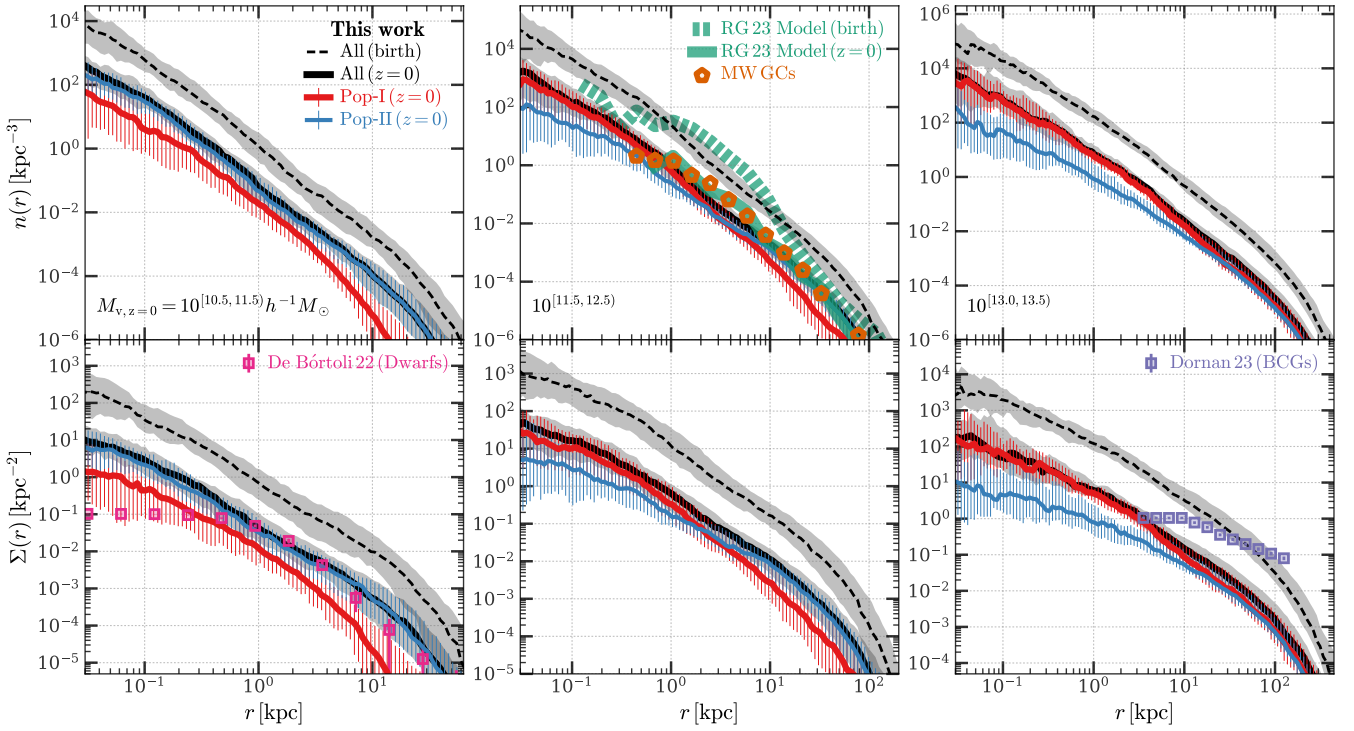


**Figure 16.** **Upper row:** number density profile of galactic GCs. **Lower row:** surface number density profile of galactic GCs. **Three columns** show the results for central galaxies with different halo masses at  $z = 0$ . Both in-situ and ex-situ components are included. In each panel, **solid black, red and blue** curves are for all, Pop-I and Pop-II GCs, respectively, all including only survived GCs. **Dashed black** curve includes all GCs at formation (see §4.1 for the selection). Each curve shows the median of GC systems, with error bars or shaded areas indicating the  $1-\sigma$  range. **Green** curves are obtained by Rodriguez et al. (2023) using the model of GC formation developed by Grudić et al. (2023) and a star-by-star model of cluster evolution, applied to a MW-size galaxy in the FIRE-2 simulation. The solid and dashed curves include their GCs at birth and survived at  $z = 0$ , respectively. **Orange** markers are obtained by their compilation of MW GCs based on the catalog of Harris (1996, 2010 edition). **Pink** markers are staked results for 7 sets of dwarf galaxies, taken from the observations by De Bortoli et al. (2022, including those obtained earlier by Caso et al. 2019). **Purple** markers are stacked results for 4 BCGs, taken from the observations by Dornan & Harris (2023). See §4.6 for a detailed discussion of this figure.

metallicity gradient in the outskirts of massive galaxies. This is indeed seen in the BCG sample of Harris (2023, see their figure 24).

The orange symbols in the upper-center panel of Fig. 16 show the number density profile of GCs in the Milky Way, obtained from the data compiled by Rodriguez et al. (2023) using the catalog of Harris (1996, 2010). Our prediction for the profile of Milky Way-size galaxies is in agreement with the observation. A noticeable difference is seen around  $r = 5$  kpc, roughly the peak position of the number distribution,  $dN_{\text{GC}}/dr$  (see e.g. figure 10 of Rodriguez et al. 2023). This radial range turns out to be the joint region of the in-situ and ex-situ components, where the interaction between infalling satellites and the central galaxy is expected to be strong. The less relaxed orbits of the GCs stripped from the satellites, and the perturbed orbits of GCs in the central, may not be described well by the simple superposition assumed in our model. Other uncertainties may come from the scatter in  $r_t$  for a given halo mass, which can change the radial distribution of GCs systematically. Such scatter may be caused by variances in both the assembly history and structure among individual halos of a given mass (Liang et al. 2024a), or by baryonic processes that can modify the dynamics of the galaxy (El-Badry et al. 2016; Jiang et al. 2019; Hopkins et al. 2023). Towards the innermost region, the observed profile for the Milky Way GCs is truncated at  $r \approx 0.5$  kpc, while that predicted by our model continues to rise. As the observed number of Milky Way GCs in the innermost bin is very small, Poisson noise dominates the observational result. Our prediction, which is obtained by averaging over a large sample

of galaxies, gives a robust estimate of the inner profile. The predicted larger scatter in the inner region, as represented by the shaded areas and error bars, is caused by sampling error.

The square markers in the lower panels of Fig. 16 show the surface number density profiles of GCs in dwarf galaxies and BCGs, obtained by staking the observations of De Bortoli et al. (2022, including those obtained earlier by Caso et al. 2019) and Dornan & Harris (2023), respectively, in comparison with our model prediction in the same ranges of halo mass. The error bars here are obtained by randomly sampling the profiles, taking into account uncertainties of their fitting parameters. For BCGs, we follow the Appendix of Dornan & Harris (2023) to correct the number of GCs fainter than the detection limit by assuming a Gaussian distribution for the magnitudes of GCs. The inner profile of observed dwarfs is flatter at  $r \lesssim 1$  kpc than the model. Part of such discrepancy may come from the uncertainty in the correction of incomplete detection, while the rest, as suggested by Caso et al. (2019), can be physically caused by the efficient tidal disruption of GCs in inner regions of galaxies (see also Bílek et al. 2019, 2024, for an interpretation with alternative gravity model). The observed GCs around BCGs have an outer profile  $\Sigma \sim r^{-1}$ , much shallower than the model prediction. Such a profile indicates that the integration of the GC number over radius is divergent, so that a significant contribution can come from GCs in the intracluster space due to projection. In both cases, it is unknown whether or not the simple assumption of a truncated isothermal profile in our model (Eq. 74) can capture the variation with halo mass. A forward model-



ing with precise recipes for GC orbits and disruption (e.g. [Vital & Boldrini 2022](#); [Ferrone et al. 2023](#)) within realistic galactic environments is needed to make accurate model-observation comparison. This can be achieved by embedding GC-formation and evolution models in cosmological/zoom-in simulations (e.g. [Rodriguez et al. 2023](#)), or by parametric methods with calibrations using simulations and observations (e.g. [Liang et al. 2024b](#)).

#### 4.7 Globular clusters in the cosmological hierarchy

The key aspect of our model is its ability to efficiently populate halos with GCs on cosmological scales. Fig. 1 shows the two-point correlations of GC populations,  $\xi_{gc,gc}$ , obtained from the GC catalog in the full box of TNG100-1-Dark. The correlation functions cover a large range of spatial scales, from the scale of cosmic web ( $\gtrsim 1$  Mpc, as indicated by the size of Coma cluster,  $R_{200c,Coma}$ ), to the scale of a sub-cloud ( $\lesssim 10$  pc, as indicated by the typical size of sub-clouds,  $R_{sc}$ ), from the regime dominated by dark matter, to the one dominated by baryons. Thus, the GC-GC correlation functions encode rich information about structure formation at different scales and throughout the cosmic history, and can potentially serve as powerful summary statistics to constrain models of galaxy formation, especially subgrid assumptions in hydrodynamic simulations (see e.g. [Li et al. 2020](#)).

Following the terminology of the halo occupation distribution model (e.g. [Jing et al. 1998](#); [Berlind & Weinberg 2002](#); [Guo et al. 2015, 2016](#); [Yuan et al. 2022](#); [Qin et al. 2022](#)), we can partition the GC-GC correlation function by characteristic scales in the structure hierarchy: a ‘two-halo’ term that represents the cross-correlation of GCs in different halos; a ‘one-halo’ term or ‘two-galaxy’ term that represents the correlation of GCs between two galaxies within a single halo; a ‘one-galaxy’ term that represents the auto-correlation of GCs within one galaxy.

The grey squares in Fig. 1 show  $\xi_{g,g}$ , the galaxy-galaxy correlation functions obtained by [Shi et al. \(2016\)](#) for galaxies of different luminosities. These correlation functions have been corrected for the redshift-space distortion, and thus approximate the real-space distribution of galaxies. Our  $\xi_{gc,gc}$  for the whole sample of GCs (black curve) tightly follows the  $\xi_{g,g}$  of galaxies, and shows a clear separation between the two-halo and one-halo terms at sub Mpc scales. These indicate that the large-scale spatial distribution of GCs reflects the large-scale dark matter distribution. The orange plus symbols in Fig. 1 show  $\xi_{g,gc}$ , the galaxy-GC cross-correlation function obtained by using the Milky Way GC profile shown in Fig. 16. This function extends the spatial coverage from the halo scale to the galaxy scale, as indicated by  $R_{e,GCS}$  and  $R_{80,galaxy}$ . The  $\xi_{gc,gc}$  for all GCs is significantly different from that of the Milky Way,  $\xi_{g,gc}$ , indicating that Milky Way-size galaxies are not the dominant hosts of GCs in the Universe. This is in contrast to the total stellar population, for which Milky Way-size halos dominate the stellar mass throughout almost the entire cosmic history (see e.g. figure 16 and §5.4 of [Paper-I](#)). One reason for this is clearly shown in Fig. 10 and discussed in §4.2, where the cosmic GC formation is found to peak at  $z \approx 5$ , much earlier than that of the overall stellar population, and in Fig. 12 and §4.4, where the GC occupation frequency is found to be the lowest at about Milky Way mass. At  $r \lesssim 1$  kpc, only a small number of GCs were found by observations in the MW, and they are even more difficult to find in extra-galactic systems due to the crowded environment. The recent discovery of GCs by Gaia in the bulge of MW ([Palma et al. 2019](#); [Minniti et al. 2021](#)) provides a new opportunity to extend the radial distribution of GCs to the core of the Galaxy, and to test the GC-GC correlation function predicted by our model. An-

other common approach is to use the projected correlation function, which is measurable in more distant galaxies. Observations targeting at dwarf galaxies, especially the (ultra-)diffuse dwarfs (e.g. [Janssens et al. 2022](#); [Forbes & Gannon 2024](#); [Jones et al. 2023](#)), may also help us avoid the crowded environment, and extend the GC clustering measurement to smaller scales.

The red and blue curves in Fig. 1 show the GC-GC correlation function for Pop-I and Pop-II GCs, respectively. The correlation function of Pop-II GCs closely follows that of all GCs at all scales, indicating that Pop-II GCs dominate the GC population. At the two-halo scale, the correlation function of both populations are similar to that of all GCs, indicating that the cosmic large-scale environment plays a secondary role in GC formation once the halo-scale environment is fixed. At and below the halo scale, the correlation function of Pop-II GCs appears to be in two parts, separated at the scale of 1–5 kpc, coincident with the core radius,  $R_{core,CGS}$ , found by [Caso et al. \(2019\)](#), [De Bortoli et al. \(2022\)](#) and [Caso et al. \(2024\)](#) when fitting the spatial distribution of GCs. This characteristic scale is the transition scale from the ‘two-galaxy’ term to the ‘one-galaxy’ term, and marks the change of the dominating GC population from the ex-situ origin to the in-situ origin. On the other hand, Pop-I GCs are more frequently produced in massive galaxies, as shown in Fig. 12 and Fig. 14, and thus are concentrated in the central galaxies of dark matter halos. Consequently, the correlation function of Pop-I GCs falls below that of Pop-II GCs at the two-galaxy scale, rises rapidly, and becomes higher than that of Pop-II GCs at the one-galaxy scale. The crossing point between the Pop-I and Pop-II correlation functions is at about  $R_{80,galaxy}$ , the observed boundaries of galaxies at or above the Milky Way mass (see [Mowla et al. 2019](#)), indicating the dominance of Pop-I GCs in galaxies more massive than the Milky Way (see Fig. 14).

The information encoded in  $\xi_{g,g}$  complements the clustering analysis based only on galaxies, and can be used to extend the test of structure formation to small scales and early times. The physical processes in the early Universe involved in the formation of GCs, such as the fragmentation of SGC into sub-clouds, the compression of sub-clouds by supersonic shocks, and the contraction of sub-clouds due to the slow cooling of metal-poor gas (marked by the green arrows in Fig. 1; see §3 for details), are expected to make imprints on these compact stellar systems, and may be retrieved from observations in the local Universe.

#### 4.8 Globular clusters at high redshift

The observation of GCs usually requires high spatial resolution so that GCs can be separated from other point(-like) sources. This is typically feasible only at low redshift, and becomes challenging at high redshift as the angular sizes involved are small. However, under certain conditions, GCs can be observed at high redshift. One promising way is to rely on gravitational strong lensing, which can magnify and stretch background images, making small sources observable and spatially distinguishable. Such observations have indeed carried out for a number of young and massive star clusters with sizes comparable to those of GCs up to  $z \approx 10$  (e.g. [Vanzella et al. 2022, 2023](#); [Welch et al. 2023](#); [Lin et al. 2023](#); [Claeyssens et al. 2023](#); [Adamo et al. 2024](#); [Messa et al. 2024](#); [Fujimoto et al. 2024](#); [Mowla et al. 2024](#); [Whitaker et al. 2025](#)). The detectability of GCs can probably be enhanced further if the initial mass function (IMF) relevant for high- $z$  GCs is top-heavy, as suggested by some theoretical studies ([Larson 1998](#); [Raiter et al. 2010](#); [Marks et al. 2012](#); [Haghi et al. 2020](#); [Chon et al. 2021](#); [Sharda & Krumholz 2022](#)) and hinted by some analyses based on observations ([Zaritsky et al. 2014](#); [Zhang et al. 2018](#); [Tang](#)



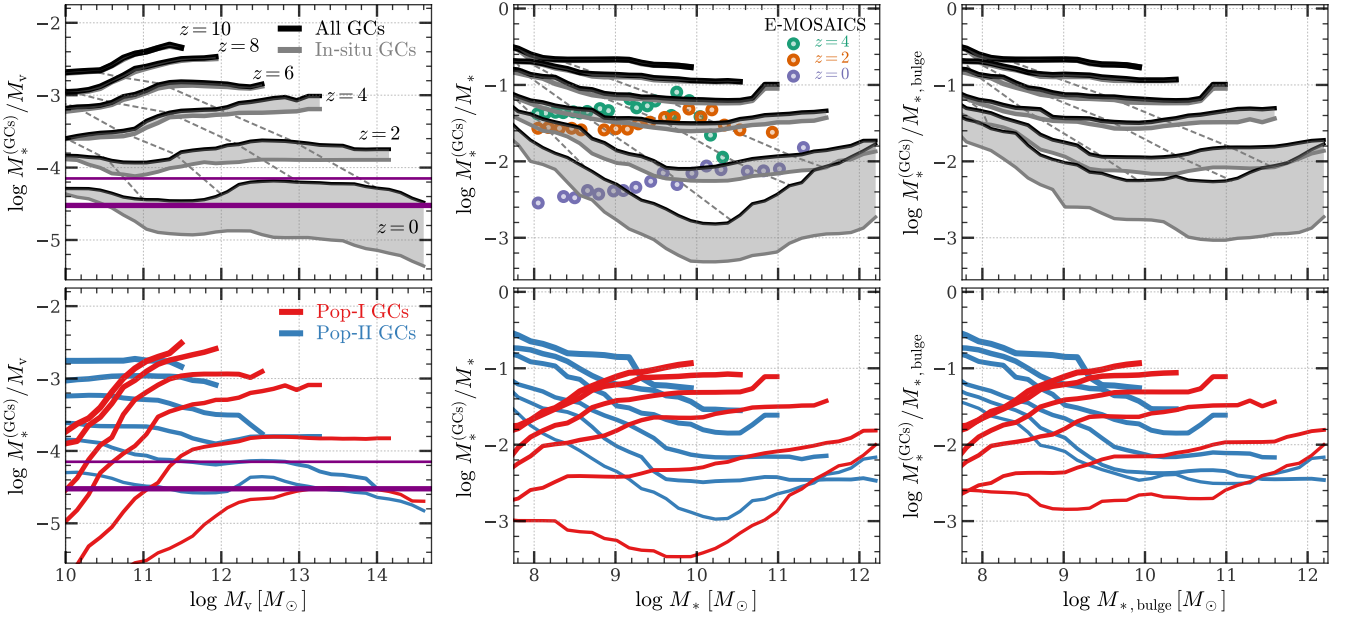


**Figure 17.** GCs mass to host mass relation, as represented by the ratio of total mass of GCs ( $M_*^{(\text{GCs})}$ ) and a host mass (halo mass  $M_v$ , stellar mass  $M_*$ , or bulge stellar mass  $M_{*,\text{bulge}}$ ) as a function of the host mass. Curves of the same color, from top to bottom, and from thick to thin, show the results for central galaxies from  $z = 10$  to  $0$ , as indicated in the first panel. All galactic GCs (in-situ and ex-situ) are included in the analysis. **Upper row** shows the results for all galactic GCs (**black curve**) and the in-situ component (**grey solid curve**). **Grey dashed** curves show the median evolution paths in the panel for the main branches of halos with given masses at  $z = 0$ , from  $M_{v,z=0} = 10^{11} M_\odot$  to  $10^{14} M_\odot$ . **Lower row** shows the results for the Pop-I (**red curve**) and Pop-II GCs (**blue curve**). **Purple lines** in the first column indicate the fittings of observations, as described in Fig. 12 and §4.4. In the upper center panel, we also show the results obtained by Bastian et al. (2020, see their figure 4) from the E-MOSAICS model at three redshifts. See §4.8 for a detailed discussion of this figure.

et al. 2021; Dib et al. 2022; Upadhyaya et al. 2024). Here we make some predictions for the GC population at high redshift, and provide some guidance for future observations.

#### 4.8.1 Connection to host galaxies and halos

Fig. 17 shows the GCs mass to host mass relation for central galaxies at various redshifts from  $z = 10$  to  $z = 0$ . Here, the mass of GCs,  $M_*^{(\text{GCs})}$ , includes all galactic GCs (in-situ and ex-situ). The host masses shown in different columns are halo mass ( $M_v$ ), galaxy stellar mass ( $M_*$ ), and galaxy bulge stellar mass ( $M_{*,\text{bulge}}$ ), respectively. The predicted total mass of Pop-II (blue) GCs is nearly a constant fraction of the host halo mass for halos with  $M_v \lesssim 10^{10.5} M_\odot$  at any given redshift (lower left panel). The value of this fraction, however, depends strongly on redshift, decreasing from  $\sim 10^{-2.8}$  at  $z = 10$  to about  $10^{-4.4}$  at  $z = 0$ . In contrast, the total mass of Pop-I (red) GCs increases with  $M_v$  in this range of halo mass, although the redshift dependence is similar to that of Pop-II. The redshift dependence of both populations is mainly driven by the evolution of the SGC density, as shown in §3.1, while the difference between the two populations reflects the increase of metal enrichment of the host galaxy with time (see Fig. 3). At  $M_v \gtrsim 10^{10.5} M_\odot$ , the formation of in-situ Pop-II GCs becomes inefficient due to the enriched ISM, but the ex-situ component brought in by mergers drives the total Pop-II GC mass back to the linear relation with the host halo mass at  $z \lesssim 4$ . This is the same conclusion reached in §4.4 from the halo mass dependence of different GC populations at  $z = 0$  shown in Fig. 12. As the central limit theorem also applies to Pop-I GCs, their total mass in a halo also follows the linear relation with the halo mass in massive halos at low redshift. The behavior of  $M_*^{(\text{GCs})}$  of all GCs, as shown in the upper left panel, is a combination of the two populations, with

the amplitude in the  $M_*^{(\text{GCs})} - M_v$  relation decreases rapidly with decreasing redshift.

The second column of Fig. 17 shows the relation of the total mass of GCs to the stellar mass of the host galaxy (GC + non-GC). Interestingly, the total mass of all GCs,  $M_*^{(\text{GCs})}$  shown by black curves, is proportional to  $M_*$  at  $z \gtrsim 4$ . At lower  $z$ , the decrease of  $M_*^{(\text{GCs})}/M_*$  with decreasing redshift appears to be the fastest at around the Milky Way mass, producing a non-linear relation between the two masses. A separation of  $M_*^{(\text{GCs})}$  into contributions from Pop-I (red) and Pop-II (blue), plotted in the lower middle panel, shows that the linear  $M_*^{(\text{GCs})} - M_*$  relation at high  $z$  seen in the upper middle panel originates from the balance between the two formation channels in halos of different masses (see Fig. 8). A more quantitative analysis can be made using  $n_{\text{sgc}} \mathcal{M}_2^2$  given by Eq. (41). As shown there, the high-density tail of the sub-cloud distribution depends only weakly on halo mass (via  $f_{\text{gas}}$  and  $f_{\text{str}}$ ) in the SN-driven regime, and so the fraction of stellar mass in GCs depends strongly only on the redshift. At lower redshift, however, two channels diverge, with the Milky Way mass falling in the gap between the two channels (shown by the blank region of Fig. 8). For comparison, we show the results of Bastian et al. (2020) as symbols in the upper-center panel. Quite different to our results, the linear relation between  $M_*^{(\text{GCs})}$  and  $M_*$  in their results extends to  $z = 0$ . They argued that this linear relation is more physical than that between  $M_*^{(\text{GCs})}$  and  $M_v$ . Since the largest difference between the predictions is at  $z \sim 0$ , the two models can be distinguished by measuring  $M_*^{(\text{GCs})}$  in galaxies with  $M_*$  between  $10^9$  and  $10^{11} M_\odot$ . The third column of Fig. 17 is similar to the second column, but with  $M_*$  replaced by  $M_{*,\text{bulge}}$ , the bulge mass of galaxies. Since the bulge of a galaxy typically represents the dynamically hot stellar component of the galaxy, its mass may be more closely related to  $M_*^{(\text{GCs})}$ , as both are affected by early violent collapse of the halo

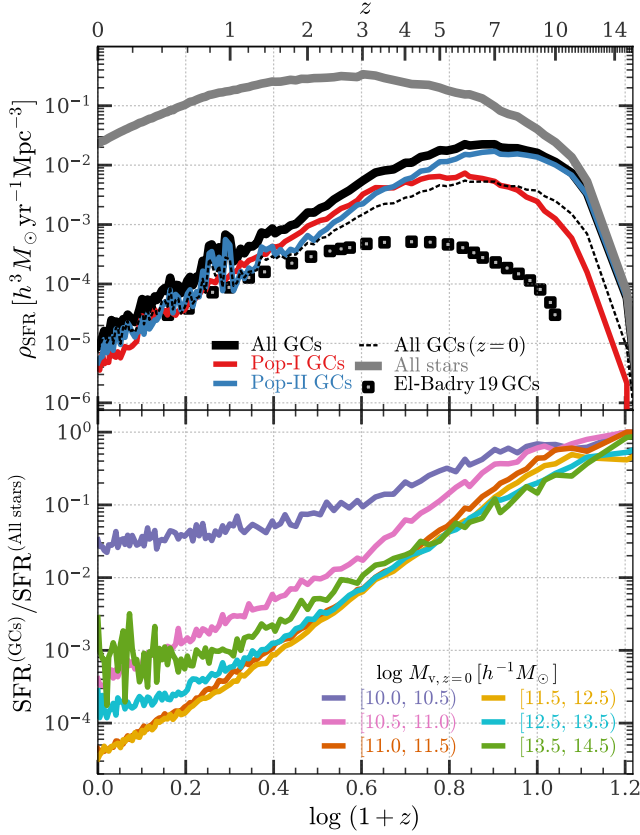


**Figure 18.** Cosmic GC formation history. **Upper panel** shows the cosmic star formation rate density  $\rho_{\text{SFR}}$  obtained by subhalo merger trees rooted in all (central and satellite) subhalos residing in halo with  $M_{v,z=0} \geq 10^{10} h^{-1} M_{\odot}$ . **Black solid, red and blue** curves show  $\rho_{\text{SFR}}$  contributed by all, Pop-I and Pop-II GCs, respectively, all selected and evaluated according to their birth-time properties (see §4.1 for the selection). For comparison, **black dashed** curve is obtained by only counting the retained mass of GCs survived until  $z = 0$  (see §3.6 for the dynamical evolution). **Grey** curve accounts for all stars (GC and non-GC). **Square** markers show the fiducial results obtained by El-Badry et al. (2019, see their figure 8) using a semi-analytic model. **Lower panel** shows the ratio of in-situ star formation rate contributed by GCs and that by all stars in the main branches of central galaxies with different halo masses at  $z = 0$ . This figure suggests that a significant fraction of stars in the early Universe is formed in GCs. See §4.8 for a detailed discussion of this figure.

and major mergers experienced by the host galaxy. This is indeed seen in the right column, where the mass ratios at  $z \lesssim 2$  become much flatter for galaxies with  $M_* > 10^{10} M_{\odot}$  and for the total, Pop-I and Pop-II populations.

For reference, the grey dashed curves in the upper row of Fig. 17 show the median evolution paths for the main branches of central sub-halos of different masses at  $z = 0$ . These are obtained by using the DIFFMAH library (Hearin et al. 2021) to generate main-branch halo mass assembly histories, and using the fittings of our model predictions to map halo histories to different stellar masses of galaxies. The meshes built in this way provide a data cube, so that one can start with a given mass  $M_*$  which can be  $M_v$ ,  $M_*$  or  $M_{*,\text{bulge}}$ , and build the expected evolution history of the halo/stellar/GC mass components of the galaxy over the entire cosmic history.

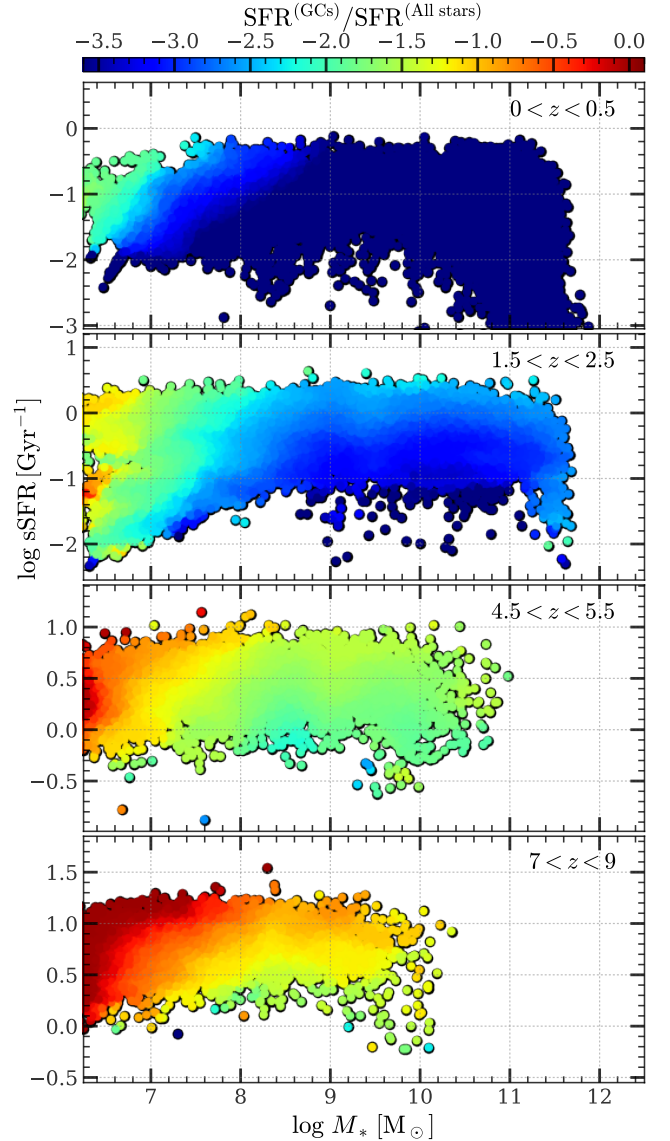


**Figure 19.** Fraction of in-situ star formation rate contributed by GCs, color-coded according to the color bar, as a function of galaxy stellar mass and specific star formation rate (sSFR). Four panels include galaxies within different ranges of redshift, and each dot represents a galaxy. See §4.8 for details.

#### 4.8.2 The cosmic formation history of globular clusters

Our results suggest that GCs are preferentially formed at high redshift. It is thus interesting to see how GCs contribute to the cosmic star formation history of the universe. The top panel of Fig. 18 shows  $\rho_{\text{SFR}}^{(\text{GCs})}$ , defined as the total mass density of stars formed in GCs per unit time. The peak of the SFR density from GCs (black curve) is peaked at  $z \approx 6-7$ , significantly earlier than that of the cosmic star formation rate density of all stars (grey curve). This is consistent with the expectation that the average  $n_{\text{sgc}}$  (see Eq. 8), and thus the formation rate of GCs (see §3.5), is higher at higher  $z$ . Separating  $\rho_{\text{SFR}}^{(\text{GCs})}$  into contributions from the Pop-I and Pop-II channels, we find that the Pop-II channel dominates the formation at  $z \gtrsim 4$ , and becomes equally important as Pop-I at lower redshift. The black dashed curve shows the cosmic SFR density obtained by accounting only for GCs that survive to  $z = 0$  and by using only their retained stellar mass in

the evaluation of  $\rho_{\text{SFR}}^{(\text{GCs})}$ . This curve is significantly lower than the black solid curve at  $z \gtrsim 1$ , consistent with the disruption timescales estimated in §3.6. The results shown here is broadly consistent with the age distribution of GCs in  $z = 0$  galaxies, as shown in Fig. 10 and discussed in §4.2. The squares show the prediction of El-Badry et al. (2019) using their semi-analytic model with fiducial parameters. The  $\rho_{\text{SFR}}^{(\text{GCs})}$  predicted by their model follows the total cosmic star formation history that peaks at a lower redshift than that predicted by our model, because of the tight relation between GC formation and star formation in host galaxies assumed in their model. The difference between our model and theirs is partly due to the enhanced formation efficiency of Pop-II GCs in the metal-poor ISM in our model (see §3.5), and partly due to their assumption that the formation rate of GCs scales with the average gas surface density of the host galaxy (see their §2.2).

The lower panel of Fig. 18 shows the fraction of stars formed in GCs throughout the star formation histories of galaxies in halos of different masses at  $z = 0$ . Here, the total star formation rate,  $\text{SFR}^{(\text{All stars})}$ , is obtained by the galactic-scale model described in §2.3, and the GC star formation rate,  $\text{SFR}^{(\text{GCs})}$ , is obtained by accounting for the formation rate of all GCs (see §4.1). At  $z \approx 0$ , only dwarf halos with  $M_v \lesssim 10^{10.5}$  can have active GC formation that consists of  $\approx 2\%$  of total SFR, while more massive halos have a smaller fraction ( $\lesssim 0.1\%$ ) of stars formed in GCs due to their enriched ISM with decreased amounts of turbulence. This is consistent with observations that only a small number of YMSCs are found in, e.g. the Milky Way (see e.g. table 4 and figure 9 of Krumholz et al. 2019), and that there seems to be an excess of GCs in (ultra-)diffuse dwarf galaxies (e.g. Forbes et al. 2020; Saifollahi et al. 2022; Jones et al. 2023).

At higher redshift, the fraction of stars formed in GCs can be significant. At  $z \gtrsim 7$ , almost all halos have  $\gtrsim 10\%$  of stars formed in GCs, and the fraction can reach to unity at  $z \gtrsim 10$ . Our model suggests that this enhanced GC fraction at high redshift is due to the high SGC density (§2.2), the strong turbulence that effectively compresses sub-clouds (see §3.1), and the low metallicity environment that prevents sub-clouds from fragmentation before becoming very dense (see §3.2).

In Fig. 19, we show the fraction of in-situ star formation rate contributed by GCs for individual galaxies, to highlight the variation of GC-formation efficiency in different galactic environments. In addition to the dependencies on redshift and stellar mass, star-forming environment, as characterized by specific star formation rate (sSFR, defined as SFR per unit stellar mass), also affects the fraction of stars formed in GCs. At all redshifts and stellar masses, a higher sSFR leads to a higher fraction of stars formed in GCs. This is a direct outcome of our external feedback model in the destruction of sub-clouds (§3.3), where low-mass sub-clouds are preferentially destroyed by the wind feedback and a higher SFR raises the threshold mass for sub-clouds to survive. A similar situation has been found observationally that the formation efficiency of bound star clusters appears to be higher in galaxies with higher SFR surface density, albeit with ongoing debates on the potential effects of, e.g. cluster selection criteria and sample homogeneity (see §7 of Adamo et al. 2020, for a review). Note that we have not defined bound star clusters in our model, but rather adopted a conservative selection for GCs. Meanwhile, we have not included the small-scale interactions among nearby sub-clouds via different types of feedbacks and tidal forces (e.g. Deng et al. 2024). A more complete model thus requires modeling correlations of sub-clouds in position and velocity spaces, which may be achieved by calibrations using zoom-in simulations with sufficient resolution to follow ISM physics.

The large fraction of stars that can form in GCs in a high-redshift galaxy has important implications. Indeed, if an observed high- $z$  galaxy is not properly resolved and its light is dominated by young GCs, the properties of the galaxy may not be interpreted correctly in terms of the picture we have from local galaxies. For example, the Sérsic index, which is traditionally used as a measure of the concentration of light in a galaxy with a smooth profile, does not have a clear meaning for a galaxy made up of a set of star clusters. The dependence of GC formation efficiency on the star-forming environment further complicates the observations, as intense star formation usually produces dusty ISM that can obscure the radiation from young GCs. A basic challenge in future observations of high- $z$  galaxies is, therefore, to resolve galaxies down to the scales of GCs so as to identify star clusters reliably in a given field. To this end, our model, which predicts the stellar mass, star formation rate, and size of individual GCs at different redshifts in different halos, can be used to predict observable quantities to explore in detail the feasibility of observing high- $z$  GCs in current and future observations. We will come back to this in a future paper.

## 5 SUMMARY AND DISCUSSION

In this paper, we have developed a model for the formation of GCs. The model is based on the ‘two-phase’ scenario presented in Paper-I, which predicts that the fast assembly of a halo in its early phase drives the formation of SGC that subsequently fragments into a dynamically hot system of sub-clouds. Here we show that a fraction of these sub-clouds can reach a supernova-free regime via two distinctive channels, and lead to the formation of two distinct populations of GCs. The main findings and conclusions are summarized as follows.

- (i) The average density of an SGC is in general below the typical density of GC formation at  $z \leq 10$  (§2.2). The fragmentation of SGC into sub-clouds (§3.1) and compression of sub-clouds are needed to provide conditions for GC formation.
- (ii) There are two channels to make a sub-cloud sufficiently dense to form a GC. The first is shock compression in a turbulent medium produced by gravity and/or SN feedback. This can deform the log-normal density distribution of sub-clouds, producing a high-density, power-law tail,  $n_{\text{sc}} \gtrsim n_{\text{sgc}} \mathcal{M}^2$ , determined by the Mach number  $\mathcal{M}$  (§3.1). The second channel is through radiative cooling in metal-poor sub-clouds ( $Z \lesssim 0.02 Z_{\odot}$ ), where cloud fragmentation and star formation are prohibited before a sub-cloud reaches a high density  $n_{\text{sf},1}$  (§3.2). Both channels are able to lift the density of a sub-cloud to the SN-free regime,  $n'_{\text{sc}} \gtrsim n_{\text{snf}} \approx 10^{3.5} \text{ cm}^{-3}$ , to avoid disruption by SN feedback before forming a GC.
- (iii) According to the channel in which sub-clouds are compactified, we classify GCs into two populations (§3.5): Pop-I, which forms in metal-rich ( $n_{\text{sf},1} < n_{\text{snf}}$ ) sub-clouds with the post-shock density  $n_{\text{sc}} \gtrsim n_{\text{snf}}$ , and Pop-II, which forms in the metal-poor ( $n_{\text{sf},1} \gtrsim n_{\text{snf}}$ ) sub-clouds with a post-cooling density  $n'_{\text{sc}} > n_{\text{snf}}$ . The halo mass and redshift where each class of GCs can actively form can be summarized in a GC-formation diagram, as shown in Fig. 8. Both channels prefer the formation of GCs at high  $z$ , but diverge at low  $z$  where GC formation is suppressed in halos of different masses.
- (iv) After formation, a GC experiences dynamical evolution driven by its tidal environment, so that it loses mass and may eventually be disrupted. The dynamical disruption timescale depends on the tidal force (and thus redshift) and the mass of the cluster itself (§3.6).

We have implemented the ‘two-phase’ galaxy formation scenario



and the ‘two-channel’ GC formation into halo merger trees produced by a N-body simulation. Our main results are summarized as follows.

- (i) The implementation follows a hierarchical design strategy so that it can be applied within a cosmological context. Structures in the Universe are separated, according to their spatial scales, into four levels: large-scale structure of the Universe, halos, galaxies, and sub-clouds. Structures at a large scale are resolved first, and used as boundary conditions for modeling structures at the next smaller scale. The overall context of the model is depicted in Fig. 1, where relevant structures and processes are shown, in terms of the spatial correlation function of GCs. The detailed steps are listed in §4.1.
- (ii) With calibration by observations, a number of observational results of GCs in the local Universe are reproduced, and more results are predicted and to be tested by future observations. The mass and age distributions of GCs produced by the model cover those observed in MW and M31, but do not reproduce those seen in M51, an interacting galaxy. The size-mass relation of GCs, with its normalization tuned to match observations, can be explained as a result of gravity-feedback balance in the star formation of sub-clouds, provided that subsequent dynamical evolution does not drive GCs off the birth-time relation. The relation between the total mass in GCs ( $M_*^{(\text{GCs})}$ ) and the host halo (galaxy) mass is predicted to be linear (non-linear). The bimodal distribution in GC metallicity is produced naturally by the two-channel formation, and the fraction of Pop-I/II GCs as a function of halo mass reflects the enrichment history of the host galaxy. The predicted spatial profile of GCs within the host galaxy is shaped by both in-situ and ex-situ, and both fast-phase and slow-phase, formation of the host galaxy. The modeled profiles match those of MW and M31, but show discrepancies with those observed for dwarfs and BCGs (§4).
- (iii) The linear relation between  $M_*^{(\text{GCs})}$  and the host halo mass is set by the metal enrichment process, and is preserved by the central limit theorem (§4.4).
- (iv) The drop of the Pop-I (red) GC fraction in halos of high mass is inferred to be produced by pristine cold streams at high redshift (§4.5).
- (v) A number of predictions are made for GCs at high redshift. These include the relations between  $M_*^{(\text{GCs})}$  and the host mass (host halo mass, total stellar mass and bulge mass of the host galaxy), the cosmic formation history of GCs in halos of different final masses, and the variation of the GC formation efficiency with star-forming environment (§4.8).

A powerful aspect of our model is its ability to predict the formation of individual GCs based on their host sub-clouds with sampled properties. This mimics the ‘post-processing’ techniques based on resolved cloud properties in high-resolution hydrodynamical simulations (Grudić et al. 2021, 2023), yet can be applied to a much larger volume so as to reproduce the statistical properties of GC populations on cosmological scales. The keys behind this approach are the use of a hierarchical strategy to reduce the model complexity, the use of analytical approximations to derive recipes relevant to each step of GC formation, and the use of the balanced sampling technique to efficiently sample sub-clouds. The sub-cloud-based modeling features only a small number of free parameters so as to avoid fine-tuning.

A number of assumptions in the model of GC have to be verified or extended by observations and/or hydrodynamical simulations. For example, the independent sampling of sub-cloud density and mass (§3.1) is designed to mimic the mass-independent density of virialized dark matter halos given by the spherical collapse model, while dissipative processes in SGCs may introduce a density-mass corre-

lation. Meanwhile, the sub-cloud mass function can be modified by the processes discussed in §3.1, and may thus depend on the environment. These can be explored by hydrodynamical simulation with a resolution that is sufficient for resolving the formation of sub-clouds. Another example is the role of radiative and wind feedback from the internal star formation of a sub-cloud. We argued that such feedback produces the flat size-mass relation of GCs (§3.4). These feedback channels have been simulated in hydrodynamic simulations (e.g. Hopkins et al. 2020; Li et al. 2020), and can be tested by measuring the correlation of gas clouds and young star clusters in observations. The final example is the spatial distribution of GCs within their host galaxies, which is modeled semi-empirically with three-components described in §4.6 and should be improved by directly tracing individual GCs within realistic gravitational potential. The comparison of the spatial distribution with observations can be made by forward modeling that mimics the selection and projection in observations.

The treatment of the dynamical evolution of GCs in this paper is clearly simplified (§3.6). One way to make improvements is to trace the environment of GCs by assigning them to particles in hydrodynamic simulations (e.g. Pfeffer et al. 2018; Chen & Gnedin 2022; Rodriguez et al. 2023). Another way is to calibrate a more realistic model using finer N-body simulations (e.g. Gieles et al. 2011; Prieto & Gnedin 2008; Gieles & Gnedin 2023), or to run cluster simulations directly for a sample of GCs (Rodriguez et al. 2023). All these improvements and numerical techniques should be explored in the future. The information obtained from our modeling can be used to motivate and guide such explorations.

## ACKNOWLEDGEMENTS

We thank the anonymous referees for the useful reports that significantly improve this paper. YC is funded by the China Postdoctoral Science Foundation (grant No. 2022TQ0329). This work is also supported by the National Natural Science Foundation of China (NSFC, Nos. 12192224, 11733004 and 11890693) and CAS Project for Young Scientists in Basic Research (grant No. YSBR-062). YC thanks Kai Wang, Fangzhou Jiang, Tao Wang, Yu Rong, Enci Wang and Baitian Tang for their valuable insights and discussions, and thanks Yi Mao and Chen Chen for their technical support. The authors would like to express their gratitude to the Tsinghua Astrophysics High-Performance Computing platform at Tsinghua University and the Supercomputer Center of the University of Science and Technology of China for providing the necessary computational and data storage resources that have significantly contributed to the research results presented in this paper.

The computations and presentations in this paper are supported by various software tools, including the HPC toolkits HIPP (Chen & Wang 2023)<sup>1</sup> and PyHIPP<sup>2</sup>, interactive computation environment IPYTHON (Perez & Granger 2007), numerical libraries NUMPY (Harris et al. 2020), ASTROPY (Robitaille et al. 2013; Astropy Collaboration et al. 2018, 2022) and SCIPY (Virtanen et al. 2020), the graphical library MATPLOTLIB (Hunter 2007), the halo mass assembly history calculator DIFFMAH (Hearin et al. 2021)<sup>3</sup>, and the two-point correlation function calculator (Sinha & Garrison 2019, 2020)<sup>4</sup>. This research has made extensive use of the arXiv and NASA’s Astrophysics Data System. Data compilations used in this paper have been

<sup>1</sup> <https://github.com/ChenYangyao/hipp>

<sup>2</sup> <https://github.com/ChenYangyao/pyhipp>

<sup>3</sup> <https://github.com/ArgonneCPAC/diffmah>

<sup>4</sup> <https://github.com/manodeep/Corrfunc>



made much more accurate and efficient by the software WEBPLOT-DIGITIZER.

Credit for the images of the structures at the top of Fig. 1: Herschel image of gas sub-clouds around young stars by ESA, NASA, JPL-Caltech, AURA, NSF, STScI and Univ. of Toledo; HST and JWST images of the NGC 628 galaxy by NASA, ESA, CSA, STScI, Janice Lee (STScI) and Thomas Williams (Oxford); Simulated image of halos and cosmic large-scale structures by Li et al. (2022).

## DATA AVAILABILITY

The code repository TwoPhaseGalaxyModel<sup>5</sup> implements the model described in this series of papers. All data used in this paper, including data points displayed in figures and observational results used for calibration and comparison, will be distributed along with the repository. The GC catalog of MW and M31 produced by the empirical model of Chen & Gnedin (2024) is available online<sup>6</sup>. The star cluster catalogs of LEGUS survey are available online<sup>7</sup>. The data of the IllustrisTNG project can be found at their website<sup>8</sup>.

## REFERENCES

- Adamo A., et al., 2020, *Space Sci. Rev.*, 216, 69
- Adamo A., et al., 2024, *Nature*, 632, 513
- Alabi A. B., et al., 2016, *MNRAS*, 460, 3838
- Appel S. M., Burkhard B., Semenov V. A., Federrath C., Rosen A. L., 2022, *ApJ*, 927, 75
- Arca Sedda M., et al., 2024, *MNRAS*, 528, 5119
- Astropy Collaboration et al., 2018, *AJ*, 156, 123
- Astropy Collaboration et al., 2022, *ApJ*, 935, 167
- Bastian N., Emsellem E., Kissler-Patig M., Maraston C., 2006, *A&A*, 445, 471
- Bastian N., Pfeffer J., Kruijssen J. M. D., Crain R. A., Trujillo-Gomez S., Reina-Campos M., 2020, *MNRAS*, 498, 1050
- Baumgardt H., Hilker M., 2018, *MNRAS*, 478, 1520
- Behroozi P. S., Wechsler R. H., Conroy C., 2013, *ApJ*, 770, 57
- Berlind A. A., Weinberg D. H., 2002, *ApJ*, 575, 587
- Bílek M., Samurović S., Renaud F., 2019, *A&A*, 625, A32
- Bílek M., Hilker M., Renaud F., Richtler T., Chaturvedi A., Samurović S., 2024, *A&A*, 682, A111
- Bishop C. M., 2006, *Pattern Recognition and Machine Learning*. Springer
- Blakeslee J. P., 1997, *ApJ*, 481, L59
- Blakeslee J. P., 1999, *AJ*, 118, 1506
- Bouwens R. J., et al., 2023, *MNRAS*, 523, 1036
- Boylan-Kolchin M., 2017, *MNRAS*, 472, 3120
- Boylan-Kolchin M., Springel V., White S. D. M., Jenkins A., Lemson G., 2009, *MNRAS*, 398, 1150
- Brown G., Gnedin O. Y., 2021, *MNRAS*, 508, 5935
- Bruzual G., Charlot S., 2003, *MNRAS*, 344, 1000
- Buck T., Pfrommer C., Girichidis P., Corobean B., 2022, *MNRAS*, 513, 1414
- Burkert A., Forbes D. A., 2020, *AJ*, 159, 56
- Burkert B., Falceta-Gonçalves D., Kowal G., Lazarian A., 2009, *ApJ*, 693, 250
- Burkhart B., Stalpes K., Collins D. C., 2017, *ApJ*, 834, L1
- Caldwell N., Schiavon R., Morrison H., Rose J. A., Harding P., 2011, *AJ*, 141, 61
- Camargo D., Minniti D., 2019, *MNRAS*, 484, L90
- Caso J. P., De Bórtoli B. J., Ennis A. I., Bassino L. P., 2019, *MNRAS*, 488, 4504
- Caso J. P., Ennis A. I., De Bórtoli B. J., 2024, *MNRAS*, 527, 6993
- Ceverino D., Dekel A., Bournaud F., 2010, *MNRAS*, 404, 2151
- Chen Y., Gnedin O. Y., 2022, *MNRAS*, 514, 4736
- Chen Y., Gnedin O. Y., 2023, *MNRAS*, 522, 5638
- Chen Y., Gnedin O. Y., 2024, *MNRAS*, 527, 3692
- Chen Y., Wang K., 2023, *Astrophysics Source Code Library*, p. ascl:2301.030
- Chen Y., Mo H. J., Li C., Wang K., Wang H., Yang X., 2023, *MNRAS*, 525, 1254
- Chen Y., Mo H., Wang H., 2024, *MNRAS*, 532, 4340
- Choksi N., Gnedin O. Y., 2019, *MNRAS*, 488, 5409
- Choksi N., Gnedin O. Y., Li H., 2018, *MNRAS*, 480, 2343
- Chon S., Omukai K., Schneider R., 2021, *MNRAS*, 508, 4175
- Claeyssens A., Adamo A., Richard J., Mahler G., Messa M., Dessauges-Zavadsky M., 2023, *MNRAS*, 520, 2180
- Collins D. C., Padoan P., Norman M. L., Xu H., 2011, *ApJ*, 731, 59
- Curti M., Mannucci F., Cresci G., Maiolino R., 2020, *MNRAS*, 491, 944
- Curti M., et al., 2024, *A&A*, 684, A75
- Danovich M., Dekel A., Hahn O., Ceverino D., Primack J., 2015, *MNRAS*, 449, 2087
- Davis M., Efstathiou G., Frenk C. S., White S. D. M., 1985, *ApJ*, 292, 371
- De Bórtoli B. J., Caso J. P., Ennis A. I., Bassino L. P., 2022, *MNRAS*, 510, 5725
- De Lucia G., Blaizot J., 2007, *MNRAS*, 375, 2
- De Lucia G., Kruijssen J. M. D., Trujillo-Gomez S., Hirschmann M., Xie L., 2024, *MNRAS*, 530, 2760
- Dekel A., Burkert A., 2014, *MNRAS*, 438, 1870
- Dekel A., Sari R., Ceverino D., 2009, *ApJ*, 703, 785
- Dekel A., Zolotov A., Tweed D., Cacciato M., Ceverino D., Primack J. R., 2013, *MNRAS*, 435, 999
- Dekel A., Sarkar K. C., Birnboim Y., Mandelker N., Li Z., 2023, *MNRAS*, 523, 3201
- Deng Y., Li H., Liu B., Kannan R., Smith A., Bryan G. L., 2024, *A&A*, 691, A231
- Dessauges-Zavadsky M., Adamo A., 2018, *MNRAS*, 479, L118
- Dib S., Kravtsov V. V., Haghi H., Zonoozi A. H., Belinchón J. A., 2022, *A&A*, 664, A145
- Dolag K., Borgani S., Murante G., Springel V., 2009, *MNRAS*, 399, 497
- Dornan V., Harris W. E., 2023, *ApJ*, 950, 179
- El-Badry K., Wetzel A., Geha M., Hopkins P. F., Kereš D., Chan T. K., Faucher-Giguère C.-A., 2016, *ApJ*, 820, 131
- El-Badry K., Quataert E., Weisz D. R., Choksi N., Boylan-Kolchin M., 2019, *MNRAS*, 482, 4528
- Fahrion K., et al., 2020a, *A&A*, 637, A26
- Fahrion K., et al., 2020b, *A&A*, 637, A27
- Fall S. M., 1983, in Athanassoula E., ed., *IAU Symposium Vol. 100, Internal Kinematics and Dynamics of Galaxies*. pp 391–398
- Fall S. M., Chandar R., 2012, *ApJ*, 752, 96
- Fall S. M., Efstathiou G., 1980, *MNRAS*, 193, 189
- Fall S. M., Rees M. J., 1985, *ApJ*, 298, 18
- Fall S. M., Zhang Q., 2001, *ApJ*, 561, 751
- Fall S. M., Krumholz M. R., Matzner C. D., 2010, *ApJ*, 710, L142
- Fernandez R., Bryan G. L., 2018, *MNRAS*, 479, 200
- Ferrone S., Di Matteo P., Mastrobuono-Battisti A., Haywood M., Snaith O. N., Montuori M., Khoperskov S., Valls-Gabaud D., 2023, *A&A*, 673, A44
- Figer D. F., 2004, in Lamers H. J. G. L. M., Smith L. J., Nota A., eds, *Astronomical Society of the Pacific Conference Series Vol. 322, The Formation and Evolution of Massive Young Star Clusters*. p. 49 ([arXiv:astro-ph/0403088](https://arxiv.org/abs/astro-ph/0403088), doi:10.48550/arXiv.astro-ph/0403088)
- Figer D. F., McLean I. S., Morris M., 1999, *ApJ*, 514, 202
- Finkelstein S. L., et al., 2023, *ApJ*, 946, L13
- Forbes D. A., Gannon J., 2024, *MNRAS*, 528, 608
- Forbes D. A., Remus R.-S., 2018, *MNRAS*, 479, 4760
- Forbes D. A., Alabi A., Romanowsky A. J., Brodie J. P., Arimoto N., 2020, *MNRAS*, 492, 4874
- Fujimoto S., et al., 2024, *Primordial Rotating Disk Composed*

- of  $\geq 15$  Dense Star-Forming Clumps at Cosmic Dawn, [doi:10.48550/arXiv.2402.18543](https://doi.org/10.48550/arXiv.2402.18543)
- Gieles M., Gnedin O. Y., 2023, *MNRAS*, 522, 5340
- Gieles M., Portegies Zwart S. F., 2011, *MNRAS*, 410, L6
- Gieles M., Heggie D. C., Zhao H., 2011, *MNRAS*, 413, 2509
- Girichidis P., Konstantin L., Whitworth A. P., Klessen R. S., 2014, *ApJ*, 781, 91
- Graham A. W., Sahu N., 2023, *MNRAS*, 518, 2177
- Grudić M. Y., Hopkins P. F., Faucher-Giguère C.-A., Quataert E., Murray N., Kereš D., 2018, *MNRAS*, 475, 3511
- Grudić M. Y., Kruijssen J. M. D., Faucher-Giguère C.-A., Hopkins P. F., Ma X., Quataert E., Boylan-Kolchin M., 2021, *MNRAS*, 506, 3239
- Grudić M. Y., Hafen Z., Rodriguez C. L., Guszejnov D., Lamberts A., Wetzel A., Boylan-Kolchin M., Faucher-Giguère C.-A., 2023, *MNRAS*, 519, 1366
- Guo H., et al., 2015, *MNRAS*, 453, 4368
- Guo H., et al., 2016, *MNRAS*, 459, 3040
- Gupta S., Nath B. B., Sharma P., Shchekinov Y., 2016, *MNRAS*, 462, 4532
- Haghi H., Safaei G., Zonoozi A. H., Kroupa P., 2020, *ApJ*, 904, 43
- Harikane Y., et al., 2023, *ApJS*, 265, 5
- Harris W. E., 1996, *AJ*, 112, 1487
- Harris W. E., 2010, *Philosophical Transactions of the Royal Society of London Series A*, 368, 889
- Harris W. E., 2023, *ApJS*, 265, 9
- Harris W. E., Racine R., 1979, *ARA&A*, 17, 241
- Harris W. E., Reina-Campos M., 2024, *ApJ*, 971, 155
- Harris W. E., Harris G. L. H., Alessi M., 2013, *ApJ*, 772, 82
- Harris W. E., Harris G. L., Hudson M. J., 2015, *ApJ*, 806, 36
- Harris W. E., Blakeslee J. P., Harris G. L. H., 2017, *ApJ*, 836, 67
- Harris C. R., et al., 2020, *Nature*, 585, 357
- Hartman K., Harris W. E., 2024, *AJ*, 168, 75
- Hartman K., Harris W. E., Blakeslee J. P., Ma C.-P., Greene J. E., 2023, *ApJ*, 953, 154
- Hearin A. P., Chaves-Montero J., Becker M. R., Alarcon A., 2021, *The Open Journal of Astrophysics*, 4, 7
- Henry R. B. C., Edmunds M. G., Köppen J., 2000, *ApJ*, 541, 660
- Hirschi R., 2007, *A&A*, 461, 571
- Hopkins P. F., Quataert E., Murray N., 2012, *MNRAS*, 421, 3522
- Hopkins P. F., Grudić M. Y., Wetzel A., Kereš D., Faucher-Giguère C.-A., Ma X., Murray N., Butcher N., 2020, *MNRAS*, 491, 3702
- Hopkins P. F., et al., 2023, *MNRAS*, 525, 2241
- Huang K.-H., et al., 2017, *ApJ*, 838, 6
- Hudson M. J., Robison B., 2018, *MNRAS*, 477, 3869
- Hudson M. J., Harris G. L., Harris W. E., 2014, *ApJ*, 787, L5
- Hunter J. D., 2007, *Computing in Science & Engineering*, 9, 90
- Janka H.-T., 2012, *Annual Review of Nuclear and Particle Science*, 62, 407
- Janssens S. R., et al., 2022, *MNRAS*, 517, 858
- Ji Z., Giallisco M., 2023, *ApJ*, 943, 54
- Jiang F., et al., 2019, *MNRAS*, 488, 4801
- Jing Y. P., Mo H. J., Börner G., 1998, *ApJ*, 494, 1
- Jones M. G., et al., 2023, *ApJ*, 942, L5
- Kartha S. S., Forbes D. A., Spitler L. R., Romanowsky A. J., Arnold J. A., Brodie J. P., 2014, *MNRAS*, 437, 273
- Keres D., Katz N., Weinberg D. H., Dave R., 2005, *MNRAS*, 363, 2
- Khullar S., Federrath C., Krumholz M. R., Matzner C. D., 2021, *MNRAS*, 507, 4335
- Kiihne A., Appel S. M., Burkhardt B., Semenov V. A., Federrath C., 2025, *ApJ*, 979, 89
- Klein R. I., McKee C. F., Colella P., 1994, *ApJ*, 420, 213
- Klessen R. S., Glover S. C. O., 2023, *ARA&A*, 61, 65
- Kobayashi C., Umeda H., Nomoto K., Tominaga N., Ohkubo T., 2006, *ApJ*, 653, 1145
- Kravtsov A. V., 2013, *ApJ*, 764, L31
- Kruijssen J. M. D., 2012, *MNRAS*, 426, 3008
- Kruijssen J. M. D., 2014, *Classical and Quantum Gravity*, 31, 244006
- Kruijssen J. M. D., Pelupessy F. I., Lamers H. J. G. L. M., Portegies Zwart S. F., Icke V., 2011, *MNRAS*, 414, 1339
- Kruijssen J. M. D., Pfeffer J. L., Crain R. A., Bastian N., 2019a, *MNRAS*, 486, 3134
- Kruijssen J. M. D., Pfeffer J. L., Reina-Campos M., Crain R. A., Bastian N., 2019b, *MNRAS*, 486, 3180
- Krumholz M. R., 2012, *ApJ*, 759, 9
- Krumholz M. R., McKee C. F., Bland-Hawthorn J., 2019, *ARA&A*, 57, 227
- Lada C. J., Dame T. M., 2020, *ApJ*, 898, 3
- Lamers H. J. G. L. M., Gieles M., Portegies Zwart S. F., 2005, *A&A*, 429, 173
- Lapiner S., et al., 2023, *MNRAS*, 522, 4515
- Larson R. B., 1981, *MNRAS*, 194, 809
- Larson R. B., 1998, *MNRAS*, 301, 569
- Latif M. A., Whalen D. J., Khochfar S., Herrington N. P., Woods T. E., 2022a, *Nature*, 607, 48
- Latif M. A., Whalen D., Khochfar S., 2022b, *ApJ*, 925, 28
- Leitherer C., et al., 1999, *ApJS*, 123, 3
- Leroy A. K., Walter F., Brinks E., Bigiel F., de Blok W. J. G., Madore B., Thornley M. D., 2008, *AJ*, 136, 2782
- Li H., Gnedin O. Y., 2014, *ApJ*, 796, 10
- Li H., Vogelsberger M., Marinacci F., Sales L. V., Torrey P., 2020, *MNRAS*, 499, 5862
- Li R., et al., 2022, *ApJ*, 936, 11
- Li Z., Dekel A., Sarkar K. C., Aung H., Giallisco M., Mandelker N., Tacchella S., 2024, *A&A*, 690, A108
- Lian J., et al., 2020, *MNRAS*, 497, 2371
- Liang J., Jiang F., Mo H., Benson A., Dekel A., Tavron N., Hopkins P. F., Ho L. C., 2024a, Connection between Galaxy Morphology and Dark-Matter Halo Structure I: A Running Threshold for Thin Discs and Size Predictors from the Dark Sector, [doi:10.48550/arXiv.2403.14749](https://doi.org/10.48550/arXiv.2403.14749)
- Liang J., Jiang F., Danieli S., Benson A., Hopkins P., 2024b, *ApJ*, 964, 53
- Lilly S. J., Carollo C. M., Pipino A., Renzini A., Peng Y., 2013, *ApJ*, 772, 119
- Lin X., et al., 2023, *ApJ*, 944, L59
- Lu Z., Mo H. J., Lu Y., Katz N., Weinberg M. D., van den Bosch F. C., Yang X., 2014, *MNRAS*, 439, 1294
- Lu Z., Mo H. J., Lu Y., 2015, *MNRAS*, 450, 606
- Luo X., et al., 2024, *ApJ*, 966, 236
- Ma X., et al., 2020, *MNRAS*, 493, 4315
- Madau P., Dickinson M., 2014, *ARA&A*, 52, 415
- Maiolino R., Mannucci F., 2019, *A&ARv*, 27, 3
- Maiolino R., et al., 2024, *A&A*, 691, A145
- Mandelker N., van Dokkum P. G., Brodie J. P., van den Bosch F. C., Ceverino D., 2018, *ApJ*, 861, 148
- Mannucci F., Cresci G., Maiolino R., Marconi A., Gnerucci A., 2010, *MNRAS*, 408, 2115
- Marinacci F., Sales L. V., Vogelsberger M., Torrey P., Springel V., 2019, *MNRAS*, 489, 4233
- Marks M., Kroupa P., Dabringhausen J., Pawlowski M. S., 2012, *MNRAS*, 422, 2246
- Marszewski A., Sun G., Faucher-Giguère C.-A., Hayward C. C., Feldmann R., 2024, *ApJ*, 967, L41
- Matthee J., et al., 2024, *ApJ*, 963, 129
- McLaughlin D. E., 1999, *AJ*, 117, 2398
- McLaughlin D. E., Fall S. M., 2008, *ApJ*, 679, 1272
- Mercedes-Feliz J., et al., 2024, *MNRAS*, 530, 2795
- Messa M., et al., 2018, *MNRAS*, 473, 996
- Messa M., Dessauges-Zavadsky M., Adamo A., Richard J., Claeysens A., 2024, *MNRAS*, 529, 2162
- Metzger B. D., 2017, *Living Reviews in Relativity*, 20, 3
- Milone A. P., Marino A. F., 2022, *Universe*, 8, 359
- Milone A. P., et al., 2017, *MNRAS*, 464, 3636
- Minniti D., et al., 2021, *A&A*, 652, A129
- Mo H. J., Mao S., White S. D. M., 1998, *MNRAS*, 295, 319
- Mo H., van den Bosch F., White S., 2010, *Galaxy Formation and Evolution*. Cambridge University Press
- Mo H., Chen Y., Wang H., 2024, *MNRAS*, 532, 3808
- Mok A., Chandar R., Fall S. M., 2019, *ApJ*, 872, 93
- Mok A., Chandar R., Fall S. M., 2021, *ApJ*, 911, 8

- Mowla L., van der Wel A., van Dokkum P., Miller T. B., 2019, *ApJ*, 872, L13
- Mowla L., et al., 2024, The Firefly Sparkle: The Earliest Stages of the Assembly of A Milky Way-type Galaxy in a 600 Myr Old Universe, [doi:10.48550/arXiv.2402.08696](https://doi.org/10.48550/arXiv.2402.08696)
- Myers P. C., 2015, *ApJ*, 806, 226
- Nakajima K., Ouchi M., Isobe Y., Harikane Y., Zhang Y., Ono Y., Umeda H., Oguri M., 2023, *ApJS*, 269, 33
- Nelson D., et al., 2019, *Computational Astrophysics and Cosmology*, 6, 2
- Pacucci F., Loeb A., 2024, *ApJ*, 964, 154
- Pacucci F., Nguyen B., Carniani S., Maiolino R., Fan X., 2023, *ApJ*, 957, L3
- Palma T., et al., 2019, *MNRAS*, 487, 3140
- Peebles P. J. E., Dicke R. H., 1968, *ApJ*, 154, 891
- Peng E. W., et al., 2008, *ApJ*, 681, 197
- Peng Y., Maiolino R., Cochrane R., 2015, *Nature*, 521, 192
- Pereira-Santaella M., et al., 2024, *A&A*, 685, L13
- Perez F., Granger B. E., 2007, *Computing in Science and Engineering*, 9, 21
- Pfeffer J., Kruijssen J. M. D., Crain R. A., Bastian N., 2018, *MNRAS*, 475, 4309
- Pillepich A., et al., 2018, *MNRAS*, 475, 648
- Planck Collaboration et al., 2016, *A&A*, 594, A13
- Portegies Zwart S. F., McMillan S. L. W., Gieles M., 2010, *ARA&A*, 48, 431
- Portinari L., Chiosi C., Bressan A., 1998, *A&A*, 334, 505
- Prieto J. L., Gnedin O. Y., 2008, *ApJ*, 689, 919
- Qin F., Howlett C., Stevens A. R. H., Parkinson D., 2022, *ApJ*, 937, 113
- Raiter A., Schaerer D., Fosbury R. A. E., 2010, *A&A*, 523, A64
- Robitaille T. P., et al., 2013, *A&A*, 558, A33
- Rodriguez-Gomez V., et al., 2015, *MNRAS*, 449, 49
- Rodriguez C. L., Hafen Z., Grudić M. Y., Lamberts A., Sharma K., Faucher-Giguère C.-A., Wetzel A., 2023, *MNRAS*, 521, 124
- Rojas-Arriagada A., Zoccali M., Schultheis M., Recio-Blanco A., Zasowski G., Minniti D., Jönsson H., Cohen R. E., 2019, *A&A*, 626, A16
- Roman-Oliveira F., Rizzo F., Fraternali F., 2024, *A&A*, 687, A35
- Rosen A. L., 2022, *ApJ*, 941, 202
- Rosswog S., Piran T., Nakar E., 2013, *MNRAS*, 430, 2585
- Saifollahi T., Zaritsky D., Trujillo L., Peletier R. F., Knapen J. H., Amorisco N., Beasley M. A., Donnerstein R., 2022, *MNRAS*, 511, 4633
- Sanders R. L., et al., 2021, *ApJ*, 914, 19
- Schweizer F., 1999, in Hubeny I., Heap S., Cornett R., eds, *Astronomical Society of the Pacific Conference Series Vol. 192, Spectrophotometric Dating of Stars and Galaxies*. p. 135 ([arXiv:astro-ph/9906488](https://arxiv.org/abs/astro-ph/9906488)), [doi:10.48550/arXiv.astro-ph/9906488](https://doi.org/10.48550/arXiv.astro-ph/9906488)
- Sharda P., Krumholz M. R., 2022, *MNRAS*, 509, 1959
- Shi F., et al., 2016, *ApJ*, 833, 241
- Simioni M., Aparicio A., Piotto G., 2020, *MNRAS*, 495, 3981
- Sinha M., Garrison L. H., 2019, in *Software Challenges to Exascale Computing*. Second Workshop. Delhi, India, pp 3–20 ([arXiv:1911.08275](https://arxiv.org/abs/1911.08275)), [doi:10.1007/978-981-13-7729-7\\_1](https://doi.org/10.1007/978-981-13-7729-7_1)
- Sinha M., Garrison L. H., 2020, *MNRAS*, 491, 3022
- Slyz A. D., Devriendt J. E. G., Bryan G., Silk J., 2005, *MNRAS*, 356, 737
- Smith B., Sigurdsson S., Abel T., 2008, *MNRAS*, 385, 1443
- Somerville R. S., et al., 2018, *MNRAS*, 473, 2714
- Spitler L. R., Forbes D. A., 2009, *MNRAS*, 392, L1
- Springel V., 2005, *MNRAS*, 364, 1105
- Springel V., White S. D. M., Tormen G., Kauffmann G., 2001, *MNRAS*, 328, 726
- Stacy A., Bromm V., Lee A. T., 2016, *MNRAS*, 462, 1307
- Tacchella S., Dekel A., Carollo C. M., Ceverino D., DeGraf C., Lapiner S., Mandelker N., Primack Joel R., 2016, *MNRAS*, 457, 2790
- Tang B., et al., 2021, *ApJ*, 908, 220
- Tremonti C. A., et al., 2004, *ApJ*, 613, 898
- Upadhyaya A., Marques-Chaves R., Schaerer D., Martins F., Pérez-Fournon I., Palacios A., Stanway E. R., 2024, *A&A*, 686, A185
- Usher C., Forbes D. A., Spitler L. R., Brodie J. P., Romanowsky A. J., Strader J., Woodley K. A., 2013, *MNRAS*, 436, 1172
- Valenzuela L. M., Moster B. P., Remus R.-S., O’Leary J. A., Burkert A., 2021, *MNRAS*, 505, 5815
- Valenzuela L. M., Remus R.-S., McKenzie M., Forbes D. A., 2024, *A&A*, 687, A104
- Vanzella E., et al., 2022, *ApJ*, 940, L53
- Vanzella E., et al., 2023, *ApJ*, 945, 53
- Venturi G., et al., 2024, *A&A*, 691, A19
- Virtanen P., et al., 2020, *Nature Methods*, 17, 261
- Vital E., Boldrini P., 2022, *A&A*, 667, A112
- Wallerstein G., 1962, *ApJS*, 6, 407
- Wang E., Lilly S. J., 2021, *ApJ*, 910, 137
- Wang X., et al., 2019, *ApJ*, 882, 94
- Wang X., et al., 2022, *ApJ*, 938, L16
- Wang K., et al., 2023, *Nature*, 623, 296
- Wang T., et al., 2024, *MASSive Galaxies aCross cOSmic Time Revealed by JWST/MIRI (MACROSS): The True Number Density of Massive Galaxies in the Early Universe*, [doi:10.48550/arXiv.2403.02399](https://doi.org/10.48550/arXiv.2403.02399)
- Wei P., Zou H., Lin L., Zhou X., Liu X., Kong X., Ma L., Ma S.-G., 2021, *Research in Astronomy and Astrophysics*, 21, 006
- Weibel A., et al., 2024, *MNRAS*, 533, 1808
- Weinberg D. H., et al., 2019, *ApJ*, 874, 102
- Welch B., et al., 2023, *ApJ*, 943, 2
- Whitaker K. E., et al., 2025, *Discovery of Ancient Globular Cluster Candidates in The Relic, a Quiescent Galaxy at Z=2.5* ([arXiv:2501.07627](https://arxiv.org/abs/2501.07627)), [doi:10.48550/arXiv.2501.07627](https://doi.org/10.48550/arXiv.2501.07627)
- Whitmore B. C., Zhang Q., Leitherer C., Fall S. M., Schweizer F., Miller B. W., 1999, *AJ*, 118, 1551
- Wiersma R. P. C., Schaye J., Smith B. D., 2009, *MNRAS*, 393, 99
- Woosley S. E., Heger A., Weaver T. A., 2002, *Reviews of Modern Physics*, 74, 1015
- Xiao M., et al., 2024, *Nature*, 635, 311
- Yang X., Mo H. J., van den Bosch F. C., Zhang Y., Han J., 2012a, *ApJ*, 752, 41
- Yang X., Mo H. J., van den Bosch F. C., Zhang Y., Han J., 2012b, *ApJ*, 752, 41
- Yuan S., Garrison L. H., Hadzhiyska B., Bose S., Eisenstein D. J., 2022, *MNRAS*, 510, 3301
- Zaritsky D., Colucci J. E., Pessev P. M., Bernstein R. A., Chandar R., 2014, *ApJ*, 796, 71
- Zhang Q., Fall S. M., 1999, *ApJ*, 527, L81
- Zhang Z.-Y., Romano D., Ivison R. J., Papadopoulos P. P., Matteucci F., 2018, *Nature*, 558, 260
- Zhang S., et al., 2023, *Science*, 380, 494
- Zhao D. H., Mo H. J., Jing Y. P., Börner G., 2003, *MNRAS*, 339, 12
- Zolotov A., et al., 2015, *MNRAS*, 450, 2327

## APPENDIX A: BALANCED SAMPLING

As mentioned in §4.1, a complete sampling of sub-clouds on the cosmological scale is expensive in terms of computation and storage. To reduce the cost while maintaining the statistical robustness, here we introduce the balanced sampling (BSAMPLING) technique. For more details of the random sampling theory and its general application, refer to, e.g. Bishop (2006).

First, we note that most of the statistical tasks for sub-clouds/GCs in this paper can be abstracted as an integration, which can be estimated by the standard, unweighted Monte Carlo method as

$$\mathbb{E}(f) = \int f(\mathbf{x})p(\mathbf{x})d\mathbf{x} \approx \frac{1}{N'_{\text{sc}}} \sum_{i=1}^{N'_{\text{sc}}} f(\mathbf{x}_i). \quad (\text{A1})$$

Here,  $\mathbf{x} \sim p(\mathbf{x})$  is a set of sub-cloud/GC properties following the target probability density function of  $p(\mathbf{x})$ ,  $f(\mathbf{x})$  is the target function in interest,  $\mathbb{E}(f)$  is the expectation value of  $f$ ,  $\{\mathbf{x}_i\}_{i=1}^{N'_{\text{sc}}}$  is a random set of  $N'_{\text{sc}}$  sub-clouds sampled from  $p(\mathbf{x})$ . It can be proved that this estimator of  $\mathbb{E}(f)$  has an asymptotic variance of  $\sim N'^{-1}_{\text{sc}}$ , independent of the dimension of  $\mathbf{x}$ , and is thus, in principle, an accurate and convenient way of solving many statistical problems. The actual speed of convergence of this estimator, however, depends on the

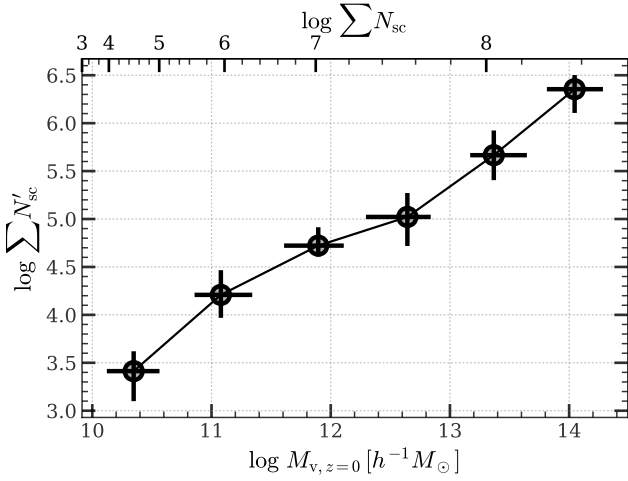


**Figure A1.** The total number of sub-clouds as a function of host halo mass at  $z = 0$ . Here,  $\sum N'_{sc}$  is the number of B-sampled sub-clouds obtained for each central galaxy at  $z = 0$  by summing the number of subclouds,  $N'_{sc}$ , formed in every progenitor in the main and side branches.  $\sum N_{sc}$  is the real number of sub-clouds. **Markers and error bars** show the median values and the  $1-\sigma$  ranges, respectively, obtained by a number of trial runs for each bin of halo mass. The BSAMPLING technique can significantly reduce the computational costs while maintaining the statistical robustness. See Appendix A for more details.

smoothness of  $f$  and the uniformity of  $p(\mathbf{x})$ , and thus can be slow in practice, especially in our case where the distribution functions of sub-clouds have a large dynamic range. It is also worth noting that the formulation of the problem as  $\mathbb{E}(f)$  covers not only the first-order statistics, but also higher-order ones. For example, taking  $f(\mathbf{x}) = [\mathbf{x} - \mathbb{E}(\mathbf{x})]^2$ , one can estimate the variance of  $\mathbf{x}$ .

To address the large dynamic range of  $p(\mathbf{x})$ , we can propose a more balanced distribution,  $q(\mathbf{x})$ , to replace  $p(\mathbf{x})$ . Since the normalization constants of  $p(\mathbf{x})$  and  $q(\mathbf{x})$  are usually unknown, we express them as  $p(\mathbf{x}) = \tilde{p}(\mathbf{x})/Z_p$  and  $q(\mathbf{x}) = \tilde{q}(\mathbf{x})/Z_q$ , where  $\tilde{p}(\mathbf{x})$  and  $\tilde{q}(\mathbf{x})$  are the unnormalized distribution functions and  $Z_p$  and  $Z_q$  are their normalization constants (also known as partition functions in physics), respectively. With the proposal distribution, we can rewrite the Monte Carlo estimator as

$$\begin{aligned} \mathbb{E}(f) &= \int f(\mathbf{x}) p(\mathbf{x}) d\mathbf{x} = \int f(\mathbf{x}) \frac{\tilde{p}(\mathbf{x})}{\tilde{q}(\mathbf{x})} q(\mathbf{x}) d\mathbf{x} \\ &= \frac{Z_q}{Z_p} \int f(\mathbf{x}) \frac{\tilde{p}(\mathbf{x})}{\tilde{q}(\mathbf{x})} q(\mathbf{x}) d\mathbf{x} \\ &\approx \frac{Z_q}{Z_p} \frac{1}{N'_{sc}} \sum_{i=1}^{N'_{sc}} f(\mathbf{x}_i) \tilde{r}_i, \end{aligned} \quad (\text{A2})$$

where  $\tilde{r}_i \equiv \tilde{p}(\mathbf{x}_i)/\tilde{q}(\mathbf{x}_i)$  is the probability ratio, and  $\mathbf{x}_i$  is now drawn from  $q(\mathbf{x})$ . The factor  $Z_q/Z_p$  can be estimated in the same way using the same sample, because

$$\frac{Z_p}{Z_q} = \frac{1}{Z_q} \int \tilde{p}(\mathbf{x}) d\mathbf{x} = \int \frac{\tilde{p}(\mathbf{x})}{\tilde{q}(\mathbf{x})} q(\mathbf{x}) d\mathbf{x} \approx \frac{1}{N'_{sc}} \sum_{i=1}^{N'_{sc}} \tilde{r}_i. \quad (\text{A3})$$

Substituting this back into Eq. (A2), we have

$$\mathbb{E}(f) \approx \sum_{i=1}^{N'_{sc}} f(\mathbf{x}_i) \tilde{w}_i, \quad (\text{A4})$$

where  $\tilde{w}_i = \tilde{r}_i / \sum_{j=1}^{N'_{sc}} \tilde{r}_j$ . Here we define the weight  $w_i \equiv N_{sc} \tilde{w}_i$ , with

$N_{sc}$  being the real number of sub-clouds formed in a snapshot in the history of a galaxy, as constrained by the total stellar mass,  $\Delta M_*$ , formed in the entire galaxy (see §4.1). Thus,  $w_i$  can be considered as the number of real sub-clouds represented by a B-sampled sub-cloud. Note that using  $q(\mathbf{x})$  as a replacement can not only improve the speed of convergence, but also allow us to avoid drawing samples directly from  $p(\mathbf{x})$ , in cases where  $p(\mathbf{x})$  is an over-complicated distribution.

The proper choice of  $q(\mathbf{x})$  turns out to be crucial to the sampling efficiency. Two requirements for  $q(\mathbf{x})$  are that it should be nearly uniform in regions of interest, and that it should be easy to draw. Thus, we factorize the distribution of  $\mathbf{x}$  into a product of the marginal distributions:

$$p(\mathbf{x}) = \prod_j p^{(j)}(x_i^{(j)}), \quad (\text{A5})$$

where each  $x_i^{(j)}$  is a sub-cloud/GC property. The properties interested in this paper are sub-cloud mass ( $M_{sc}$ ; see §3.1 and Eq. 30), density contrast ( $s$ ; see §3.1 and Eq. 31), star formation threshold ( $n'_{sc}$ ; see §3.2 and Eq. 45) and the metallicity of the stream inflow ( $Z_{sc}$ ; see §4.5 and Eq. 73). We choose a power-law form for each of the proposal distributions,  $q(x_i^{(j)})$ , with the power-law index close to  $-1$ , to ensure the uniformity in the logarithmic space. After a number of trials, we find that

$$q(M_{sc}) \propto M_{sc}^{-0.75}; \quad (\text{A6})$$

$$q(n'_{sc}) \propto n'_{sc}^{-0.75}; \quad (\text{A7})$$

$$q(Z_{sc}) \propto Z_{sc}^{-0.75}; \quad (\text{A8})$$

$$q(s) \propto s^{-1.25} \quad (\text{A9})$$

yields stable results, where the more negative index of  $s$  accounts for its log-normal piece that dominates the sub-cloud populations in most cases. The final probability ratio of each sub-cloud,  $\tilde{r}_i$ , is the product of each factor,  $\tilde{r}_i^{(j)} = \tilde{p}(x_i^{(j)})/\tilde{q}(x_i^{(j)})$ , namely

$$\tilde{r}_i = \tilde{r}_i^{(M_{sc})} \tilde{r}_i^{(n'_{sc})} \tilde{r}_i^{(s)} \quad (\text{A10})$$

for the fiducial model, and

$$\tilde{r}_i = \tilde{r}_i^{(M_{sc})} \tilde{r}_i^{(n'_{sc})} \tilde{r}_i^{(s)} \tilde{r}_i^{(Z_{sc})} \quad (\text{A11})$$

for the variant with cold stream inflow (see §4.5).

With the balanced proposal distributions, the number of Monte Carlo samples,  $N'_{sc}$ , can be reduced much compared to the real number of sub-clouds,  $N_{sc}$ . We thus set

$$N'_{sc} = \max \left\{ \left\lfloor \left( \frac{\Delta M_*}{M_B} \right)^{\beta_B} \right\rfloor, N'_{sc, \min} \right\}. \quad (\text{A12})$$

Here, we adopt the power-index  $\beta_B = 1/2$ , a value less than 1 to ensure  $N'_{sc} < N_{sc}$  asymptotically, and  $\geq 1/2$  to ensure that the Poisson noise is not dominant. The lower bound  $N'_{sc, \min} = 4$  is set to ensure that sub-clouds in low-mass galaxies are well represented. The batch mass  $M_B$  is empirically set to be  $10^3 h^{-1} M_{\odot}$  for halos with  $M_{v, z=0} < 10^{12} h^{-1} M_{\odot}$ , and  $2 \times 10^5 h^{-1} M_{\odot}$  otherwise, which we have verified to be stable. Fig. A1 shows the total number of sub-clouds B-sampled in the history of a galaxy at  $z = 0$  as a function of its host halo mass and the real number of sub-clouds.  $N'_{sc}$  is about two orders of magnitude smaller than  $N_{sc}$  for massive galaxies, and thus significantly reduces the computation and storage requirements.

Other target distributions that do not cause imbalance, such as that of  $u_r$  for the effective orbit of dynamical evolution (see §3.6 and Eq. 67), are sampled by the usual Monte Carlo method. In cases where a real, un-weighted sample of sub-clouds is needed (see e.g.



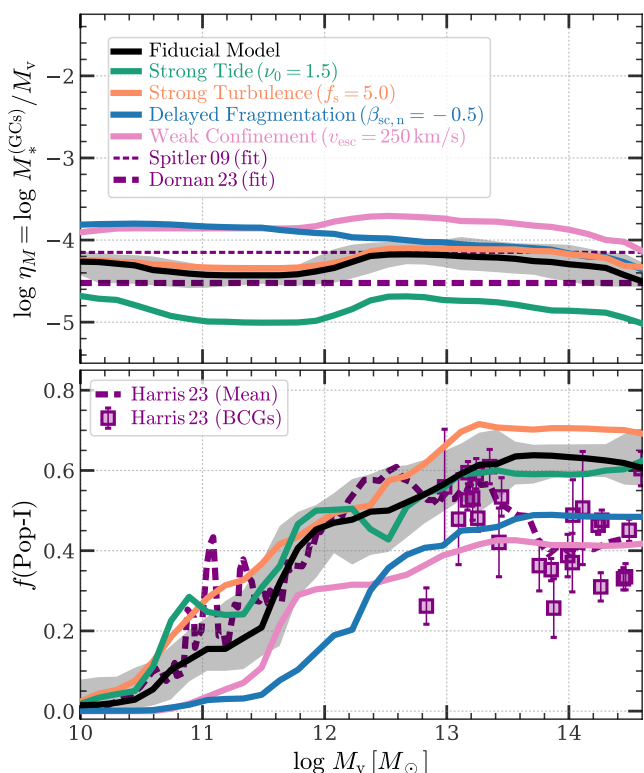


**Figure B1.** Calibration of the model parameters. **Solid curves** show the median relations from different variants of the model. The shaded area of the ‘Fiducial Model’ indicates the  $1\text{-}\sigma$  range. **Purple dashed curves and markers** show the observations, the same as those shown in Fig. 12 and Fig. 14. **Upper panel** shows the mass ratio of the GC system to the host halo, as a function of the host halo mass. **Lower panel** shows the fraction of Pop-I (red) GCs as a function of the host halo mass. All galactic GCs (in-situ and ex-situ) of central galaxies at  $z = 0$  are included in the analysis. For details, see Appendix B.

§4.6 and Fig. 15), a resampling of  $N_{\text{sc}}$  sub-clouds can be made from the  $N'_{\text{sc}}$  B-sampled sub-clouds,  $\{\mathbf{x}_i\}_{i=1}^{N'_{\text{sc}}}$ , using the associated importance weights,  $\{w_i\}_{i=1}^{N'_{\text{sc}}}$ , as discussed in §4.1.

## APPENDIX B: CALIBRATION OF THE MODEL

The model presented in this paper includes several free parameters:  $\beta_{\text{sc},n}$ ,  $\nu_0$ ,  $f_s$ , and those related to metal enrichment (see Table 1 for a complete list). We calibrate these parameters using two observational results: the  $M_*^{(\text{GCs})}$ - $M_V$  relation and the  $f(\text{Pop-I})$ - $M_V$  relation for galactic GC systems at  $z = 0$ .

The parameter  $\beta_{\text{sc},n}$  describes the growth of clumpiness in a single sub-cloud during its cooling and contraction (see §3.2). A smaller value of  $\beta_{\text{sc},n}$  results in a more rapid growth of density perturbation, therefore accelerating the decrease in the cooling timescale  $t_{\text{cool,sc}}$  (see Eq. 42) and leading to earlier fragmentation (see Eq. 44). Conversely, a larger value of  $\beta_{\text{sc},n}$  delays fragmentation. Thus,  $\beta_{\text{sc},n}$  determines the fraction of sub-clouds that can reach the SN-free regime via the Pop-II channel, and consequently, the total mass of GCs that can form in low-mass galaxies. The black curve in the upper panel of Fig. B1 shows the GC-to-halo mass ratio as a function of host halo mass predicted by our fiducial model, with  $\beta_{\text{sc},n} = -2.5$ . For comparison, we define a variant, denoted as ‘Delayed Fragmentation’, with

$\beta_{\text{sc},n} = -0.5$ , shown by the blue curve. The delayed fragmentation results in higher GC mass in galaxies below the Milky Way mass due to enhanced formation of Pop-II GCs. Consequently, the slope of the mass ratio curve changes, becoming inconsistent with the observed  $M_*^{(\text{GCs})}$ - $M_V$  proportionality. Based on this effect of  $\beta_{\text{sc},n}$ , we can determine its optimal value and adopt it as the fiducial one.

The parameter  $\nu_0$  determines the tidal disruption timescale of GCs (see §3.6 and Eq. 69). A larger value of  $\nu_0$  results in a shorter survival time for GCs, leading to fewer observable GCs at any given snapshot. The green curves in Fig. B1 show the results of a model variant, denoted as ‘Strong Tide’, with  $\nu_0 = 1.5$ . The change in the GC-to-halo mass ratio, compared to the fiducial result with  $\nu = 0.6$ , is quite significant, and the fraction of the change is almost independent of the host halo mass. The effect of  $\nu_0$  on the  $f(\text{Pop-I})$ - $M_V$  relation is moderate. The Pop-I fraction in low-mass halos increases because the in-situ Pop-II GCs, which are born earlier (see Fig. 10), are more likely to be disrupted by the strong tidal field. Based on these features of  $\nu_0$ , we can determine its calibrated value mainly using the GC-to-halo mass ratio, with the aid of the Pop-I fraction.

The parameter  $f_s$  describes the strength of supersonic turbulence in the creation of dense sub-clouds, which is the only channel for forming Pop-I GCs. A larger value of  $f_s$  leads to more efficient formation of Pop-I GCs, resulting in a higher fraction of Pop-I GCs. However, the total mass of GCs does not change significantly, as a broader sub-cloud density distribution increases both the probability of a sub-cloud reaching the SN-free threshold,  $n_{\text{snf}}$  (see §3.5), and the production of more sub-clouds that are just below the threshold. Because the total stellar mass has been well constrained by the boundary condition provided by the galactic-scale context (see §2), the total mass of GCs is not sensitive to  $f_s$ . The orange curves in Fig. B1 show the results of a model variant, denoted as ‘Strong Turbulence’, with  $f_s = 5.0$ . Compared to the fiducial model with  $f_s = 1.0$ , the changes in the GC-to-halo mass ratio and Pop-I fraction are as expected. Based on these features of  $f_s$ , we can determine its calibrated value mainly using the Pop-I fraction, with the aid of the GC-to-halo mass ratio.

The most uncertain part of the model is the process of metal enrichment, partly due to the limited constraints from high-redshift observations (e.g. Curti et al. 2020; Sanders et al. 2021; Curti et al. 2024; Venturi et al. 2024), and partly due to the potential systematic differences in metallicity in various regions of the host galaxy (Wang et al. 2019, 2022; Venturi et al. 2024), particularly within the dense sub-clouds. Given the lack of constraints, we propose a heuristic model in §2.4, motivated by the gas-regulator scenario, and adapt it to account for conditions prevalent at high redshifts. The resulting MZR of this model is required to reproduce observed trends, including the slow redshift evolution at  $z \gtrsim 4$  (e.g. Nakajima et al. 2023), the slope of  $\approx 1/3$ – $2/3$  at the low-stellar-mass end (see e.g. figure 3 of Curti et al. 2020), and a bending at the high-stellar-mass end (e.g. Tremonti et al. 2004; Mannucci et al. 2010). All parameters involved in the metal enrichment process affects GC formation via the Pop-II channel (see §3.5), and we adjust them within acceptable ranges that meet the aforementioned requirements to reproduce the GC-to-halo mass ratio and the Pop-I fraction. For example, the pink curves in Fig. B1 show the results of a model variant, denoted as ‘Weak Confinement’, with an escape velocity of  $v_{\text{esc}} = 250 \text{ km s}^{-1}$ , which is larger than the fiducial value of  $75 \text{ km s}^{-1}$ . This variant tends to produce a more metal-poor environment, therefore enhancing the formation of Pop-II GCs. Consequently, the changes in the GC-to-halo mass ratio and Pop-I fraction are both significant, resulting in a clear inconsistency with observations.

An interesting finding by Harris (2023), based on HST data, is

the decline in the Pop-I fraction of BCGs, as indicated by individual markers in the lower panel of Fig. B1. Should this observation be confirmed by future studies with higher resolution and larger sample sizes, it could pose a significant challenge to most of the current models of GC formation. Our analysis suggests that this finding is consistent with a scenario where high-redshift galaxies in massive halos are fed by pristine cold streams, leading to efficient GC formation via the Pop-II channel. Because this scenario provides a promising connection between low-redshift relics and high-redshift gas accretion processes, we have defined an additional suite of variants and discuss their implications in §4.5.

This paper has been typeset from a  $\text{\LaTeX}$  file prepared by the author.